COMPUTATIONALLY EFFICIENT APPROACHES TO INTEGRATED CARDIAC ELECTROPHYSIOLOGY

A THESIS SUBMITTED TO
THE GRADUATE SCHOOL OF NATURAL AND APPLIED SCIENCES
OF
MIDDLE EAST TECHNICAL UNIVERSITY

BY

ÖZGÜR PAŞAOĞLU

IN PARTIAL FULFILLMENT OF THE REQUIREMENTS
FOR
THE DEGREE OF MASTER OF SCIENCE
IN
CIVIL ENGINEERING

AUGUST 2017

Approval of the thesis:

COMPUTATIONALLY EFFICIENT APPROACHES TO INTEGRATED CARDIAC ELECTROPHYSIOLOGY

submitted by **ÖZGÜR PAŞAOĞLU** in partial fulfillment of the requirements for the degree of **Master of Science in Civil Engineering Department, Middle East Technical University** by,

Prof. Dr. Gülbin Dural Ünver _____
Dean, Graduate School of **Natural and Applied Sciences**

Prof. Dr. İsmail Özgür Yaman _____
Head of Department, **Civil Engineering**

Assoc. Prof. Dr. Serdar Göktepe _____
Supervisor, **Civil Engineering Department, METU**

Examining Committee Members:

Prof. Dr. Kağan Tuncay
Civil Engineering Department, METU _____

Assoc. Prof. Dr. Serdar Göktepe
Civil Engineering Department, METU _____

Assoc. Prof. Dr. Ercan Gürses
Aerospace Engineering Department, METU _____

Assist. Prof. Dr. Cüneyt Baykal
Civil Engineering Department, METU _____

Assist. Prof. Dr. Besim Baranoğlu
Manufacturing Engineering Department, Atılım University _____

Date: _____

I hereby declare that all information in this document has been obtained and presented in accordance with academic rules and ethical conduct. I also declare that, as required by these rules and conduct, I have fully cited and referenced all material and results that are not original to this work.

Name, Last Name: ÖZGÜR PAŞAOĞLU

Signature :

ABSTRACT

COMPUTATIONALLY EFFICIENT APPROACHES TO INTEGRATED CARDIAC ELECTROPHYSIOLOGY

Paşaoğlu, Özgür
M.S., Department of Civil Engineering
Supervisor : Assoc. Prof. Dr. Serdar Göktepe

August 2017, 103 pages

This work is concerned with the development of numerically efficient approaches for cardiac electrophysiology within the bidomain setting. In this approach, non-linear cardiac tissue is embedded into a linear conductor, called the torso. While the excitation of cardiac tissue involves two field variables, the transmembrane potential and the extracellular potential, the electrical activity of the torso involve the extracellular potential field only. The electrophysiological behavior of cardiac tissue is governed by a set of two partial differential equations. One of these equations contains a highly non-linear ionic current term that is modeled by the celebrated ten Tusscher model. The linear and time-independent nature of the differential equations describing the electrical behavior of torso enables us to propose computationally efficient approaches. These include the condensation of the stiffness matrix for an entirely Finite Element-based approach and the hybrid Finite Element Method - Boundary Element Method (FEM-BEM) approach. In the former, owing to the linear behavior of the torso, the conductivity matrix of the surrounding tissue is constant and can be assembled once

and for all. Consequently, we can rearrange the overall coefficient matrix to decrease the total number of degrees of freedom. In the latter approach, we exploit the linear differential equation of the torso and solve it by using the BEM. The coupling between the nonlinear equations of cardiac tissue and the equations of the torso is achieved on the surface of the heart by the FEM-BEM approach. The efficiency of the proposed approaches is demonstrated through the representative numerical examples.

Keywords: FEM-BEM Coupling, Torso Modeling, Bidomain Models, ECG

ÖZ

BÜTÜNLEŞİK KALP ELEKTROFİZYOLOJİSİ PROBLEMİNE SAYISAL OLARAK ETKİN YAKLAŞIMLAR

Paşaoğlu, Özgür
Yüksek Lisans, İnşaat Mühendisliği Bölümü
Tez Yöneticisi : Doç. Dr. Serdar Göktepe

Ağustos 2017 , 103 sayfa

Bu tez çalışmasında, kalp elektrofizyolojisinde çift alan probleminin çözümü için sayısal olarak etkin yaklaşımlar önerilmektedir. Bu problemde, doğrusal olmayan kalp dokusu doğrusal bir iletken olarak kabul edilen gövde tarafında sarmalanmaktadır. Kalp dokusunun elektriksel uyarılması hücre zarı ve hücre dışı potansiyeline bağlı iken, gövdenin elektriksel uyarılması sadece hücre dışı potansiyeline bağlıdır. Kalp dokususun elektriksel davranışı iki ayrı kısmi diferansiyel denklem ile ifade edilmektedir. Bu denklemlerin ilki yüksek derecede doğrusal olmayan iyonik akım terimini içermektedir. Bu akımları matematiksel olarak modellemek için, yaygın olarak kullanılmakta olan ten Tusscher modeli seçilmiştir. Gövdeyi ifade eden diferansiyel denklemin doğrusal ve zamandan bağımsız yapısı bu problemin çözümü için sayısal olarak etkin yaklaşımların geliştirilmesine olanak sağlamaktadır. Bu yaklaşımların ilki, problemin tümüyle Sonlu Eleman Yöntemi ile çözümünde, çözüm matrisinin kümelenmiş hale getirilmesi, ikinci yaklaşım ise Sonlu Elemenlar Yöntemi ve Sınır Elemanlar Yönteminin (FEM-

BEM) hibrit bir şekilde kullanılmasıdır. İlk yöntemde, çevre dokunun iletkenlik matrisi gövdenin doğrusal iletken yapısı nedeni ile sabittir. Bu nedenle, bu yapıya ait matrislerin çözüm matrisinde bir defa derlenmesi yeterlidir. Ayrıca, oluşan çözüm matrisinin yeniden düzenlenmesiyle serbestlik derecelerinin azaltılması ve çözüm matrisinin küçültülmesi mümkün olmaktadır. Diğer yöntemde, doğrusal diferansiyel denklemden istifade edilerek BEM kullanılmıştır. Kalp dokusunun doğrusal olmayan denklemleri ile doğrusal gövde denklemlerinin bağlaşımı kalp yüzeyinde hibrit FEM-BEM yaklaşımı ile sağlanmıştır. Önerilen yöntemlerin etkinliği sayısal örnekler ile gösterilmiştir.

Anahtar Kelimeler: FEM-BEM Bağlaşımı, Gövde Modelleme, Çift Alan Modelleri, EKG

To my dearest

ACKNOWLEDGMENTS

Foremost, I would like to thank to my thesis supervisor Dr. Serdar Göktepe. His immense knowledge, insight, perspective and guidance made this study possible. There is no way to express my deepest appreciation to Dr. Serdar Göktepe.

I would like to thank to the members of my thesis examining committee; Dr. Kağan Tuncay, Dr. Ercan Gürses, Dr. Cüneyt Baykal and Dr. Besim Baranoğlu for their interests on my thesis topic and contributions to this study.

I am grateful to my roommates Şemsi Çoşkun, Müge Özgenoğlu, Korhan Kocamaz, Onur Solmaz, Aykut Bilginer, Sinan Fırat Dal, Berkay Akçören and Sepehr Seyedian Choubi for their support and patience during my thesis study.

I would also like to thank to my family for their unconditional love and support throughout my life.

Finally, I thank to two very special people, Ezgi Berberoğlu and Mehran Ghasabeh. When everything was upside down, they were with me to help me overcome all the difficulties. I am honored to have their support and I am very happy to have their love.

TABLE OF CONTENTS

ABSTRACT v

ÖZ vii

ACKNOWLEDGMENTS x

TABLE OF CONTENTS xi

LIST OF TABLES xiv

LIST OF FIGURES xv

LIST OF ABBREVIATIONS AND SYMBOLS xviii

CHAPTERS

1 INTRODUCTION 1

1.1 Motivation 1

1.2 Anatomy of the Human Heart 3

1.3 Electrical Conduction System of the Heart 5

1.4 Ionic Models for Cardiac Electrophysiology 9

1.5 Monodomain and Bidomain Settings 13

1.6 Electrocardiogram 15

1.7 The Torso and Its Numerical Manipulation 19

1.7.1 Condensation of the Stiffness Matrix 20

1.7.2 Boundary Element Method Coupling 20

1.8 Related Studies 20

1.9 Aim of the Thesis 22

1.10 Scope and Outline 23

2 GOVERNING DIFFERENTIAL EQUATIONS OF THE ELECTROPHYSIOLOGY 25

2.1 Monodomain Formulation 25

2.2 Bidomain Formulation 27

2.2.1 Reduction of the Bidomain Formulation 30

2.3 Linear Conductor Equation 31

2.4 Two Dimensional Setting of the Problem 31

3 ELECTROCHEMISTRY OF CARDIOMYOCYTES 35

3.1 Continuous Model Problem 35

3.1.1 Sodium Concentration and Related Variables . 41

3.1.2 Potassium Concentration and Related Variables 43

3.1.3 Calcium Concentration and Related Variables . 46

3.1.4 Calcium Concentration of the Sarcoplastic Reticulum and Related Variables 50

3.2 Local Discretization of the Model Problem 50

4 DISCRETIZATIONS AND NUMERICAL IMPLEMENTATIONS 53

4.1 Finite Element Discretization of the Bidomain Model . . 53

4.2 Condensation of the Solution Matrix 59

4.3 The Boundary Element Method and the FEM-BEM Coupling 61

5 NUMERICAL EXAMPLES 69

5.1 Determination of the Mesh Size 69

5.1.1 Appropriate Mesh Size for the Heart Domain . 71

5.1.2 Appropriate Mesh Size for the Torso Domain . 73

5.2 Appropriate Time Step for the Analysis 75

5.3 ECG Simulations 77

5.3.1 Healthy ECG 81

5.3.2 Modeling the Inferial Infarction 85

6 CONCLUSION 95

REFERENCES 97

LIST OF TABLES

TABLES

Table 2.1 Parameters of the integrated electrophysiology equations . . . 34

Table 3.1 Chemo-electrical material parameters of human ventricular cardiomyocyte. 40

Table 5.1 Parameters of the integrated electrophysiology equations . . . 70

Table 5.2 Selected mesh sizes for the sensitivity analysis of the heart domain. 71

Table 5.3 Selected mesh sizes for the sensitivity analysis of the torso domain. 74

Table 5.4 Parameters for the Purkinje elements 80

Table 5.5 Solution times of FEM, C-FEM and FEM-BEM methods. . . 84

Table 5.6 FEM-BEM solution times with different numbers of outer line elements. 85

LIST OF FIGURES

FIGURES

Figure 1.1 The cross section of a healthy heart [1]. 4

Figure 1.2 The idealized action potential - time diagram of a cardiac cell and corresponding phase numberings (above) and the corresponding ionic movements between intracellular medium and the extracellular medium of each phase (below). 6

Figure 1.3 The electrical conduction system of the heart [2]. 7

Figure 1.4 Different action potential waveforms on the different zones of the heart [3]. 9

Figure 1.5 The circuit representation of the Hodgkin-Huxley model (left) and the cellular representation of the local ionic currents between the intracellular medium and the extracellular medium(right). 10

Figure 1.6 The action potential waveform obtained through the use of Hodgkin-Huxley model. 11

Figure 1.7 The action potential waveform obtained through the use of ten Tusscher ionic model [4]. 12

Figure 1.8 Circuit representation of the ionic model (left) and the cellular representation of the local ionic currents between the intracellular medium and the extracellular medium(right). 13

Figure 1.9 Circuit representation of the bidomain model. 14

Figure 1.10 The schematic ECG Waveform [5]. 16

Figure 1.11 Limb leads, Lead-I, Lead-II, Lead-III, placed on the body surface that form Einthoven's triangle (above) and the augmented limb leads, aVF, aVL, aVR (below) 17

Figure 1.12 ECG leads placed on the chest. 18

Figure 1.13 The 12-lead ECG diagram of a healthy heart [6]. 19

Figure 2.1 Illustration of the heart domain embedded in the torso domain. 32

Figure 4.1 Algorithmic box of the FEM solution. 60

Figure 4.2 Boundaries of the FEM-BEM coupling. 64

Figure 5.1 The structured 64×64 mesh including the torso and the heart elements. 72

Figure 5.2 Transmembrane potentials at point P for four different mesh sizes (left) and the potentials in the close-up (right). 73

Figure 5.3 Errors in conduction velocity as the normalized difference for mesh sizes h^h= 6 mm, h^h= 2 mm and h^h= 0.67 mm . The result of the finest mesh where h^h= 0.5 mm is taken as to be the reference result. 74

Figure 5.4 The extracellular potential at the point P (left) and the potentials in the close-up (right) for different mesh sizes. 75

Figure 5.5 A mesh geometry for the integrated electrophysiology problem. The mesh is composed of 36037 quadrilateral elements. 76

Figure 5.6 The extracellular potentials at the point P1 (left) and at point P2 (right) for different mesh sizes of the torso. 77

Figure 5.7 The action potential at point P (left) and the potentials in the close-up (right) for different time steps. 78

Figure 5.8 The extracellular potential changes at Point P (left) and the extracellular potentials in the close-up (right) for different time steps. 79

Figure 5.9 The extracellular potential at the point $P1$ (left) and close-up for different time steps. 80

Figure 5.10 Geometric settings of the mesh. 81

Figure 5.11 The Purkinje fibers placed on the mesh. 82

Figure 5.12 Zones of the human heart and the corresponding action potential waveforms. 83

Figure 5.13 The normalized ECG of a healthy heart computed with FEM, C-FEM and FEM-BEM. Units are mV in y direction and ms in x direction. 84

Figure 5.14 LEAD-I ECG (left) and close-up. Units are in mV in y direction and ms in x direction. 85

Figure 5.15 The transmembrane potential propagation through the healthy heart. 86

Figure 5.16 The extracellular potential contours on the body for the healthy case. 88

Figure 5.17 Normalized LEAD-I ECG obtained using FEM-BEM coupling with different numbers of outer line elements. Units are mV in y direction and ms in x direction. 89

Figure 5.18 The heart section with inferial infarction. 90

Figure 5.19 The propagation of the transmembrane potential through the infarcted heart. 91

Figure 5.20 The propagation of the extracellular potential through the infarcted heart. 92

Figure 5.21 The normalized ECG of the healthy heart (blue) and the ECG of the infarcted heart (red). Units are mV in y direction and ms in x direction. 93

LIST OF ABBREVIATIONS AND SYMBOLS

FEM	Finite element method
C-FEM	Condensed finite element method
FEM-BEM	Finite element method - boundary element method coupling
ECG	Electrocardiogram
RA	Right arm
LA	Left arm
LF	Left foot
AV	Atrioventricular node
SA	Sinoatrial node
Ca^{2+}	Calcium ion
K^{+}	Potassium ion
Na^{+}	Sodium ion
Φ	Transmembrane potential
Φ_e	Extracellular potential
Φ_i	Intracellular potential
$\mathcal{D}_e$	Extracellular medium
$\mathcal{D}_i$	Intracellular medium
$\mathcal{B}^H$	Heart domain
$\mathcal{B}^T$	Torso domain
Γ	Interface between the heart and the torso
$\mathcal{X}$	Aspect ratio of the membrane surface to volume of the tissue
C_m	Membrane capacitance per unit area
f^{Φ}	Electrical source term
$\boldsymbol{D}$	Total conductivity tensor
$\boldsymbol{D}_i$	Intracellular conductivity tensor
$\boldsymbol{D}_e$	Extracellular conductivity tensor
$\boldsymbol{D}_T$	Conductivity tensor of the torso
$d^i_{\parallel}$	Intracellular conductance in the longitudinal direction

$d^i_\perp$	Intracellular conductance in the orthogonal direction
$d^e_\parallel$	Extracellular conductance in the longitudinal direction
$d^e_\perp$	Extracellular conductance in the orthogonal direction
d^T_{iso}	Isotropic conductance of the torso
θ	Fiber orientation angle
q_i	Intracellular potential flux
q_e	Extracellular potential flux
q_T	Potential flux of the torso
n_H	Unit normal surface vector of the heart
n_T	Unit normal surface vector of the torso
I_{Na}	Fast sodium current
I_{bNa}	Background sodium current
I_{NaK}	Sodium-potassium pump current
I_{NaCa}	Sodium-calcium exhanger current
I_{K1}	Inward rectifier current
I_{Kr}	Rapid delayed rectifier current
I_{Ks}	Slow delayed rectifier current
I_{pK}	Plateau potassium current
I_{t0}	Transient outward current
I_{CaL}	L-type calcium current
I_{bCa}	Background calcium current
I_{pCa}	Plateau calcium current
I_{leak}	Leakage current
I_{up}	Uptake current
I_{rel}	Release current of the sarcoplastic reticulum
c_{Na}	Sodium concentration
c_K	Potassium concentration
c_{Ca}	Calcium concentration
c^{sr}_{Ca}	Calcium concentration of the sarcoplastic reticulum

CHAPTER 1

INTRODUCTION

In this study, numerically efficient approaches for the solution of the bimaterial model, consisting of the heart and the torso, are proposed. In order to test the performance of these approaches, the mathematical model of cardiac electrophysiology is solved together with the mathematical model of the torso. Then, the representative results comparing the proposed approaches are demonstrated. The purpose of Chapter 1 is to introduce the anatomical and mathematical concepts of the corresponding problem in a systematic way. Therefore, first the motivation for this study is given. After brief motivation, the background information about the anatomy and electrical conduction system of the heart is provided. Then, the mathematical models explaining the electrical structure of the heart and the torso are outlined along with the well-known diagnostic tool, the electrocardiagram. Finally, to highlight the novelty of this work, related studies will be summarized briefly.

1.1 Motivation

The understanding of the underlying mechanisms of physical, chemical, or biological systems and their modeling using mathematical tools have been the major concern of human-being for centuries. Lately, the advances in computer science and technology allow us to develop realistic mathematical models of natural processes and to deal with highly complex systems. Owing to physical, chemical, and biological balance equations, applied mathematics and the powerful computational tools, researchers and scientists can now use simulations. Consequently, different branches of science come together to develop more sophisticated and

realistic simulation tools of these complex systems.

One of the interdisciplinary fields using simulations is the mathematical modeling of cardiac electrophysiology and cardiac electromechanics. Due to the difficulty of experimental studies in practical medicine, there is a great need for the mathematical models that explain the nature of the heart. These models help researchers understand the nature of healthy cardiovascular system of the living bodies. Modeling various dysfunctional cases, on the other hand, provides a mean to classify and understand the problems occuring in the heart. With the use of these mathematical simulations, new diagnostic and therapeutic approaches can be developed by cardiologists and researchers from different disciplines.

Due to several reasons, the cardiovascular system is more popular than other physiological systems in terms of mathematical modeling. For example, cardiac diseases are the major cause of death in the world. Cardiavascular diseases cause 3.9 million deaths in Europe annually, constituting 45% of all deaths per year [7]. Similarly, in the US, heart diseases caused 787,000 deaths in 2011 only, constituting 25% of all mortality [8]. Furthermore, heart diseases lead to high financial cost. In EU, overall cost of the cardiovascular diseases is around $250 billion per year. 53% of this cost is health care costs, while 26% of it is productivity losses, and 21% of it is informal care [9].

The key risk factors for heart disease are high blood pressure, high cholesterol, and smoking. Other than these factors, diabetes, physical inactivity, excessive alcohol consumption are also reasons of heart disease [10]. There are several treatments for various cardiovascular diseases. For example, for problems related to the heart valves, medications, and heart valve surgery are proposed. For arrhythmia, pacemakers may be implemented. Moreover, for the heart attack, coronary angioplasty or coronary artery bypass graft surgery are suggested [11]. Despite the fact that there are several treatments, driving reasons of the cardiovascular diseases cannot be avoided in the modern life. That is why, the number of people with high blood pressure is doubled since 1975 and reached to 1.13 billion. Moreover, the expected annual mortality caused by heart disease is

expected to be 23.3 million in 2030 [12]. Because of these facts and estimations, advanced treatment and diagnosis techniques will be highly significant to save lives and increase the life quality of people in the upcoming years.

In the last decade, with the power of computational tools and the advances in mathematical modeling of the cardivascular system, new therapeutic methods are proposed. Also, diagnostic tools are improved according to the results obtained from the simulations. Furthermore, with the recent techniques of image processing and data management, patient specific heart models are spreading around the world [13]. Individualization of the mathematical models helps the medical doctors treat the disease of each specific patient accurately. Also, with the individualization, cardiac diseases can be detected more quickly and these diseases can be treated timely. However, detection of all sorts of diseases for a wide range of heart geometries is still a challenging task [14]. Therefore, the effects of diseases on diagnostic tools like the pressure-volume curves and the electrocardiograms (ECG) should be investigated in detail for all kinds of cases with the simulation tools. For this reason, accurate physical definitions, generalization of the heart geometries, and efficient mathematical and numerical tools are required to improve the individualization techniques. The motivation of this study is to propose numerically efficient methods to decrease the solution time of the forward problem of electrophysiology for the integrated heart models including the torso.

1.2 Anatomy of the Human Heart

The heart is a muscular organ that forces the blood to move in the arteries and capillaries of the human body. This system that involves the heart and the network of veins, and arteries is the circulatory system. There are two parts of the circulatory system. First one is the systemic circulation where the main duty of the heart is to continuously provide oxygen and nutrients to the rest of the body. Second part is the pulmonary circulation where the oxygen-poor blood is pushed to the lungs in which it is refreshed with the oxygen. The heart is the center of these circulation systems and it works as an electromechanical

pump. The well-coordinated contraction of the chambers of the heart provides the circulation of the blood. By the systemic circulation, the cells, tissue, and organs are supplied with life-sustaining sources. On the other hand, the cellular wastes including the carbondioxide are removed from the body with the pulmonary circulation.

The heart is located on the slightly left side of the middle of the chest between the two lungs and behind the strenum. The size of the heart is about that of an average clenched adult fist. The longitudinal cross section and anatomy of a healthy heart is depicted in Figure 1.1.

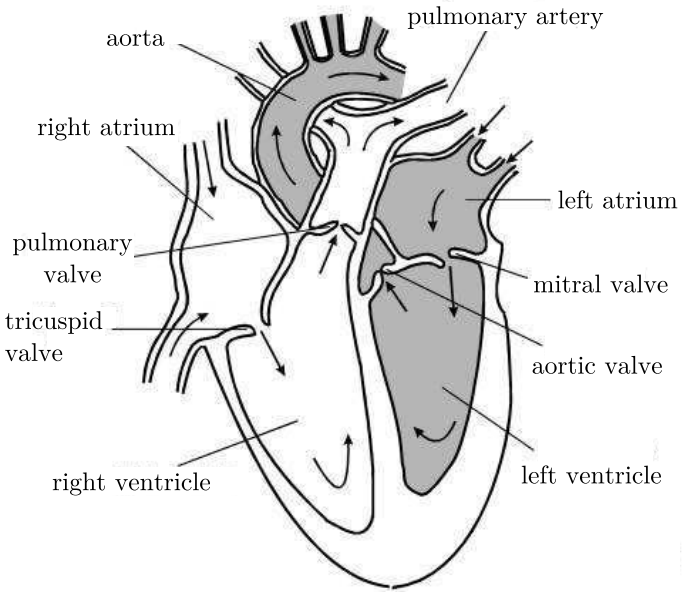

Figure 1.1: The cross section of a healthy heart [1].

The upper part of the heart is called the base and the lower tip is called the apex. There are four chambers working in harmony. The upper chambers are called the atria and the lower chambers are called the ventricles. The atria and ventricles are separated from each other by a strong wall named atrioventricular septum. Right and left parts of the heart, on the other hand, are separated by the septum. The chambers have a vital role in the cardiac cycle. The deoxygenated blood is collected in the right two chambers of the heart, whereas the oxygenated blood is collected in the left two chambers. The upper two chambers

of the heart, the right atrium and the left atrium, receive the incoming blood and push it to the ventricles. The left ventricle, being the strongest muscle of all four, pumps the oxygenated and nutrient-rich blood to the rest of the body via the aorta. The right ventricle pushes the de-oxygenated and nutrient-poor blood to the lungs via the pulmonary artery. Other than chambers, there are valves that provides harmony between these chambers. The four valves, the aortic valve, the tricuspid valve, the pulmonary valve, and the mitral valve provide a perfect timing for the blood flow between the chambers, veins, and arteries. These valves are uni-directional and ensure the blood flow to be in one direction only. During the contraction of a chamber, if the blood pressure exceeds the threshold pressure of a valve, this valve opens and the blood starts to flow out of that chamber. The tricuspid valve separates the right atrium and the right ventricle. The mitral valve separates the left atrium and the left ventricle. The pulmonary and aortic valves, on the other hand, hold the blood in the ventricles until it develops a sufficient pressure to reach to the lungs and all other parts of the body, respectively, see [15, 16, 17].

1.3 Electrical Conduction System of the Heart

The heart functions as a mechanical pump in the circulatory system. This mechanical power is actually a result of an excitation-contraction coupling. The heart is a biologically electro-active material that can convert an electrical stimulus into a mechanical power and can undergo large deformations. Therefore, the electrical conduction system has an important role in the cardiac cycle [18].

Contraction of a muscle is the result of ionic changes in the cellular level. Inside a muscle cell, calcium ions ($[Ca]^{2+}$) are the regulators that determine the mechanical behavior of the corresponding cell. The excitation, also referred as depolarization, alters the ionic balance inside the cell and triggers chemical reactions. In the content of the heart physiology, this electrical activity is defined as the action potential, also known as the transmembrane potential. In the upper graph of Figure 1.2, the schematic transient of the transmembrane potential of a single cell is presented. As can be seen from the Figure 1.2, there are four

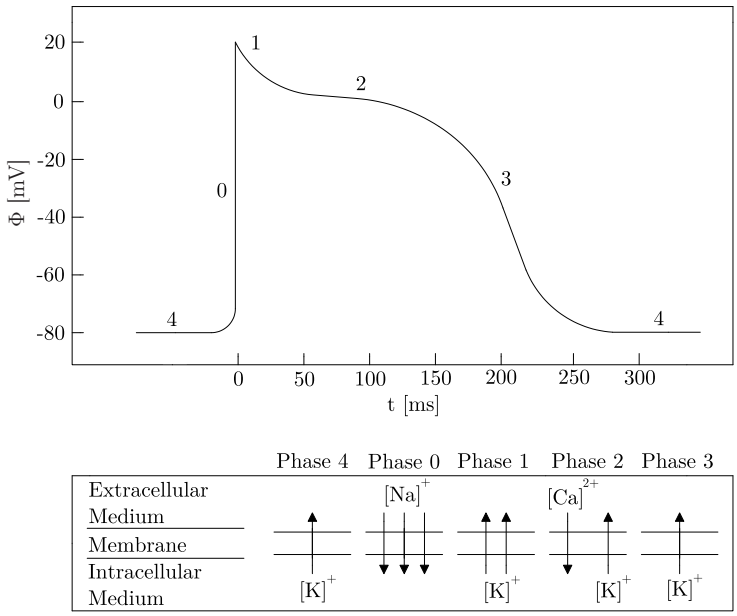

Figure 1.2: The idealized action potential - time diagram of a cardiac cell and corresponding phase numberings (above) and the corresponding ionic movements between intracellular medium and the extracellular medium of each phase (below).

phases that define the overall action potential waveform. Phase 4 is known as the resting state. The resting potential of a cardiac cell is about -80 mV. In the cardiac cycle, after excitation, the action potential eventually returns to its resting state. This is one of the characteristic features of this electrical activity. Phase 0 is the excitation part of the cardiac cell. If the cell is disturbed with a threshold potential, around -40 mV, the action potential increases up to +20 mV, instantaneously [19]. The reason of this sudden increase is that after the excitation, the sodium ($[Na]^+$) channels which are placed on the cell membrane, open. Opening of these channels causes a sudden inflow of $[Na]^+$ current from the extracellular medium [20]. This phase is called the depolarization phase. The ionic changes during Phase 0 and other phases are illustrated in the lower panel of Figure 1.2. Phase 1 is another characteristic feature of the waveform, since, there is a sudden drop, namely the overshoot, of the action potential. Once the $[Na]^+$ current increases suddenly, the cell reacts to the sudden change and the potassium ($[K]^+$) channels open to regulate the intracellular potential.

This opening causes an outflow of $[K]^+$ ions to the extracellular medium. As a result, the action potential decreases to 0 mV and the cell gets into a temporarily balanced state. This state is denoted by Phase 2 and is called the plateau phase. During this part, $[Ca]^{2+}$ ions start to inflow but they are in equilibrium with $[K]^+$ ions outflowing. Therefore, the action potential remains stationary for a certain amount of time. It is worth noting that, in this part, $[Ca]^{2+}$ ions flow into the intracellular medium of the cardiac cell and initiate the mechanical contraction process. Finally, in Phase 3, all of the channels except the outflowing $[K]^+$ channels, are closed. This phase is called the repolarization phase, and due to very slow outflow of the current, the action potential decreases gradually. During this phase, the ionic balance is satisfied more slowly. At the end of the repolarization phase, the cell returns back to its resting state and gets prepared for a new cycle of excitation. One excitation cycle takes around 300 ms, although it depends on the physiological state of a person and the location of the excited cell in the heart [21].

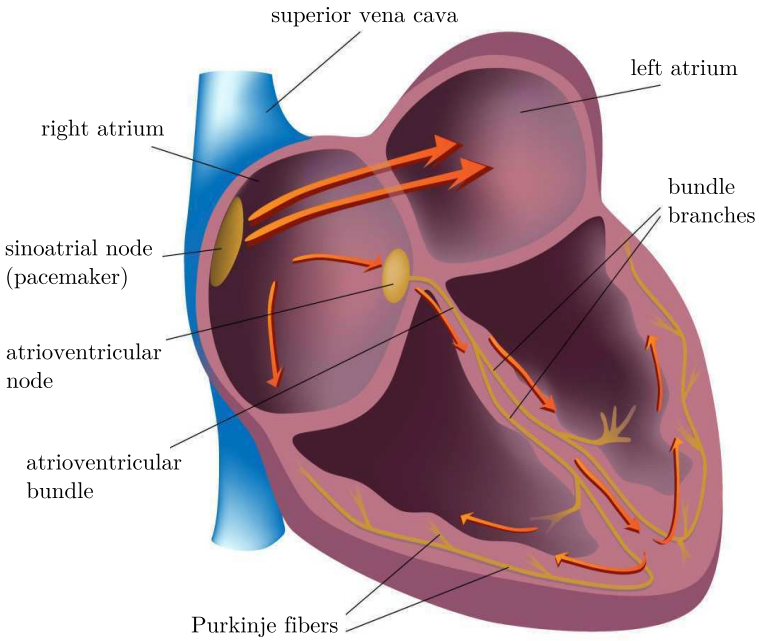

Figure 1.3: The electrical conduction system of the heart [2].

The action potential evolution is a cell-based evolution. The diffusion of the action potential throughout the heart cells is controlled by different specialized

muscle cells. These cells are shown in Figure 1.3. The sinoatrial node (SA) cells are the pacemaker cells; that is, they are self-excitatory cells. They can generate action potentials at a rate about 60 per minute. These cells are located at the upper wall of the right atrium. Once the action potential is generated by the SA node, it propagates through the atrial cells with a velocity of 1 m/s. During this propagation, the atria start to contract and eventually push the blood to the ventricles. The action potential, however, cannot propagate through the ventricles, because, the atrioventricular septum between the the atria and the ventricles acts as an isolator. The atrioventricular node (AV), on the other hand, is the electrical connection between the atria and the ventricles. The propagation speed of the action potential slows down to a velocity of 0.05 m/s in these cells. With this delay, the contraction of the atria is waited to be completed. Then, following the atrioventricular bundle, the potential starts to propagate through the ventricles. First, it follows two major branches placed on both sides of the septum. These branches are called the bundle branches. Via the bundle branches, the action potential propagates through the septum. These branches split into fibers that diverges through the endocardial parts of the ventricle walls. These fibers are called the Purkinje fibers and the conduction velocity of these cells are almost 3.5 m/s. Once the action potential reaches to these fibers, it instantaneously diffuses through the inner parts of the ventricular walls, exciting all the ventricle cells quickly.

It is also important to state that different regions of the heart has different conduction velocities and also different action potential evolution characteristics. In Figure 1.4, different peak values of the action potential, different plateau durations and the overall timings are provided for several zones of the heart. Moreover, the delay between the initiation times of the cells can be observed. The action potential variations are the result of different initial ionic concentrations of the corresponding zones. The initiation starts with the SA node and the potential propagates downwards until the action potential reaches to the apex of the heart. For further information on the electrical system of the heart, the reader is referred to [22, 23, 24].

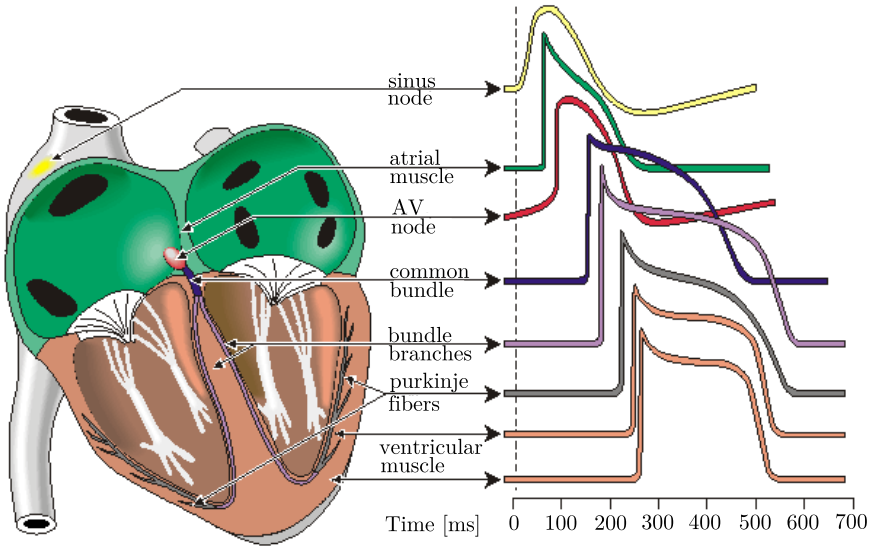

Figure 1.4: Different action potential waveforms on the different zones of the heart [3].

1.4 Ionic Models for Cardiac Electrophysiology

To conduct simulations of the electrophysiology of the heart, a mathematical model describing the experimental action potential waveform is required. About a half a century ego, Alan Hodgkin and Anrew Huxley proposed the first model that successfully mimics the time-dependent behavior of eletro-active cells, i.e. nerves [25]. They used a squid giant axon to explain the ionic relations between the extracellular and intracellular media. Despite the fact that this mathematical model was constructed for the nerve cells, it is proven to be very effective when used to model the myocardium cells as well. The evolution equation they suggested is

$$\mathcal{I}_{app} = \mathcal{C}_m \dot{\Phi} + \mathcal{I}_{ion} \tag{1.1}$$

where $\mathcal{C}_m$, $\mathcal{I}_{ion}$, and $\mathcal{I}_{app}$ are the membrane capacity, summation of all ionic currents through the membrane and the external current applied to the cell. Moreover, Φ denotes the action potential of the medium. The ohmic model for this ordinary differential equation is provided in Figure 1.5 (left). On right hand

side of the same figure, the cellular representation of the governing currents is illustrated. In this representation $\mathcal{D}_\mathrm{i}$ and $\mathcal{D}_\mathrm{e}$ stand for the intracellular domain and the extracellular domain, respectively. In this model, the major currents I_{Na}, I_K, I_l are the currents depending on $[\mathrm{Na}]^+$ concentration, $[\mathrm{K}]^+$ concentration, and other minor ionic concentrations, respectively. Moreover, I_l denotes the leakage current.

Overall membrane current, $\mathcal{I}_{ion}$, is then defined as

$$\mathcal{I}_{ion} = I_{Na} + I_K + I_l. \tag{1.2}$$

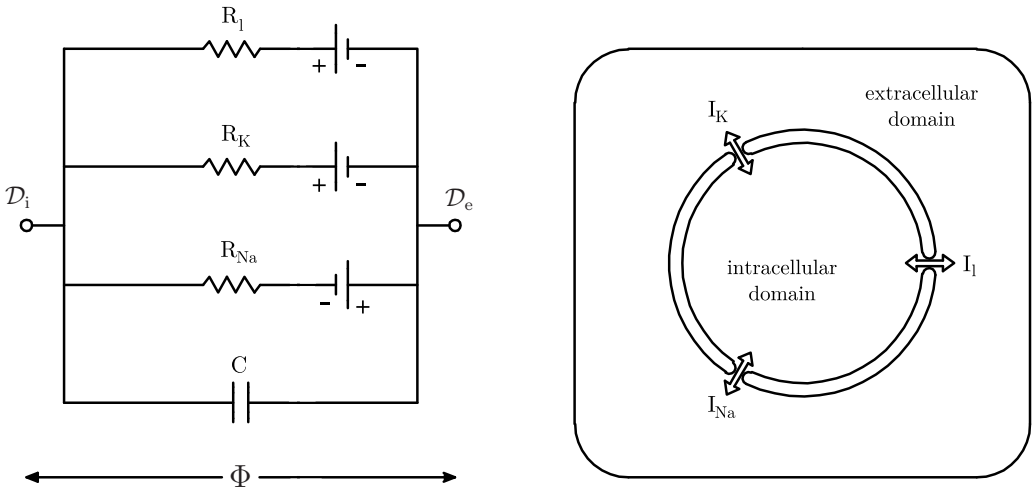

Figure 1.5: The circuit representation of the Hodgkin-Huxley model (left) and the cellular representation of the local ionic currents between the intracellular medium and the extracellular medium(right).

The model can be summarized that in the absence of an external potential, the action potential evolution depends on the local currents through the membrane, while the capacitor reflects the time dependent behavior of the potential. For further information about the equations of the local currents of this system and the derivation of these equations, the reader is referred to [25]. The ionic currents in this model are governed by two major ionic concentrations, $[\mathrm{Na}]^+$ and $[\mathrm{K}]^+$. Also, the effects of minor currents are taken into account with the leakage current.

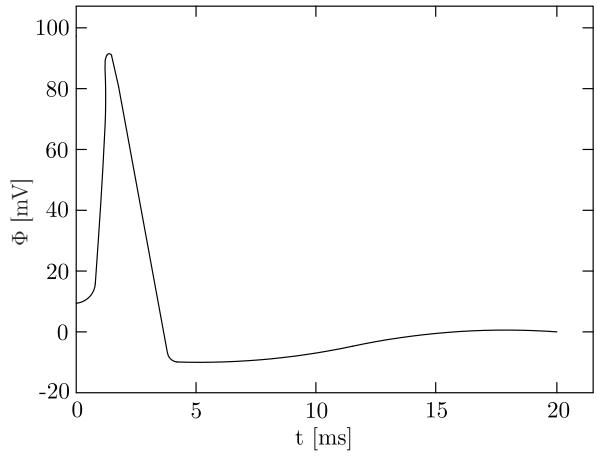

Figure 1.6: The action potential waveform obtained through the use of Hodgkin-Huxley model.

The action potential evolution obtained through Hodgkin-Huxley model is provided in Figure 1.6. It can be observed that this model predicts the overall behavior of the action potential cycle very well. The depolarization, the repolarization, and the resting state of the model is well constructed. After the publication of this Nobel-winning model, similar studies have been conducted to be able to mimic the action potential of the myocardium with a higher level of detail and accuracy. The FitzHugh-Nagumo equations for pacemakers [26], Yanagihara equations [27], Luo and Rudy model [28, 29] , Noble model for Purkinje fibers [30] and, the distinguished Aliev-Panfilov model [31] are the major mathematical models constructed so far.

A relatively new model was introduced by ten Tusscher [4, 32, 33, 34]. This model is here referred as the ionic model for the cardiac electrophysiology. The model incorporates the effects of the ionic concentrations with high accuracy. Figure 1.7 depicts the action potential waveform obtained through the ten Tusscher ionic model. It can be observed from Figure 1.7 that the model mimics all 4 phases, the depolarization, the overshoot, the plateau, and the repolarization, of the action potential effectively. Also, the possibility to change the ionic parameters of the model makes it favorable, since it allows to alter the peak action potentials, timings and resting potentials for different cases. Its applicability to pharmacological studies is another superiority of the model. Moreover, the ac-

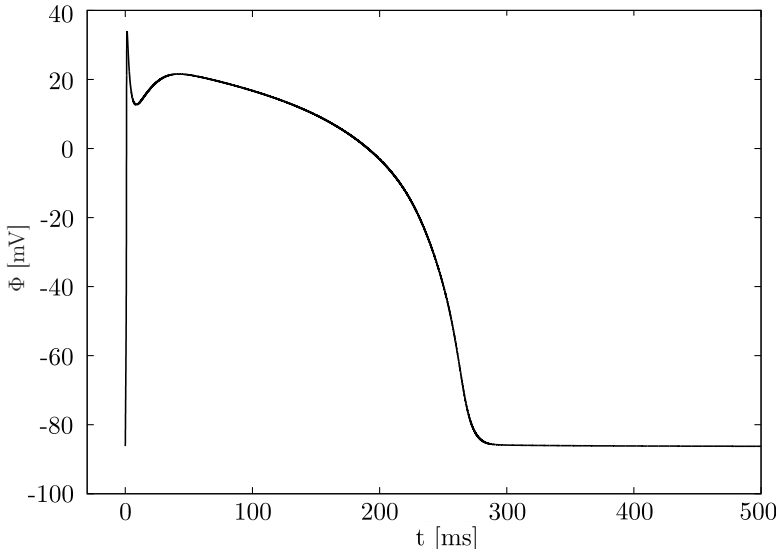

Figure 1.7: The action potential waveform obtained through the use of ten Tusscher ionic model [4].

curate prediction of the transient $[Ca]^{+2}$ in the cell makes this model applicable for electromechanical studies [18].

Different from the Hodgkin-Huxley model, the ionic model is governed by 4 ion concentrations, C_{Na}, C_K, C_{Ca}, C_{Ca}^{Sr}, that are the sodium concentration, the potassium concentration, the calcium concentration, and the calcium concentration in the sarcoplastic reticulum, respectively. There are also 13 gating variables and 15 ionic currents that define the local evolutions of this model. It should be noted that the Hodgkin-Huxley model includes the effects of three concentrations and corresponding three ionic currents. The same procedure is extended in the ionic model for 17 variables and 15 ionic currents in total. For the analogy between the Hodgkin-Huxley model and the ionic model, Figure 1.8 may be examined. Figure 1.8 shows the schematic model on the left and the cellular analogy of the model on the right. This model simply states that the global problem is the same for the action potential calculation, while the local problem is now extended to 15 ionic currents.

I_{Na}, I_{bNa}, I_{NaK}, I_{NaCa} are the sodium-related currents, I_{K1}, I_{Kr}, I_{Ks}, I_{NaK}, I_{pK}, I_{t0} are the potassium-related currents, I_{CaL}, I_{bCa}, I_{pCa}, I_{NaCa}, I_{leak}, I_{up}, I_{rel} are the calcium-related currents, and finally, I_{leak}, I_{up} and, I_{rel} are the calcium

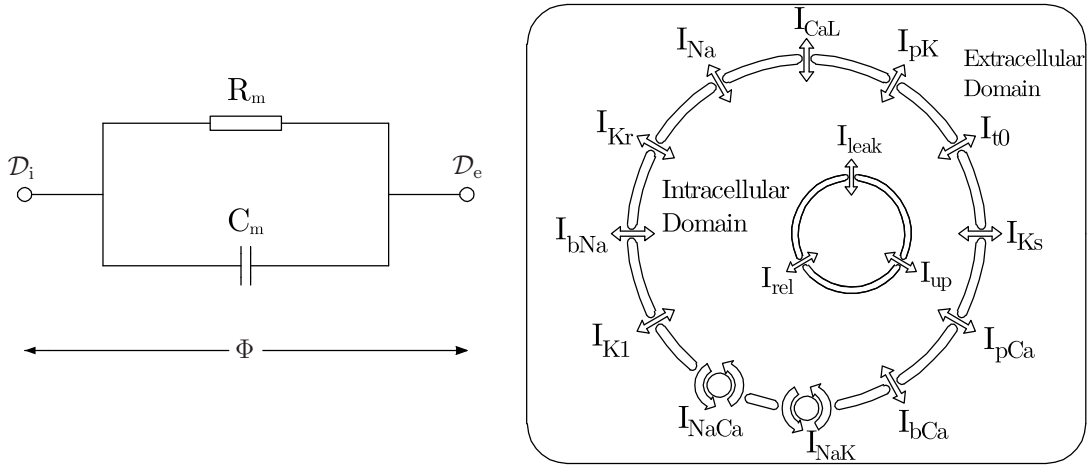

Figure 1.8: Circuit representation of the ionic model (left) and the cellular representation of the local ionic currents between the intracellular medium and the extracellular medium(right).

related currents of the sarcoplastic reticulum.

Eventually, $\mathcal{I}_{ion}$ contribution of this local problem is defined as

$$\begin{aligned} \mathcal{I}_{ion} = \quad & I_{Na} + I_{bNa} + I_{NaCa} + I_{K1} + I_{Kr} + I_{Ks} + I_{NaK} + I_{pK} + \\ & I_{t0} + I_{CaL} + I_{bCa} + I_{pCa} + I_{leak} + I_{up} + I_{rel}. \end{aligned} \tag{1.3}$$

In Chapter 3, a detailed explanation of the ionic model and its variables are provided. Also, for further information about the bioelectricity problem, the reader is referred to [35].

1.5 Monodomain and Bidomain Settings

The global degree of freedom of the cardiac electrophysiology is the action potential, Φ. However, the behavior of a single cardiac cell and several tens of cardiac cells differ [36, 37]. The monodomain and bidomain settings are two different approaches for the solution of the global electrophysiology problem of the heart. To be able to understand the difference between the monodomain and

bidomain models, the term domain should be explained. A domain refers to homogeneous macroscopic description, for example, of several tens of cells. With the bidomain model, macroscopic homogeneous medium is decomposed into two domains, namely the extracellular domain and the intracellular domain. This separation of domains is represented in Figure 1.9, with a circuit model.

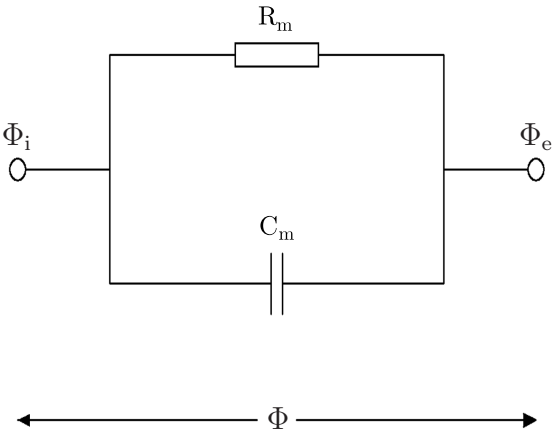

Figure 1.9: Circuit representation of the bidomain model.

In this setting, the transmembrane potential of the cardiac tissue is defined as the difference between the intracellular and extracellular potentials.

$$\Phi := \Phi_i - \Phi_e. \tag{1.4}$$

Here, Φ_i denotes the intracellular potential and Φ_e denotes the extracellular potential. It can be stated from the circuit model that the local problem of the model does not change [38]. The local problem of the bidomain setting is provided with the ionic model, mentioned in the previous section.

Moreover, the potential and current density in each of these two domains should satisfy the electrical current equilibrium. This equilibrium can be formulated with the two equations provided below:

$$\operatorname{div} \boldsymbol{q}_i = -i_T \quad \text{and} \quad \operatorname{div} \boldsymbol{q}_e = i_T, \tag{1.5}$$

where i_{T} is the transmembrane current, $\boldsymbol{q}_{\mathrm{i}}$ and $\boldsymbol{q}_{\mathrm{e}}$ are the intracellular and extracellular spatial potential fluxes, respectively.

With the bidomain approach, the homogenization of the two media is achieved. However, it is important to state that the conductivities and the propagation characteristics of the electrical potential in these two domains are completely different. In this setting, it is clear that even though the spaces are physically separated, the macroscopic intracellular and extracellular domains overlap at every point of the cardiac tissue [39]. As a result, at any point of the cardiac tissue, both of the global degrees of freedom exist simultaneously.

The monodomain model is the simplified version of the bidomain model. In the monodomain setting, the global degree of freedom is the transmembrane potential only. This causes the extracellular potential and its effects on the transmembrane potential to be neglected. Apart from the monodomain model, with the bidomain approach, the electrical activity of the extracellular domain can be taken into account. Furthermore, the effects of the external currents can be modeled with this approach. Therefore, it can be stated that the bidomain model is a superior setting in terms of reflecting the overall behavior of the cardiac potential.

1.6 Electrocardiogram

Electrocardiogram, commonly known as ECG, is used to assess the electrical activity of the heart. Since its invention by Willem Einthoven in the beginning of 1900s, it has been the most commonly used dignostic tool in clinical practice [40]. Compared to other clinical tools, ECG is relatively simple to measure and is a cheap, noninvasive tool. This makes it a distinguished medical tool that is required for almost all the patients who consult a doctor with a wide range of health problems.

Basically, ECG is the measurement of the electrical waves spreading through the atria and ventricles involving both the depolarization and the repolarization phases. Depending on the direction of the wave propagation and the different

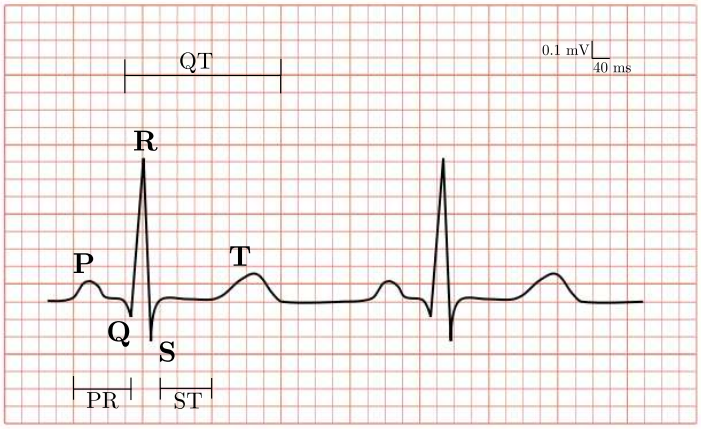

Figure 1.10: The schematic ECG Waveform [5].

cardiac zone characteristics, the recording of the electrical activity reveals specific intervals and waves, which are the main components of an ECG. Referring to Figure 1.10, ECG starts with the P wave, representing the depolarization of the atria, and followed by the isoelectric PQ interval representing the delay of the electrical waves at the atrioventricular (AV) node. This delay is significant for the proper functioning of the heart, providing the atria with the enough time to completely eject the blood into the ventricles. Propagation of the electrical waves through the ventricles causes the depolarization which is represented by a large triangular wave, named the QRS complex. Compared to P wave, QRS is considerably wider because of the differences in the muscle mass of atria and ventricles. The ST interval, which is the second isoelectric period on the ECG corresponds to the depolarized state of the both ventricles, or the plateau phase of the electrical activation on the cellular level. After the ventricles are fully depolarized, the repolarization phase starts and it is represented by the T wave on the ECG.

The ECG is obtained by measuring the electrical signals by using an array of electrodes placed at specific locations on the body surface covering the arms, legs, and the chest [41]. The potential differences between these leads are measured by a device and written in the standard 12-Lead ECG format. In this representation, the leads are classified into 3 types depending on their orien-

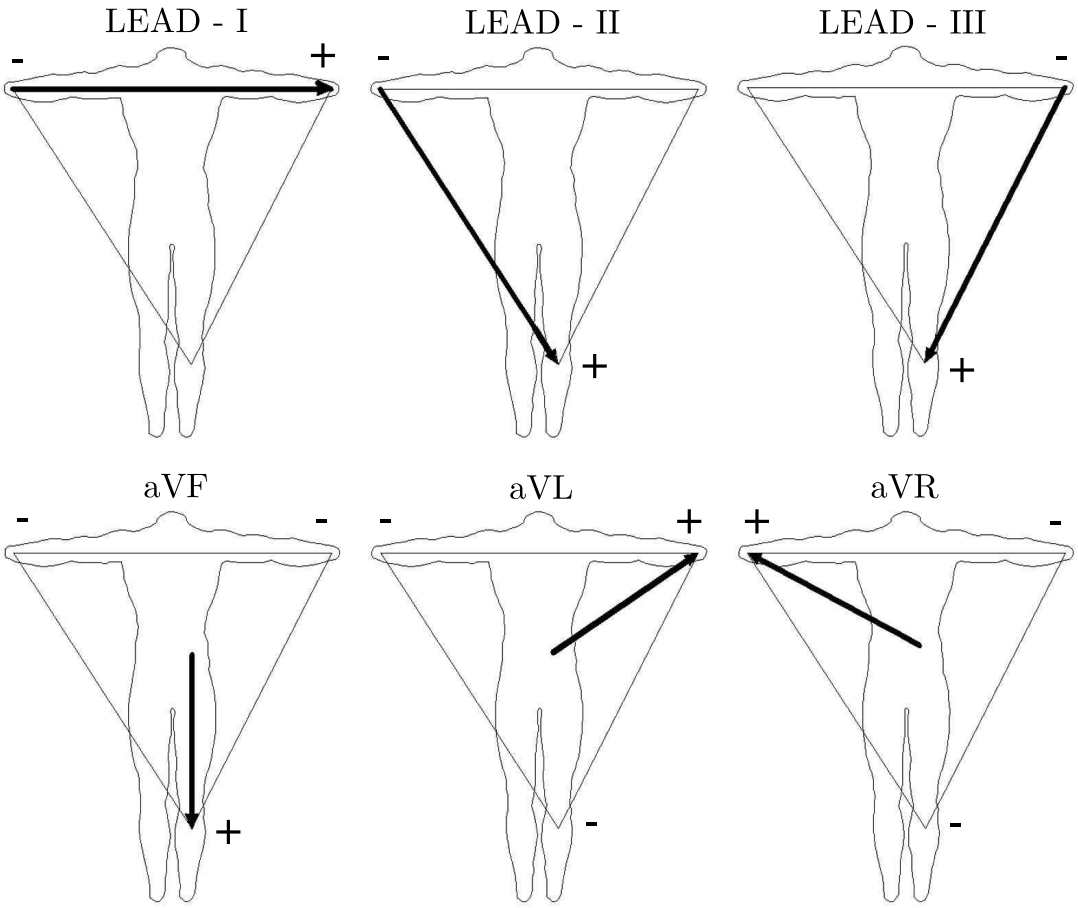

Figure 1.11: Limb leads, Lead-I, Lead-II, Lead-III, placed on the body surface that form Einthoven's triangle (above) and the augmented limb leads, aVF, aVL, aVR (below)

tation. These are the standard limb leads, augmented limb leads, and chest leads. For the standard limb leads, the placement of the positive and negative electrodes are shown in Figure 1.11 (top). For the augmented ones, Figure 1.11 (bottom), the positive electrodes are placed on left leg, left arm, and right arm for aVF, aVR, and aVR, respectively. Having the potential differences at hand, ECG is the obtained by printing them on a special paper. For a practical approach, the paper is divided into small grids, and the vertical interval of one square is 0.1 mV while the horizontal interval is 40ms. It is possible to explain the generation of ECG in terms of the projection of the heart vector, defined as the integration of the electrical impulses through the heart [42], onto the sagital and frontal planes represented in Figure 1.12. Depending on the projected plane,

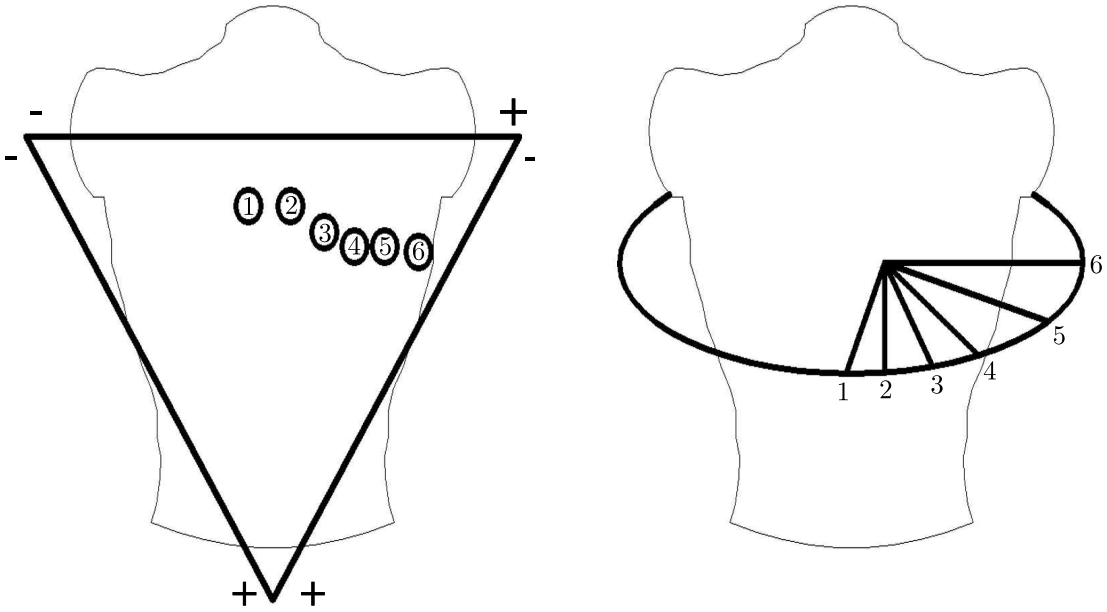

Figure 1.12: ECG leads placed on the chest.

components of the 12 lead ECG representation is obtained. The ECG example of a healthy heart is provided in Figure 1.13 where the characteristic P,Q,R,S and T waves can be observed.

Certain changes in the duration, morphology, or amplitude of these phases and intervals are accepted as strong indicators of cardiac dysfunctions. For example, the dysfunctions related with the atria, namely left or right lateral enhancements, bilateral enhancement etc., are generally revealed on P wave, while any distortion on PR interval is related with the problems of wave propagation between atria and ventricles, such as AV conduction block. The proper functioning of the ventricles, responsible for the pumping the blood through the pulmonary and systemic circulation, is of vital importance for the life and any disturbances in the electrical conduction system of the ventricles are directly observed as distortion of QRS wave. These dysfuntions cover a wide range of pathological cases; myocardial infarction, ventricular hypertrophy, and bundle brach blocks, to name a few. While ST segment position is the most widely accepted indication for the diagnosis of ventricular ischemia, indications on T waves are generally related with repolarization properties and supports the diagnosis of the diseases

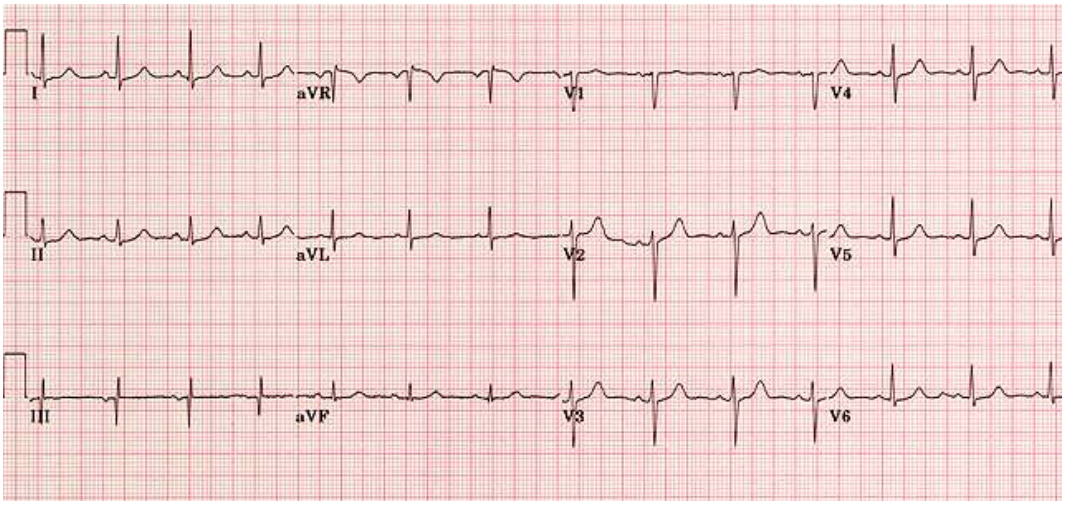

Figure 1.13: The 12-lead ECG diagram of a healthy heart [6].

such as bundle branch blocks, hypertropy, and conduction abnormalities. For a more detailed discussion on the diagnostic indications on ECG, the reader is referred to [43, 44, 45].

1.7 The Torso and Its Numerical Manipulation

The torso consists of tissue and organs including the heart that in this structure, is an electrically active material. It generates electric potential and transfers this electricity into surrounding tissue. The torso by its nature is assumed to be a linear conductor [46, 47]. The organs like liver, lungs, stomach possesses different electrical properties and conductivites. However, in this study, for simplicity we assumed the torso to be a linear, isotropic, and homogeneous conductor of electricity. The mathematical definition of the torso allows us to manipulate the numerical solution scheme of the problem. The two numerical approaches are explained in the following sections.

1.7.1 Condensation of the Stiffness Matrix

Owing to the linear and time-independent nature of the torso, its stiffness contributions are to the solution matrix are constant in FEM. Therefore, these contributions can be computed and stored at the beginning of the analysis. Consequently, we propose to rearrange the global solution matrix of the problem to decrease the total degrees of freedom. Eventually, we expect a faster solution because of the fact that the computational cost of the inversion of the condensed matrix is less. Moreover, there is no calculation of the stiffness terms of the linear part during the analysis. After the solution is obtained for the heart domain, the unknowns of the torso domain are recovered by using back-substitution. The details of the condensation are explained in Section 4.2.

1.7.2 Boundary Element Method Coupling

The boundary element method is a powerful mathematical tool that depends on the idea to solve the governing linear differential equation on the surface of the domain and using this information to compute the inner domain [48]. Using this method, the computational cost can be decreased drastically, because of the fact that when compared to the overall torso domain, the surface domain of the torso is much smaller, and as a result, the solution time of the problem decreases [49]. Using the BEM formulation, we exploited the BEM matrix to associate the heart surface fluxes in with the surface potentials of the torso. Using the staggered solution scheme, the coupling of the finite element method applied to the nonlinear myocardium and the boundary element method applied to the linear torso takes place on the interface nodes.

1.8 Related Studies

In this section, related studies to the present work are introduced. As mentioned earlier, ECG is a cheap, non-invasive and very efficient tool for the diagnosis of the heart problems. Therefore, there are several attempts to simulate the ECG

more accurately.

First, the heart reaction-diffusion models excluding the torso is one approximation for the ECG simulations [50, 51, 42, 52]. With this approach, the torso is ignored and only the nonlinear problem of the heart domain is solved with the FEM. The ECG is obtained by projecting the computed heart vector onto the sagital and frontal planes. In this approach, the effects of the torso on the heart is neglected. Owing to the finite element method and the bidomain setting of the cardiac domain, the anisotropy of the heart can be taken into account.

Second, the torso and the heart domains are discretized together and the overall domain is solved with the FEM [53, 54, 55, 56]. With this approach, the effects of the torso domain on the heart surface are taken into account. Furthermore, the FEM allows us to solve anisotropic and heterogeneous structure of the torso straightforwardly. This model associates the physical properties of the electrophysiology problem with the mathematical model efficiently [57]. However, due to the fact that the torso domain is much larger than the heart domain, the size of the problem and thus, the computational cost increase.

Third, the boundary element method can be employed for the solution of the linear differential equation of the torso. For the ECG simulations, the surface method BEM is quite applicable [58, 59, 60, 61]. The linear part is solved only on the outer surface of the torso domain. As a result, the size of the solution matrix and the solution time decrease [62]. The disadvantages of the BEM is that the memory requirement of the model during the analysis is high. Another disadvantage is the difficulty to model the heterogeneous and anisotropic cases of the torso domain. Recent studies focuses on the modeling of the anisotropic cases [63, 49, 64].

The BEM is a tool to model a linear domain. However, for the solution of this domain, a source model is required. This source model represents the electrical activity of the heart surface. The coupling of the source term with the BEM is another research area. Some models use static approaches [64, 65], whereas some use dynamic approaches [66]. Static approaches refer to the simulating the heart surface without coupling with the BEM. Then using the simulated results as

source term, computing the surface body potentials. Dynamic approaches refer to computing the heart surface potentials and the body surface potentials in a coupled form. Other source models are oblique dipole layer [67], and equivalent double layer approaches [68].

In this contribution, the torso is treated as a linear and isotropic conductor. The source model for the solution of the BEM is computed using the FEM for the nonlinear domain. Then, FEM and BEM are coupled dynamically on the heart surface, the interface. The contribution of the torso is converted into external flux terms on the heart surface. The boundary element matrix is implemented into the solution array of the nonlinear problem as an equivalent finite element contribution. Then, the staggered solution scheme is applied for the solution of the problem.

1.9 Aim of the Thesis

The aim of this thesis is to develop efficient numerical approaches for the solution of the integrated electrophysiology problem of the heart in the bidomain setting. In this contribution, the effect of the torso on the heart and the effect of the heart on the torso are examined. The problems of nonlinear electricity problem of cardiac tissue and linear electricity problem of the torso are solved together. One of the most important diagnostic tools of the cardiac practice is the electrocardiograms. The ECG leads are placed on the various parts of the body and they measure the electrical activity. Moreover, the direction of the currents provides us with a diagram defining the electrical activity of the heart. The mathematical models, on the other hand, only involve the electrical activity of the heart and ignore the effects of the torso. In this thesis, the effect of the torso on the ECG in the 2-D setting is also provided.

Moreover, the torso is the large portion of the body. As a result, for the numerical solution of the overall system, it increases the size of the solution matrix enormously. Therefore, exploiting the linear and time-independent nature of this conductor, we proposed efficient numerical methods to decrease the com-

putation time of the integrated electrophysiology problem in bidomain setting. The representative numerical examples are analyzed to illustrate the efficiency of the proposed approaches.

1.10 Scope and Outline

The thesis is structured as follows:

In Chapter 2, the governing differential equations in the monodomain and bidomain setting for the electrical problem are introduced. Furthermore, the linear governing differential equation of the torso is provided. Also, the boundary conditions of the integrated problem are defined.

In Chapter 3, the constitutive equations of the electrochemistry problem and their discretizations on the integration points are given.

In Chapter 4, the finite element formulation for the integrated cardiac electrphysiology problem is introduced. Moreover, two efficient numerical approaches for the solution of the corresponding problem are explained. Firstly, the condensation of the solution matrix is provided. Secondly, the boundary element method and finite element method coupling on the heart surface is represented.

In Chapter 5, the representative numerical examples are demonstrated. The performance of the proposed methods are shown with a comparison study using FEM, condensed FEM approach, C-FEM, and FEM-BEM. The ECG results of the proposed approaches and that of FEM are compared. The efficiency of the methods is demonstrated in terms of the solution time of the problem. Furthermore, the FEM-BEM coupling results for a diseased heart's ECG simulation, along with the fibrillation and defibrillation simulations are presented.

Lastly, in Chapter 6, the critical points of the present work are summarized.

CHAPTER 2

GOVERNING DIFFERENTIAL EQUATIONS OF THE ELECTROPHYSIOLOGY

The aim of this chapter is to introduce the fundamental equations of the electrophysiology of the heart and the linear electrical conductor. In Section 2.1, monodomain equations of the heart electrophysiology is provided. In Section 2.2, the extention of the monodomain formulation to the bidomain formulation is given. The governing equations of the linear conductor problem are presented in Section 2.3. Finally, in Section 2.4, boundary conditions and initial conditions of the bimaterial problem are given along with the overall parameter set of the global problem of the integrated cardiac electrophysisology.

2.1 Monodomain Formulation

In the monodomain model, the action potential is the unique field variable and is the only global degree of freedom of the heart domain, $\mathcal{B}^H$. The local state at material point $\boldsymbol{X}$ and at time t can then be defined as follows:

$$\text{State}(\boldsymbol{X}, t) := \{\Phi(\boldsymbol{X}, t)\}. \tag{2.1}$$

As mentioned earlier, the first quantitative model representing the electrophysiology of the excitable neural cell was proposed by Hodgkin and Huxley [25]. In their pioneering model, the local evolution of the transmembrane potential Φ is

represented by the equation

$$i_T = \mathcal{X}(\mathcal{C}_m\dot{\Phi} + \mathcal{I}_{ion}), \tag{2.2}$$

where i_T represents the summation of ionic and capacitive currents, $\mathcal{X}$ represents the aspect ratio of the membrane surface to volume of the tissue and $\mathcal{C}_m$ represents the membrane capacitance per unit area. Moreover, $\mathcal{I}_{ion}$ denotes the current density and is governed by the ionic movements through the membrane. Due to the nonlinearity of the ionic currents, this first order ordinary differential equation is nonlinear by its nature. The transmembrane current is balanced by the flux term

$$i_T = \operatorname{div} \boldsymbol{q}, \tag{2.3}$$

where, $\boldsymbol{q}$ is the spatial potential flux. The phenomenological form of the spatial potential flux $\boldsymbol{q}$ is specified as follows:

$$\boldsymbol{q} = \boldsymbol{D} \cdot \nabla\Phi \tag{2.4}$$

where $\boldsymbol{D}$ is the conductivity tensor and is defined, in general case of anisotropic diffusion, as follows:

$$\boldsymbol{D} = d_{\parallel}\boldsymbol{f} \otimes \boldsymbol{f} + d_{\perp}(\boldsymbol{I} - \boldsymbol{f} \otimes \boldsymbol{f}). \tag{2.5}$$

Here, $d_{\parallel}$ and $d_{\perp}$ denote conductances along the fibre direction and the orthogonal plane to it, respectively and the unit vector $\boldsymbol{f}$ stands for the fibre orientation vector in the 2-D space.

$$\boldsymbol{f} = \begin{Bmatrix} \cos\theta \\ \sin\theta \\ 0 \end{Bmatrix} \tag{2.6}$$

In this representation, θ stands for the orientation angle of the cardiac fibers. Then, inserting (2.3) into (2.2), we obtain

$$\mathcal{X}(\mathcal{C}_m\dot{\Phi} + \mathcal{I}_{ion}) = \operatorname{div} \boldsymbol{q}. \tag{2.7}$$

Using the definition (2.4) in (2.7) and rearranging the equation to recast into a more compact form, we obtain:

$$\dot{\Phi} = \operatorname{div}(\bar{\boldsymbol{D}} \cdot \nabla\Phi) + f^{\Phi}. \tag{2.8}$$

The normalized conductivity tensor $\bar{\boldsymbol{D}}$ in this equation is defined by

$$\bar{\boldsymbol{D}} := (\mathcal{X}\mathcal{C}_m)^{-1} \cdot \boldsymbol{D}. \tag{2.9}$$

The term f^{Φ} is the electrical source term and is a function of ionic currents. It is defined by

$$f^{\Phi} := -C_m^{-1}\mathcal{I}_{ion}. \tag{2.10}$$

2.2 Bidomain Formulation

In the previous section, the fundamental equation (2.8) of the monodomain model was explained. In the bidomain model, contrary to the monodomain model, the intracellular and extracellular potentials are the two independent global degrees of freedom. This separation allows us to solve extracellular potential, and by this way, investigate the effect of cardiac potential on the body and that of the body potential on the heart.

The state variables of the bidomain model at a material point $\boldsymbol{X}$ and at time t

are

$$\text{State}(\boldsymbol{X}, t) := \{\Phi_i(\boldsymbol{X}, t), \Phi_e(\boldsymbol{X}, t)\}. \tag{2.11}$$

The bidomain equations are reaction-diffusion equations of extracellular and intracellular media. The conservation law suggests that if there is no external current applied to the system, the total flux should be conserved.

$$\int_{\partial \mathcal{B}^H} \boldsymbol{q}_t \cdot \boldsymbol{n}\, dA = 0 \quad \text{and} \quad \boldsymbol{q}_t = \boldsymbol{q}_i + \boldsymbol{q}_e, \tag{2.12}$$

where $\boldsymbol{q}_i$ is the intracellular spatial potential flux, $\boldsymbol{q}_e$ is the extracellular spatial potential flux, and $\boldsymbol{n}$ is the unit normal vector of the surface, respectively. Then, the local form of (2.12) is

$$\operatorname{div} \boldsymbol{q}_t = 0. \tag{2.13}$$

If $\boldsymbol{D}_i$ is defined to be the intracellular conductivity tensor and $\boldsymbol{D}_e$ to be the extracellular conductivity tensor, the intracellular and extracellular potential fluxes can be represented as

$$\boldsymbol{q}_i = -\boldsymbol{D}_i \cdot \nabla \Phi_i \quad \text{and} \quad \boldsymbol{q}_e = -\boldsymbol{D}_e \cdot \nabla \Phi_e. \tag{2.14}$$

The intracellular $\boldsymbol{D}_i$, extracellular $\boldsymbol{D}_e$, and the total $\boldsymbol{D}$ conductance tensors are defined as

$$\begin{aligned} \boldsymbol{D}_i &= d^i_{\parallel} \boldsymbol{f} \otimes \boldsymbol{f} + d^i_{\perp}(\boldsymbol{I} - \boldsymbol{f} \otimes \boldsymbol{f}), \\ \boldsymbol{D}_e &= d^e_{\parallel} \boldsymbol{f} \otimes \boldsymbol{f} + d^e_{\perp}(\boldsymbol{I} - \boldsymbol{f} \otimes \boldsymbol{f}), \\ \boldsymbol{D} &= \boldsymbol{D}_i + \boldsymbol{D}_e. \end{aligned} \tag{2.15}$$

As mentioned in the monodomain model, $\boldsymbol{f}$ denotes the unit fibre direction vector represented in (2.6), $d^i_{\parallel}$, $d^i_{\perp}$, $d^e_{\parallel}$, and $d^e_{\perp}$ denote the intracellular conductances

along the fibre direction and the plane perpendicular to it, and the extracellular conductances along the fibre direction and the plane perpendicular to it, respectively.

Furthermore, we define the transmembrane potential as the potential difference between the intracellular domain and the extracellular domain, i.e.

$$\Phi := \Phi_i - \Phi_e. \tag{2.16}$$

Employing the pioneering equation of the Hodgkin and Huxley Model:

$$i_T = \mathcal{X}(\mathcal{C}_m \dot{\Phi} + \mathcal{I}_{ion}), \tag{2.17}$$

where, the transmembrane current i_T is a function of the intracellular and extracellular currents, in the bidomain setting. These currents are in equilibrium. Therefore, each subspace obeys the following equations:

$$\operatorname{div} \boldsymbol{q}_i = -i_T \quad \text{and} \quad \operatorname{div} \boldsymbol{q}_e = i_T. \tag{2.18}$$

Equations (2.13) and (2.18) introduce the strong form of the bidomain model of the cardiac electrophysiology. This equation system can be written in a more coherent form as:

$$\begin{aligned} \dot{\Phi} &= \operatorname{div}(\bar{\boldsymbol{D}}_i \cdot \nabla \Phi) + \operatorname{div}(\bar{\boldsymbol{D}}_i \cdot \nabla \Phi_e) + f^{\Phi}, \\ 0 &= -\operatorname{div}(\bar{\boldsymbol{D}}_i \cdot \nabla \Phi) - \operatorname{div}(\bar{\boldsymbol{D}} \cdot \nabla \Phi_e), \end{aligned} \tag{2.19}$$

where $\bar{\boldsymbol{D}}$ and $\bar{\boldsymbol{D}}_i$ are the normalized conductivity tensors, defined by

$$\begin{aligned} \bar{\boldsymbol{D}} &:= (\mathcal{X}\mathcal{C}_m)^{-1} \cdot \boldsymbol{D}, \\ \bar{\boldsymbol{D}}_i &:= (\mathcal{X}\mathcal{C}_m)^{-1} \cdot \boldsymbol{D}_i. \end{aligned} \tag{2.20}$$

The definition of the electrical source term f^{Φ} is provided in (2.10).

2.2.1 Reduction of the Bidomain Formulation

The coupled equations of the bidomain setting can be reduced to the monodomain setting with some simplifications. By inserting (2.14) into (2.13), and exploiting this equation, the following equation is obtained:

$$\nabla\Phi_i = \boldsymbol{D}^{-1}(\boldsymbol{D}_e\nabla\Phi - \boldsymbol{q_t}). \tag{2.21}$$

Implementing (2.21) into the first equation of (2.18), we end up with the ionic currents in terms of the transmembrane potential.

$$i_T = \mathrm{div}(\boldsymbol{D}_i\boldsymbol{D}^{-1}\boldsymbol{D}_e\nabla\Phi) - \mathrm{div}(\boldsymbol{D}_i\boldsymbol{D}^{-1}\boldsymbol{q_t}). \tag{2.22}$$

Owing to the conservation of total current flux, $\mathrm{div}\,\boldsymbol{q_t} = 0$, if the intracellular conductivity tensor and extracellular conductivity tensor are taken to be proportional, i.e. $\boldsymbol{D}_i = c\boldsymbol{D}_e$, where c is a constant, the right hand side of (2.22) drops. The resulting reduced equation can be inserted into (2.17) and recast into the following monodomain setting,

$$\mathcal{X}(\mathcal{C}_m\dot{\Phi} + \mathcal{I}_{ion}) = \mathrm{div}(\hat{\boldsymbol{D}}\cdot\nabla\Phi), \tag{2.23}$$

where effective monodomain conductivity tensor is defined as

$$\hat{\boldsymbol{D}} := \boldsymbol{D}_i(\boldsymbol{D}_i + \boldsymbol{D}_e)^{-1}\boldsymbol{D}_e. \tag{2.24}$$

This procedure provides a way to simplify the problem. However, the assumption of proportional intracellular and extracellular conductivity tensors is not accurate due to physical, and biological reasons.

2.3 Linear Conductor Equation

The bidomain setting of the heart electrophysiology consists of the field variables, the intracellular potential and the extracellular potential. The heart cells are specialized excitable cells that when they are perturbed with a threshold potential, they react in such a way that the cell depolarizes and repolarizes in a waveform illustrated in Figure 1.2. The same feature can be observed with the neural cells. The regular body cells, on the other hand, can react to external stimulus but cannot propagate a nonlinear transmembrane currents. Therefore, the only field variable of the torso domain $\mathcal{B}^T$ is the extracellular potential and the transmembrane potential $\Phi = 0$. The torso is assumed to be a linear, isotropic, and homogeneous conductor. Therefore, the governing equation representing this model is the Laplace Equation. It can be formulated as

$$-\operatorname{div}(\boldsymbol{D}_T \cdot \nabla \Phi_e) = 0. \tag{2.25}$$

Here, $\boldsymbol{D}_T$ represents the isotropic conductivity tensor of the torso.

$$\boldsymbol{D}_T = d_{iso}^T \boldsymbol{I}, \tag{2.26}$$

where the d_{iso}^T denotes the isotropic coefficient of conductivity. Eventually, the spatial potential flux of the torso can be obtained as

$$\boldsymbol{q}_T = -\boldsymbol{D}_T \cdot \nabla \Phi_e. \tag{2.27}$$

2.4 Two Dimensional Setting of the Problem

In this section, the boundary conditions, the initial conditions and the parameter set of the problem are provided. For a better representation, the two subdomains of the problem in two dimensional setting is illustrated in Figure 2.1 where $\mathcal{B}^H$ denotes the heart domain, $\mathcal{B}^T$ denotes the torso domain, and Γ denotes the

interface between the heart and the torso. The longitudinal cross-section of the heart is surrounded with the torso section. The heart domain contains the section of the ventricles only. Therefore, a line surface representing the atria surface is introduced to separate the torso domain from the inner parts of the heart. It is important to note that this separated region contains the blood, yet the effects of the blood is neglected. As a result, there is no domain in that enclosed zone. Therefore, on the surface surrounding that enclosed area, there are boundaries of both the heart $\mathcal{B}^H$ and the torso $\mathcal{B}_1^T$. The equations of the two problems are solved in the corresponding domains. On the interface, the equations of the heart and the torso are coupled. There are three boundaries and one interface in the provided setting.

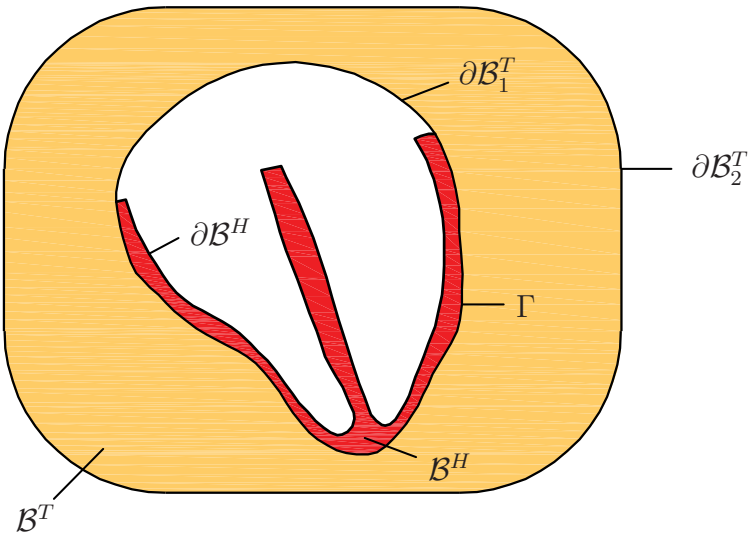

Figure 2.1: Illustration of the heart domain embedded in the torso domain.

There is no transmembrane potential in the torso domain. Therefore, the interface should satisfy two conditions. First condition is the continuity of the extracellular potential flux.

$$\boldsymbol{q}_e \cdot \boldsymbol{n}_H + \boldsymbol{q}_T \cdot \boldsymbol{n}_T = 0 \quad \text{on} \quad \Gamma, \tag{2.28}$$

where $\boldsymbol{q}_e$ represents the extracellular flux of the heart and $\boldsymbol{q}_T$ represents the flux of the torso. Moreover, $\boldsymbol{n}_H$ and $\boldsymbol{n}_T$ denote the unit normal surface vector of the heart and the unit normal surface vector of the torso, respectively. On the interface Γ, at a same point, these two vectors are aligned in the opposite directions. The second condition is the insulation of the intracellular flux. In the torso domain, the spatial potential flux of the intracellular domain is zero. Therefore, the interface should be impermeable to intracellular flux.

$$\boldsymbol{q}_i \cdot \boldsymbol{n}_H = 0 \quad \text{on} \quad \Gamma, \tag{2.29}$$

where $\boldsymbol{q}_i$ represents the intracellular flux.

On the boundary of the heart, the coupled bidomain equations lead to the following boundary conditions:

$$\begin{aligned} \boldsymbol{q}_{i,e} \cdot \boldsymbol{n}_H = \bar{\boldsymbol{q}}_{i,e} \quad &\text{on} \quad \partial\mathcal{B}_{\boldsymbol{q}}^H, \\ \Phi_{i,e} = \bar{\Phi}_{i,e} \quad &\text{on} \quad \partial\mathcal{B}_{\Phi}^H. \end{aligned} \tag{2.30}$$

On the boundaries of the torso, on the other hand, the Laplace equation leads to the boundary conditions of

$$\begin{aligned} \boldsymbol{q}_T \cdot \boldsymbol{n}_T = i_{app} \quad &\text{on} \quad \partial\mathcal{B}_{\boldsymbol{q}}^T, \\ \Phi_e = \bar{\Phi}_e \quad &\text{on} \quad \partial\mathcal{B}_{\Phi}^T. \end{aligned} \tag{2.31}$$

In this equation system, i_{app} denotes the external current applied the the boundary of the torso. Moreover, the initial conditions of the electrophysiology problem can be defined as following:

$$\begin{aligned} \Phi(0) = \bar{\Phi}_0 \quad &\text{at} \quad t = 0, \\ \Phi_e(0) = \bar{\Phi}_{e,0} \quad &\text{at} \quad t = 0. \end{aligned} \tag{2.32}$$

Finally, to complete the definition of the global problem of the integrated cardiac electrophysiology, the parameter set is provided in Table 2.1. There are four

conductivity parameters of the heart domain, one conductivity parameter of the torso domain, and one orientation angle of the heart fibers that define the global equation of the bimaterial problem.

Table 2.1: Parameters of the integrated electrophysiology equations

Parameter	Unit	Description	Equations
$\bar{d}^i_\parallel := d^i_\parallel / \mathcal{X}\mathcal{C}_m$	$[\mathrm{mm}^2/\mathrm{s}]$	Normalized intracellular conductance of the heart in the longitudinal direction	(2.15, 2.20)
$\bar{d}^i_\perp := d^i_\perp / \mathcal{X}\mathcal{C}_m$	$[\mathrm{mm}^2/\mathrm{s}]$	Normalized intracellular conductance of the heart in the orthogonal direction	(2.15, 2.20)
$\bar{d}^e_\parallel := d^e_\parallel / \mathcal{X}\mathcal{C}_m$	$[\mathrm{mm}^2/\mathrm{s}]$	Normalized extracellular conduction of the heart in the longitudinal direction	(2.15, 2.20)
$\bar{d}^e_\perp := d^e_\perp / \mathcal{X}\mathcal{C}_m$	$[\mathrm{mm}^2/\mathrm{s}]$	Normalized extracellular conductance of the heart in the orthogonal direction	(2.15, 2.20)
d^T_{iso}	$[\mathrm{mm}^2/\mathrm{s}]$	Isotropic conductance of the torso	(2.26)
θ	[Rad]	Fiber orientation angle of the heart tissue	(2.6)

The global problem of the bimaterial problem of the cardiac electrophysiology is provided in Chapter 2. However, the local source term f^Φ still needs to be specified for the full description of the problem. In Chapter 3, the constitutive equations of the ionic model for the human cardiomyocytes are provided along with the discretization of these equations at the integration points.

CHAPTER 3

ELECTROCHEMISTRY OF CARDIOMYOCYTES

The aim of this chapter is to introduce the governing equations of the chemical problem for ventricular cardiomyocytes [4]. Moreover, the temporal discretization of these equations on the integration points are presented, according to the work by Wong, Göktepe, and Kuhl [34].

The global equations of the bidomain model are introduced in Chapter 2. The calculation of the source term f^{Φ} in (2.19) is presented in this section. The chemical part of the electrochemical coupling in cardiac tissue is characterized through a system of ordinary differential equations. The local solution field of this system involves n_{gate} gating variables and n_{ion} ion concentrations. In Section 3.1, the cellular gating variables, the ion concentrations, and the ionic currents are defined and the continuous formulation of the model is represented. In Section 3.2, the time discretization and the associated iterative update scheme of the local solution field at the integration points are provided.

3.1 Continuous Model Problem

The continuous formulation of the chemical problem is defined in terms of two sets of first order ordinary differential equations. These sets correspond to n_{gate}=13 gating variables and c_{ion}=4 ion concentrations. This system of equations is solved iteratively and the updated variables are stored at the integration points at each time step.

The first set of equations is for the gating variables. Gating variables are the quantitative indicators of the ionic state of a cell. Depending on the instanta-

neous state of a cell, the ion channels have different permeability characteristics, that is, they have a time-dependent nature. For example, if sodium concentration in the cell increases suddenly, channels that are permeable to sodium start to close gradually, while the channels, which regulate the sodium-dependent ions, such as potassium, start to open. Channels may be open for a specific state of the cell or they start to close for a certain ion concentration in the cell and so on. Gating variables, as a whole, quantitatively represent the overall states of all channels. In the ten Tusscher model [4], there are 13 gating variables and 10 of these variables depend only on the transmembrane potential, whereas the other 3 variables depend on both the transmembrane potential and the corresponding ion concentration. Therefore, it makes sense to separate these two groups of variables into two subsets, $\boldsymbol{g}^{I}_{gate} = [g_m,\, g_h,\, g_j,\, g_{xr1},\, g_{xr2},\, g_{xs},\, g_r,\, g_s,\, g_d,\, g_f]$ and $\boldsymbol{g}^{II}_{gate} = [g_{xK1\infty},\, g_{fCa},\, g_g]$. These two subsets define the gating variables, which is the first set of the problem.

The second set of equations is for the ion concentrations. In human ventricles, generally, sodium, potassium, and calcium are the major ion concentrations. In addition to these concentrations, the calcium concentration of the sarcoplastic reticulum is included in this model. These 4 ion concentrations, $\boldsymbol{c}_{ion} = [c_{Na},\, c_K,\, c_{Ca},\, c^{sr}_{Ca}]$, define the second set, whose elements c_{Na}, c_K, c_{Ca} and c^{sr}_{Ca} denote the sodium concentration, the potassium concentration, the calcium concentration and the calcium concentration of the sarcoplastic reticulum, respectively. The details of these 17 variables defining the local problem are explained in the following sections.

The two subsets of the evolution of the gating variables are defined through the following equations.

$$\begin{aligned} \dot{g}^{I}_{gate} &= f^{gI}_{gate}(\Phi, g^{I}_{gate}) = \frac{1}{\tau^{I}_{gate}(\Phi)}[g^{\infty I}_{gate}(\Phi) - g^{I}_{gate}], \\ \dot{g}^{II}_{gate} &= f^{gII}_{gate}(\Phi, g^{II}_{gate}, c_{ion}) = \frac{1}{\tau^{II}_{gate}(\Phi)}[g^{\infty II}_{gate}(\Phi, c_{ion}) - g^{II}_{gate}], \end{aligned} \tag{3.1}$$

where I=1,..,10 gating variables of the first set, and II=11,12,13 gating variables of the second set. These equations are derived through the Hogkin-Huxley

model. Therefore, there are two constants that characterize them. The first one is g_{gate}^{∞} which quantifies the steady state conductance of the gate. The second one, τ_{gate}, is a temporal parameter that represents the characteristic time for a gate to reach its steady state. The second set of ordinary differential equations is defined by the following equations

$$\dot{\boldsymbol{c}}_{ion} = \boldsymbol{f}_{ion}^{c}(\Phi, \boldsymbol{g}_{gate}, \boldsymbol{c}_{ion}). \tag{3.2}$$

It can be deduced from (3.2) that the evolution equations of the ion concentrations depend on the transmembrane potential, the gating variables, and the ion concentrations themselves. Because of the fact that some of the gating variables depend on the ion concentrations and ion concentrations depend on some of the gating variables, this equation system is a tightly coupled system. Therefore, iterative solution procedure is chosen. The details of the solution procedure are given in Section 3.2.

The chemical problem of the cardiac tissue involves n_{crt}=15 ionic currents depending on the gating variables and the ion concentrations. These ionic currents can be expressed in terms of the transmembrane potential, the gating variables, and the ion concentrations.

$$\boldsymbol{I}_{crt} = \boldsymbol{I}_{crt}(\Phi, \boldsymbol{g}_{gate}, \boldsymbol{c}_{ion}). \tag{3.3}$$

The set of ionic currents for cardiac tissue is $\boldsymbol{I}_{crt} = [I_{Na},\ I_{bNa},\ I_{NaK},\ I_{NaCa},\ I_{K1},\ I_{Kr},\ I_{Ks},\ I_{pK},\ I_{t0},\ I_{CaL},\ I_{bCa},\ I_{pCa},\ I_{leak},\ I_{up},\ I_{rel}]$ where I_{Na} denotes the fast sodium current, I_{bNa} is the background sodium current, I_{NaK} designates the sodium potassium pump current, I_{NaCa} symbolizes the sodium calcium exchanger current, I_{K1} stands for the inward rectifier current, I_{Kr} shows the rapid delayed rectifier current, I_{Ks} denotes the slow delayed rectifier current, I_{pK} is the plateau potassium current, I_{t0} symbolizes the transient outward current, I_{CaL} designates the L-type calcium current, I_{bCa} shows the background calcium current, I_{pCa} stands for the plateau calcium current, I_{leak} is the leakage current, I_{up} denotes the uptake current of the sarcoplastic reticulum, and finally

I_{rel} stands for the release current of the sarcoplastic reticulum. The amount of these currents through the cell membrane depends on the corresponding gating variables, the ion concentrations, and the transmembrane potential. The solution of the complex system of the ionic currents, the gating variables, and the ion concentrations enables us to specify the instantaneous state of the cell. The sodium related currents, I_{Na}, I_{bNa}, I_{NaK} and I_{NaCa}, for example, alters the sodium concentration of the cell. The dependencies of the sodium-related currents is given in the following form

$$\begin{aligned} I_{Na} &= \hat{I}_{Na}(\Phi, g_m, g_h, g_j, c_{Na}), \\ I_{bNa} &= \hat{I}_{bNa}(\Phi, c_{Na}), \\ I_{NaK} &= \hat{I}_{NaK}(\Phi, c_{Na}), \\ I_{NaCa} &= \hat{I}_{NaCa}(\Phi, c_{Na}, c_{Ca}). \end{aligned} \tag{3.4}$$

The current I_{Na} is gated by the sodium activation gate g_m, the fast sodium inactivation gate g_h, and the slow sodium inactivation gate g_j. The potassium-related currents can be listed as follows.

$$\begin{aligned} I_{K1} &= \hat{I}_{K1}(\Phi, g_{K1}^{\infty}, c_K), \\ I_{Kr} &= \hat{I}_{Kr}(\Phi, g_{xr1}, g_{xr2}, c_K), \\ I_{Ks} &= \hat{I}_{Ks}(\Phi, g_{xs}, c_{Na}, c_K), \\ I_{pK} &= \hat{I}_{pK}(\Phi, c_K), \\ I_{t0} &= \hat{I}_{t0}(\Phi, g_r, g_s, c_K). \end{aligned} \tag{3.5}$$

The current I_{K1} is gated by inward recrification factor g_{K1}^{∞}, I_{Kr} is gated by the inward rectifiers channels g_{xr2} and g_{xr1}, I_{Ks} is gated by the delayed rectifier channel g_{xs}. Moreover, the slowly delayed rectifier channels g_r and g_s are gating I_{t0}. These currents alter the potassium concentration of the cell. Lastly, the

calcium-dependent currents can be given in the form,

$$\begin{aligned} I_{CaL} &= \hat{I}_{CaL}(\Phi, g_d, g_f, g_{fCa}, c_{Ca}), \\ I_{bCa} &= \hat{I}_{bCa}(\Phi, c_{Ca}), \\ I_{pCa} &= \hat{I}_{pCa}(c_{Ca}), \\ I_{leak} &= \hat{I}_{leak}(c_{Ca}^{sr}, c_{Ca}), \\ I_{up} &= \hat{I}_{up}(c_{Ca}), \\ I_{rel} &= \hat{I}_{rel}(g_d, g_g, c_{Ca}^{sr}). \end{aligned} \tag{3.6}$$

Here, the transient outward channels g_d, g_f, g_{fCa} are gating I_{CaL}. Furthermore, g_d and g_g are gating the sarcoplastic reticulum current I_{rel}. These calcium related currents alter the calcium concentration in the cell and the calcium concentration in the sarcoplastic reticulum.

The concentration-dependent potentials of sodium, potassium, and calcium are computed using the Nernst equation,

$$\Phi_{ion} = \frac{RT}{z_{ion}F} \ln\left(\frac{c_{ion0}}{c_{ion}}\right) \quad \text{with} \quad \Phi_{ion} = [\Phi_{Na}, \Phi_K, \Phi_{Ca}]. \tag{3.7}$$

Table 3.1: Chemo-electrical material parameters of human ventricular cardiomyocyte.

	sodium related	potassium related	calcium related	calcium^{sr} related
concentrations	$c_{Na0} = 140\,mM$	$c_{K0} = 5.4\,mM$	$c_{Ca0} = 2\,mM$	-
maximum currents	$I_{NaCa}^{max} = 1000\,pA/pF$ $I_{NaK}^{max} = 1.362\,pA/pF$	$I_{NaK}^{max} = 1.362\,pA/pF$	$I_{NaCa}^{max} = 1000\,pA/pF$ $I_{leak}^{max} = 0.08\,s^{-1}$ $I_{up}^{max} = 0.425\,mM/s$ $I_{rel}^{max} = 8.232\,mM/s$	$I_{leak}^{max} = 0.08\,s^{-1}$ $I_{up}^{max} = 0.425\,mM/s$ $I_{rel}^{max} = 8.232\,mM/s$
maximum conductances	$C_{Na}^{max} = 14.838\,nS/pF$ $C_{bNa}^{max} = 0.00029\,nS/pF$	$C_{K1}^{max} = 5.405\,nS/pF$ $C_{Kr}^{max} = 0.0096\,nS/pF$ $C_{Ks,\,epi}^{max} = 0.245\,nS/pF$ $C_{Ks,\,endo}^{max} = 0.245\,nS/pF$ $C_{Ks,\,M}^{max} = 0.062\,nS/pF$ $C_{pK}^{max} = 0.0146\,nS/pF$ $C_{t0,\,epi}^{max} = 0.294\,nS/pF$ $C_{t0,\,endo}^{max} = 0.073\,nS/pF$ $C_{t0,\,M}^{max} = 0.294\,nS/pF$	$C_{CaL}^{max} = 0.175mm^3/[\mu Fs]$ $C_{bCa}^{max} = 0.000592\,nS/pF$ $C_{pCa}^{max} = 0.825\,nS/pF$	
half saturation constants	$c_{CaNa} = 1.38\,mM$ $c_{NaCa} = 87.50\,mM$ $c_{KNa} = 1.00\,mM$ $c_{NaK} = 40.00\,mM$	$c_{KNa} = 1.00\,mM$ $c_{NaK} = 40.00\,mM$	$c_{CaNa} = 1.38\,mM$ $c_{NaCa} = 87.50\,mM$ $c_{pCa} = 0.0005\,mM$ $c_{up} = 0.00025\,mM$ $c_{rel} = 0.25\,mM$ $c_{buf} = 0.001\,mM$	$c_{up} = 0.00025\,mM$ $c_{rel} = 0.25\,mM$ $c_{buf}^{sr} = 0.3\,mM$
other parameters	$k_{NaCa}^{sat} = 0.10$ $\gamma_{NaCa} = 2.50$ $\gamma = 0.35$	$p_{KNa} = 0.03$	$\gamma_{rel} = 2$ $c_{tot} = 0.15\,mM$	$\gamma_{rel} = 2$ $c_{tot}^{sr} = 10\,mM$

gas constant	R	$= 8.3143\,J\,K^{-1}\,mol^{-1}$	temperature	T	$= 310\,K$	cytoplasmic volume	V	$= 16404\mu m^3$
Faraday constant	F	$= 96.4867\,C/mmol$	membrane capacitance	C	$= 185\,pF$	sarcoplastic reticulum volume	V^{sr}	$= 1094\mu m^3$

With this equation, the balance potential that would be generated by a particular ion is computed. In this case, the cell is assumed to be permeable to the corresponding ion only. The constants used in the Nernst Equation are R = 8.3143 $JK^{-1}mol^{-1}$ for gas constant, T = 310K for absolute temperature, F = 96.4867 C/mmol for Faraday constant. z_{ion} is 1 for single-charged ions, like sodium and potassium and is 2 for double charged calcium ions. All other constants of the problem provided in Table 3.1. The units used in this model are milliseconds for time and millivolts for the action potential. Furthermore, the conductances are given in nanosiemens per picofarad, the ion concentrations in millimoles per liter, the ionic currents through the membrane in picoamperes per picofarad and the ionic currents of the sarcoplastic reticulum in millimolar per millisecond.

Eventually, the source term f^{Φ} in (2.19) is then defined as follows:

$$\begin{aligned} f^{\Phi} = -[&I_{Na} + I_{bNa} + I_{NaK} + I_{NaCa} + I_{K1} + I_{Kr} + \\ &I_{Ks} + I_{pK} + I_{t0} + I_{CaL} + I_{bCa} + I_{pCa}]. \end{aligned} \tag{3.8}$$

In the next sections, the relations between the ion concentrations, the gating variables and the ionic currents are quantified for sodium-, potassium-, calcium-dependent quantities.

3.1.1 Sodium Concentration and Related Variables

Sodium ions are responsible for the depolarization of the action potential. If the threshold value is exceeded with a threshold potential, then the sodium channels open and the potential of the intracellular domain starts to increase rapidly. Then, once the cell reaches to peak value of around +20 mV, the sodium channels close and the flow of the sodium is balanced by the flow of the potassium.

Four currents alter the concentration of the sodium inside the cell. Two of these currents are responsible for the sudden increase of the action potential. These currents are I_{Na}, the fast sodium and I_{bNa}, the background sodium currents.

Other two currents, on the other hand, are the I_{NaK}, sodium potassium and I_{NaCa}, sodium calcium pumps. These currents regulate the intracellular potential of the cell, if the cell is positively charged. The evolution of the sodium concentration is then,

$$\dot{c}_{Na} = -\frac{C}{VF}[I_{Na} + I_{bNa} + 3I_{NaK} + 3I_{NaCa}], \tag{3.9}$$

where C is the membrane capacitance per unit surface area and V denotes the cytoplasmic volume. The constants are provided in Table 3.1. Sodium related currents are defined as follows

$$\begin{aligned}
I_{Na} &= C_{Na}^{max} g_m^3 g_h g_j [\Phi - \Phi_{Na}]\,, \\
I_{bNa} &= C_{bNa}^{max} [\Phi - \Phi_{Na}]\,, \\
I_{NaK} &= \frac{I_{NaK}^{max}[c_{K0}c_{Na}][[c_{Na} + c_{NaK}][c_{K0} + c_{KNa}]}{[1 + 0.1245e^{-0.1\Phi F/RT} + 0.0353e^{-\Phi F/RT}]]}\,, \\
I_{NaCa} &= \frac{I_{NaCa}^{max}[e^{\gamma\Phi F/RT}c_{Na}^3 c_{Ca0} - e^{(\gamma-1)\Phi F/RT}c_{Na0}^3 c_{Ca}\gamma_{NaCa}]}{[[c_{NaCa}^3 + c_{Na0}^3][c_{CaNa} + c_{Ca0}][1 + k_{NaCa}^{sat}e^{(\gamma-1)\Phi F/RT}]]}\,.
\end{aligned} \tag{3.10}$$

The gating variables in these equations are computed using the Hodgkin-Huxley Equations $\dot{g}_{gate} = [g_{gate}^{\infty}$ - $g_{gate}]/\tau_{gate}$.

The sodium activation gate evolves according to,

$$\begin{aligned}
\dot{g}_m &= [g_m^{\infty} - g_m]/\tau_m \qquad \text{with} \\
g_m^{\infty} &= \frac{1}{[1 + e^{(-56.86-\Phi)/9.03}]^2}\,, \\
\tau_m &= \frac{0.1}{[1 + e^{(-60-\Phi)/5}][[1 + e^{(\Phi+35)/5}]} + \frac{1}{[1 + e^{(\Phi-50)/200}]]}\,.
\end{aligned} \tag{3.11}$$

The evolution of the fast sodium inactivation gate is given by,

$$\begin{aligned}
\dot{g}_h &= [g_h^\infty - g_h]/\tau_h \qquad \text{with} \\
g_h^\infty &= \frac{1}{[1+e^{(\Phi+71.55)/7.43}]^2}, \\
\tau_h &= \begin{cases} 0.1688[1+e^{-(\Phi+10.66)/11.1}], & \text{if } \Phi \geq -40 \\ \dfrac{1}{[0.057e^{-(\Phi+80)/6.8}+2.7e^{0.079\Phi}+3.1\cdot 10^5 e^{0.3485\Phi}]}, & \text{if } \Phi < -40 \end{cases}
\end{aligned} \tag{3.12}$$

The slow sodium inactivation gate varies according to

$$\dot{g}_j = [g_j^\infty - g_j]/\tau_j \quad \text{with} \quad g_j^\infty = \frac{1}{[1+e^{(\Phi+71.55)/7.43}]^2} \quad \text{and} \quad \tau_j = \frac{1}{[\alpha_j+\beta_j]}, \tag{3.13}$$

where

$$\alpha_j = \begin{cases} 0 & \text{if } \Phi \geq -40, \\ \dfrac{[-2.5428\cdot 10^4 e^{0.2444\Phi} - 6.948\cdot 10^{-6} e^{-0.04391\Phi}]}{[\Phi+37.78][1+e^{0.311(\Phi+79.23)}]} & \text{if } \Phi < -40 \end{cases}$$

$$\beta_j = \begin{cases} \dfrac{0.6e^{0.057\Phi}}{[1+e^{-0.1(\Phi+32)}]} & \text{if } \Phi \geq -40, \\ \dfrac{0.02424e^{-0.01052\Phi}}{[1+e^{-0.1378(\Phi+40.14)}]} & \text{if } \Phi < -40. \end{cases}$$

3.1.2 Potassium Concentration and Related Variables

The sodium, after the stimulation of the cell, tends to inflow through the cell. On the contrary, the potassium ions try to leave the cell due to diffusive chemical force. The potassium plays a role in 4 phases of the action potential curve. The outflow of the potassium ions after the depolarization causes the overshoot which is governed by the current I_{t0}, the transient outward current. The slow

and rapid rectifier currents balances the inflowing calcium ions and creates the plateau phase. The transient potassium concentration is provided below:

$$\dot{c}_K = -\frac{C}{VF}[I_{K1} + I_{Kr} + I_{Ks} - 2I_{NaK} + I_{pK} + I_{t0} + I_{stim}]. \tag{3.14}$$

The evolution of the potassium is governed by 4 ionic currents the inward rectifier current, the rapid rectifier current, transient outward current and the slow rectifier current. Other than these currents, the plateau current of potassium, the sodium potassium pump and the stimulus current play a role in the behavior of the potassium ions. These currents are defined specifically in the following form:

$$\begin{aligned}
I_{K1} &= C_{K1}^{max} g_{K1}^{\infty}[c_{K0}/5.4]^{1/2}[\Phi - \Phi_K], \\
I_{Kr} &= C_{Kr}^{max} g_{xr1} g_{xr2}[c_{K0}/5.4]^{1/2}[\Phi - \Phi_K], \\
I_{Ks} &= C_{Ks}^{max} g_{xs}^2[\Phi - \Phi_{Ks}], \\
I_{NaK} &= \frac{I_{NaK}^{max}[c_{K0}c_{Na}][[c_{Na} + c_{NaK}][c_{K0} + c_{KNa}]}{[1 + 0.1245e^{-0.1\Phi F/RT} + 0.0353e^{-\Phi F/RT}]}, \\
I_{pK} &= C_{pK}^{max}[1 + e^{[25-\Phi]/5.98}]^{-1}[\Phi - \Phi_K], \\
I_{t0} &= C_{t0}^{max} g_r g_s[\Phi - \Phi_K].
\end{aligned} \tag{3.15}$$

I_{Ks} is a function of the potential which represents the reversal potential $\Phi_{Ks} = \frac{RT}{F} \cdot \log([c_{k0} + p_{KNa}c_{Na0}][c_K + p_{KNa}c_{Na}]^{-1})$.

I_{K1} is characterized through explicit form of the time-independent inward rec-

tification factor g_{K1}^{∞},

$$\begin{aligned} g_{K1}^{\infty} &= \alpha_{K1}[\alpha_{K1}+\beta_{K1}]^{-1} \qquad \text{with} \\ \alpha_{K1} &= \frac{0.1}{[1+e^{0.06(\Phi-\Phi_K-200)}]}, \\ \beta_{K1} &= \frac{[3e^{0.0002(\Phi-\Phi_K+100)}+e^{0.1(\Phi-\Phi_K-10)}]}{[1+e^{-0.5(\Phi-\Phi_K)}]1}. \end{aligned} \tag{3.16}$$

The rapid delayed rectifier current is gated by the activation gate g_{xr1},

$$\begin{aligned} \dot{g}_{xr1} &= [g_{xr1}^{\infty}-g_{xr1}]/\tau_{xr1} \qquad \text{with} \\ g_{xr1}^{\infty} &= [1+e^{(-26-\Phi)/7}]^{-1}, \\ \tau_{xr1} &= 2700[1+e^{(-45-\Phi)/10}]^{-1}[1+e^{(\Phi+30)/11.5}]^{-1} \end{aligned} \tag{3.17}$$

and by the inactivation gate g_{xr2},

$$\begin{aligned} \dot{g}_{xr2} &= [g_{xr2}^{\infty}-g_{xr2}]/\tau_{xr2} \qquad \text{with} \\ g_{xr2}^{\infty} &= \frac{1}{[1+e^{(\Phi+88)/24}]}, \\ \tau_{xr2} &= \frac{3.36}{[1+e^{(-60-\Phi)/20}][1+e^{(\Phi-60)/20}]}. \end{aligned} \tag{3.18}$$

The slow delayed rectifier current I_{Ks} is gated by g_{xs} which is defined through

$$\begin{aligned} \dot{g}_{xs} &= [g_{xs}^{\infty} - g_{xs}]/\tau_{xs} \qquad \text{with} \\ g_{xs}^{\infty} &= \frac{1}{[1+e^{(-5-\Phi)/14}]}, \\ \tau_{xs} &= \frac{1100}{[1+e^{(-10-\Phi)/6}]^{1/2}[1+e^{(\Phi-60)/20}]}. \end{aligned} \tag{3.19}$$

I_{t0} is responsible for the transition between the plateau and depolarization phases. It causes an early limited repolarization. The evolution, time constant and steady state value of the gate, g_r, of this current are given as

$$\begin{aligned} \dot{g}_r &= [g_r^{\infty} - g_r]/\tau_r \qquad \text{with} \\ g_r^{\infty} &= \frac{1}{[1+e^{(20-\Phi)/6}]}, \\ \tau_r &= 9.5e^{-(\Phi+40)^2/1800} + 0.8 \end{aligned} \tag{3.20}$$

and the inactivation gate of this current, g_s is defined as

$$\dot{g}_s = [g_s^{\infty} - g_s]/\tau_s \tag{3.21}$$

where the gating parameters g_s^{∞} and τ_s are defined for the epicardium as

$$g_s^{\infty} = [1+e^{(\Phi+20)/5}] \qquad \text{and} \quad \tau_s = 85e^{-(\Phi+45)^2/320} + 5[1+e^{(\Phi-20)/5}] + 3,$$

and for the endocardium as

$$g_s^{\infty} = [1+e^{(\Phi+28)/5}] \qquad \text{and} \quad \tau_s = 1000e^{-(\Phi+67)^2/1000} + 8.$$

3.1.3 Calcium Concentration and Related Variables

The calcium enters into the cell during the plateau phase. The ecolution of the calcium is critical, because it initiates the mechanical behavior of the cell. The influx of the calcium ions are slow compared to the influx of sodium ions.

Therefore, the calcium ions causing the current I_{CaL} are balanced out by the potassium related currents. Therefore, the potential of the cell remains constant during the entrance of the calcium ions. The time-dependent behavior of the calcium ions are explained with the following differential equation:

$$\dot{c}_{Ca} = \gamma_{Ca}\left[-\frac{C}{2VF}[I_{CaL} + I_{bCa} + I_{pCa} - 2I_{NaCa}] + I_{leak} - I_{up} + I_{rel}\right]. \quad (3.22)$$

There are two sets of currents changing the calcium concentration. The first set depends on the concentration of the cytoplasm, while the second set depends on the sarcoplastic reticulum. The currents I_{CaL}, I_{bCa}, I_{pCa} and I_{NaCa} are related to the calcium concentration of the cytoplasm. Other currents I_{leak}, I_{up} and I_{rel} depend on the calcium changes of the sarcoplastic reticulum. The calcium dependent currents are provided as follows:

$$\begin{aligned}
I_{CaL} &= \frac{C_{CaL}^{max} g_d g_f g_{fCa}[4\Phi F^2][c_{Ca}e^{2\Phi F/[RT]} - 0.341 c_{Ca0}]}{[e^{2\Phi F/[RT]} - 1][RT]}, \\
I_{bCa} &= C_{bCa}^{max}[\Phi - \Phi_{Ca}], \\
I_{pCa} &= \frac{C_{pCa}^{max} c_{Ca}}{[c_{pCa} + c_{Ca}]}, \\
I_{NaCa} &= \frac{I_{NaCa}^{max}[e^{\gamma\Phi F/RT} c_{Na}^3 c_{Ca0} - e^{(\gamma-1)\Phi F/RT} c_{Na0}^3 c_{Ca} \gamma_{NaCa}]}{[[c_{NaCa}^3 + c_{Na0}^3][c_{CaNa} + c_{Ca0}][1 + k_{NaCa}^{sat} e^{(\gamma-1)\Phi F/RT}]]}, \\
I_{leak} &= l_{leak}^{max}[c_{Ca}^{sr} - c_{Ca}], \\
I_{up} &= \frac{1}{l_{up}^{max}[1 + c_{up}^2/c_{Ca}^2]}, \\
I_{rel} &= l_{rel}^{max} g_d g_f [1 + \frac{\gamma_{rel} c_{Ca}^{sr2}}{[c_{rel}^2 + c_{Ca}^{sr2}]}],
\end{aligned} \quad (3.23)$$

The parameter set for the constants of these equations are provided in Table 3.1. The free calcium concentration and the buffered calcium concentration should be summed in order to obtain the calcium concentration of the intracellular domain. The addition is defined with $c_{ca}^{tot} = c_{Ca} + c_{Ca}^{buf}$ where buffered calcium concentration is $c_{Ca}^{buf} = [c_{Ca} c_{Ca\,buf}^{tot}][c_{Ca} - c_{Ca\,buf}]^{-1}$. And, the calcium concentration is weighed with $\gamma_{Ca} = [1 + [c_{tot} c_{buf}][c_{Ca} + c_{buf}]^{-2}]^{-1}$.

The dominant calcium channel, long-lasting L-type calcium channel is controlled by the gate g_d. The transient, steady-state value and the time constant of this gate are defined as

$$\begin{aligned} \dot{g}_d &= [g_d^\infty - g_d]/\tau_d \qquad \text{with} \\ g_d^\infty &= \frac{1}{[1+e^{(-5-\Phi)/7.5}]}, \\ \tau_d &= [\frac{1.4}{[1+e^{(-35-\Phi)/13}]}+0.25][1.4[1+e^{(\Phi+5)/5}]]+[1+e^{(50-\Phi)/20}]. \end{aligned} \tag{3.24}$$

First inactivation gate is g_f. Its evolution, steady state value and time constant are defined through,

$$\begin{aligned} \dot{g}_f &= [g_f^\infty - g_f]/\tau_f \qquad \text{with} \\ g_f^\infty &= \frac{1}{[1+e^{(\Phi+20)/7}]}, \\ \tau_f &= 1125e^{-(\Phi+27)^2/240}+\frac{165}{[1+e^{(25-\Phi)/10}]}+80. \end{aligned} \tag{3.25}$$

Second inactivation gate is g_{fCa}. It depends on the calcium concentration. The

evolution, steady state value and the time constant are defined through

$$\dot{g}_{fCa} = [g^{\infty}_{fCa} - g_{fCa}]/\tau_{fCa} \qquad \text{with}$$

$$\begin{aligned} g^{\infty}_{fCa} &= \frac{0.685}{[[1 + (c_{ca}/0.000325)^8]} + \frac{0.1}{[1 + e^{(c_{ca}-0.0005)/0.0001}]} \\ &+ \frac{0.2}{[1 + e^{(c_{ca}-0.00075)/0.0008}]} + 0.23, \end{aligned} \tag{3.26}$$

$$\tau_{fCa} = \begin{cases} \infty, & \text{if } g^{\infty}_{fCa} > g_{fCa}, \Phi \geq -60, \\ 2\,\text{ms}, & \text{otherwise.} \end{cases}$$

Last, the calcium-induced calcium release current I_{rel} is characterized through the activation gate g_d defined above. Also, it depends on the calcium-dependent inactivation gate g_g. The evolution, steady state value and time constant of this gate is defined by

$$\dot{g}_g = [g^{\infty}_g - g_g]/\tau_g \qquad \text{with}$$

$$g^{\infty}_g = \begin{cases} \dfrac{1}{[1 + c^6_{ca}/0.00035^6]}, & \text{if } c_{ca} \leq 0.00035, \\ \dfrac{1}{[1 + c^{16}_{ca}/0.00035^{16}]}, & \text{otherwise.} \end{cases} \tag{3.27}$$

$$\tau_g = \begin{cases} \infty, & \text{if } g^{\infty}_g > g_g, \Phi \geq -60\,, \\ 2\,\text{ms}, & \text{otherwise.} \end{cases}$$

3.1.4 Calcium Concentration of the Sarcoplastic Reticulum and Related Variables

The calcium concentration of the sarcoplastic reticulum is only the calcium concentration of the intracellular medium but scaled with the volume ratios of the intracellular space and the sarcoplastic reticulum space. The volume of the intracellular domain is denoted by V, while the volume of the sarcoplastic reticulum is denoted by V^{sr}. With this information, the concentration of the calcium in the sarcoplastic reticulum is expressed with the following ODE:

$$\dot{c}^{sr}_{Ca} = \gamma^{sr}_{Ca} \frac{V}{V^{sr}} [-I_{leak} + I_{up} - I_{rel}]. \tag{3.28}$$

The leakage curren, uptake current and release current are defined as follows,

$$\begin{aligned} I_{leak} &= l^{max}_{leak}[c^{sr}_{Ca} - c_{Ca}], \\ I_{up} &= \frac{l^{max}_{up}}{[1 + c^2_{up}/c^2_{Ca}]}, \\ I_{rel} &= l^{max}_{rel} g_d g_g [1 + \frac{\gamma_{rel} c^{sr2}_{Ca}}{[c^2_{rel} + c^{sr2}_{Ca}]}]. \end{aligned} \tag{3.29}$$

The free calcium concentration and the buffered calcium concentration should be summed in order to obtain the calcium concentration of the intracellular domain. The addition is defined with $c^{sr\,tot}_{ca} = c^{sr}_{Ca} + c^{sr\,buf}_{Ca}$ where buffered calcium concentration is $c^{sr\,buf}_{Ca} = [c^{sr}_{Ca} c^{sr}_{tot}][c^{sr}_{Ca} - c^{sr}_{buf}]^{-1}$. And, the calcium concentration is weighed with $\gamma^{sr}_{Ca} = [1 + [c^{sr}_{tot} c^{sr}_{buf}][c^{sr}_{Ca} + c^{sr}_{buf}]^{-2}]^{-1}$.

3.2 Local Discretization of the Model Problem

The chemical problem involves 13 gating variables, 10 of which depend only on the current transmembrane potential, whereas 3 of them depend on both the current transmembrane potential and the ion concentrations, as stated earlier. Furthermore, there are 4 ion concentrations to be solved. These total of 17 internal variables are stored at the integration points. The initial values of these

variables at t=0 are the resting state values. For the temporal discretization, the finite difference scheme is used. The update equations are given in the following form,

$$\begin{aligned} \dot{g}^{I}_{gate} &= [g^{I}_{gate} - g^{In}_{gate}]/\Delta t, \\ \dot{g}^{II}_{gate} &= [g^{II}_{gate} - g^{IIn}_{gate}]/\Delta t, \\ \dot{c}_{ion} &= [c_{ion} - c^{n}_{ion}]/\Delta t \end{aligned} \tag{3.30}$$

where the implicit Euler scheme is used to update the values of the gating variables g^{I}_{gate} and g^{II}_{gate}, at current time step t.

$$\begin{aligned} g^{I}_{gate} &= g^{In}_{gate} + \frac{1}{\tau^{I}_{gate}(\Phi)}[g^{\infty I}_{gate}(\Phi) - g^{I}_{gate}]\Delta t, \\ g^{II}_{gate} &= g^{IIn}_{gate} + \frac{1}{\tau^{II}_{gate}(\Phi)}[g^{\infty II}_{gate}(\Phi, c_{ion}) - g^{II}_{gate}]\Delta t. \end{aligned} \tag{3.31}$$

The equations of the first subset depend only on the current transmembrane potential. Hence, the solutions of these variables remain constant during the local iteration. The second subset, on the other hand, is updated iteratively. The set of the residuals on the local point is defined through,

$$\begin{aligned} R^{c}_{K} &= c_K - c^{n}_{K} + \frac{C}{VF}[I_{K1} + I_{Kr} + I_{Ks} - 2I_{NaK} \\ &\quad + I_{pK} + I_{t0} + I_{stim}]\Delta t \doteq 0, \\ R^{c}_{Na} &= c_{Na} - c^{n}_{Na} + \frac{C}{VF}[I_{Na} + I_{bNa} + 3I_{NaK} + 3I_{NaCa}]\Delta t \doteq 0, \\ R^{c}_{Ca} &= c_{Ca} - c^{n}_{Ca} + \Big[\frac{C}{2VF}[I_{CaL} + I_{bCa} + I_{pCa} - 2I_{NaCa}] \\ &\quad - I_{leak} + I_{up} - I_{rel}\Big]\gamma_{Ca}\Delta t \doteq 0, \\ R^{src}_{Ca} &= c^{sr}_{Ca} - c^{srn}_{Ca} + \frac{V}{V^{sr}}[I_{leak} - I_{up} + I_{rel}]\gamma^{sr}_{Ca}\Delta t \doteq 0. \end{aligned} \tag{3.32}$$

Also, the linearization of the residual vectors with respect to the ion concentra-

tions are defined through

$$K^c_{ion\,ion} = \partial_{c_{ion}} R^c_{ion} = \begin{bmatrix} \partial_{c_K} R^c_K & \partial_{c_{Na}} R^c_K & 0 & 0 \\ 0 & \partial_{c_{Na}} R^c_{Na} & \partial_{c_{Ca}} R^c_{Na} & 0 \\ 0 & \partial_{c_{Na}} R^c_{Ca} & \partial_{c_{Ca}} R^c_{Ca} & \partial_{c^{sr}_{Ca}} R^c_{Ca} \\ 0 & 0 & \partial_{c_{Ca}} R^{src}_{Ca} & \partial_{c^{sr}_{Ca}} R^{src}_{Ca} \end{bmatrix} \tag{3.33}$$

Then, the set of ion concentrations is updated through $c_{ion} \leftarrow c_{ion}$ - $\left[K^c_{ion\,ion}\right]^{-1} R^c_{ion}$ and the second subset of gating variables through $g^{II}_{gate} \leftarrow g^{II}_{gate} + g^{gII}_{gate}(\Phi, g_{gate}, c_{ion})\Delta t$. Once converged for a specified tolerance and the residual norm, the updated set of the ionic currents are summed to obtain the electrical source term, f^Φ in (3.8).

$$\begin{aligned} f^\Phi = -[&I_{Na} + I_{bNa} + I_{NaK} + I_{NaCa} + I_{K1} + \\ &I_{Kr} + I_{Ks} + I_{pK} + I_{t0} + I_{CaL} + I_{bCa} + I_{pCa}]. \end{aligned} \tag{3.34}$$

Furthermore, the linearized terms of the source term are summed for the linearization of the global residual vectors. The linearized terms are given in the form,

$$\begin{aligned} \partial_\Phi f^\Phi = -[&\partial_\Phi I_{Na} + \partial_\Phi I_{bNa} + \partial_\Phi I_{NaK} + \partial_\Phi I_{NaCa} + \partial_\Phi I_{K1} + \partial_\Phi I_{Kr} + \\ &\partial_\Phi I_{Ks} + \partial_\Phi I_{pK} + \partial_\Phi I_{t0} + \partial_\Phi I_{CaL} + \partial_\Phi I_{bCa} + \partial_\Phi I_{pCa}]. \end{aligned} \tag{3.35}$$

For the derivation of the linearized terms, please see [34] In the current chapter, the electrical source term f^Φ and its linearization $\partial_\Phi f^\Phi$ are provided to complete the mathematical description of the problem. In Chapter 4, the spatio-temporal discretization of the global problem is introduced.

CHAPTER 4

DISCRETIZATIONS AND NUMERICAL IMPLEMENTATIONS

In Chapter 4, two numerical modifications that decrease the solution time of the bimaterial problem at hand are introduced. These modifications are implemented into the initial boundary value problem that is described in Chapter 2 and Chapter 3. The first improvement is the condensation of the solution matrix and the solution of the reduced matrix. The second improvement is the coupling of the boundary element and finite element methods on the heart surface. In Section 4.1, the finite element discretization of the integrated cardiac electrophysiology problem is presented. In Section 4.2, the details of the condensation procedure are provided. Lastly, the boundary element method and its coupling with the finite element method are explained in Section 4.3.

4.1 Finite Element Discretization of the Bidomain Model

In this part, the spatio-temporal discretization of the coupled bidomain problem of the heart domain $\mathcal{B}^H$ and the linear torso problem of the torso domain $\mathcal{B}^T$ are introduced. For the spatial discretization of the two field variables, namely the transmembrane potential Φ and the extracellular potential Φ_e, the finite element scheme is applied. The residuals are linearized consistently and solved with the incrementally iterative Newton scheme for the nodal unknowns. The electrical source term f^{Φ} and its derivative $\mathrm{d}_{\Phi} f^{\Phi}$ are treated as the local problem. The variables of this problem are stored and updated at the integration point level. The update scheme of these variables is explained in Chapter 3.

For the finite element discretization of the global problem, C^0 - continuous

isoparametric shape functions are selected. The weak form of the governing equations of the bidomain model and the linear conductor are obtained through the following residual expressions:

$$\begin{aligned}
\mathrm{R}^{\Phi} = &\quad \dot{\Phi} - \operatorname{div}(\bar{\boldsymbol{D}}_{\mathrm{i}} \cdot \nabla\Phi) - \operatorname{div}(\bar{\boldsymbol{D}}_{\mathrm{i}} \cdot \nabla\Phi_{\mathrm{e}}) - f^{\Phi} \doteq 0 && \text{in } \mathcal{B}^H, \\
\mathrm{R}^{\Phi_{\mathrm{e}}} = &\quad - \operatorname{div}(\bar{\boldsymbol{D}}_{\mathrm{i}} \cdot \nabla\Phi) - \operatorname{div}(\bar{\boldsymbol{D}} \cdot \nabla\Phi_{\mathrm{e}}) \doteq 0 && \text{in } \mathcal{B}^H, \\
\mathrm{R}^{\Phi_{\mathrm{e}}} = &\quad - \operatorname{div}(\boldsymbol{D}_{\mathrm{T}} \cdot \nabla\Phi_{\mathrm{e}}) \doteq 0 && \text{in } \mathcal{B}^T.
\end{aligned} \tag{4.1}$$

The first two expressions are integrated over the heart domain $\mathcal{B}^H$, and the third statement is integrated over the torso domain $\mathcal{B}^T$. These domains are illustrated in Figure 2.1. Further, they are tested by square-integrable scalar-valued test functions $\delta\Phi$ and $\delta\Phi_{\mathrm{e}}$, respectively. Employing the integration by parts and the Gauss's theorem, we obtain the following weak forms where the Galerkin functionals are separated into the internal and external parts

$$\begin{aligned}
\mathrm{G}^{\Phi}(\delta\Phi, \Phi, \Phi_{\mathrm{e}}) &= \mathrm{G}^{\Phi}_{\mathrm{int}}(\delta\Phi, \Phi, \Phi_{\mathrm{e}}) - \mathrm{G}^{\Phi}_{\mathrm{ext}}(\delta\Phi, \Phi) = 0 && \text{in } \mathcal{B}^H \\
\mathrm{G}^{\Phi_{\mathrm{e}}}(\delta\Phi_{\mathrm{e}}, \Phi, \Phi_{\mathrm{e}}) &= \mathrm{G}^{\Phi_{\mathrm{e}}}_{\mathrm{int}}(\delta\Phi_{\mathrm{e}}, \Phi, \Phi_{\mathrm{e}}) - \mathrm{G}^{\Phi_{\mathrm{e}}}_{\mathrm{ext}}(\delta\Phi_{\mathrm{e}}) = 0 && \text{in } \mathcal{B}^H, \\
\mathrm{G}^{\Phi_{\mathrm{e}}}(\delta\Phi_{\mathrm{e}}, \Phi_{\mathrm{e}}) &= \mathrm{G}^{\Phi_{\mathrm{e}}}_{\mathrm{int}}(\delta\Phi_{\mathrm{e}}, \Phi_{\mathrm{e}}) - \mathrm{G}^{\Phi_{\mathrm{e}}}_{\mathrm{ext}}(\delta\Phi_{\mathrm{e}}) = 0 && \text{in } \mathcal{B}^T.
\end{aligned} \tag{4.2}$$

The specific forms of the internal and external parts of the Galerkin functionals for the transmembrane potential of the heart domain are defined as

$$\begin{aligned}
\mathrm{G}^{\Phi}_{\mathrm{int}}(\delta\Phi, \Phi, \Phi_{\mathrm{e}}) &= \int_{\mathcal{B}^H} (\delta\Phi\dot{\Phi} + \nabla(\delta\Phi) \cdot \bar{\boldsymbol{D}}_{\mathrm{i}} \cdot (\nabla\Phi + \nabla\Phi_{\mathrm{e}}))\, \mathrm{dV}\,, \\
\mathrm{G}^{\Phi}_{\mathrm{ext}}(\delta\Phi) &= \int_{\mathcal{B}^H} \delta\Phi f^{\Phi}\, \mathrm{dV} + \int_{\partial\mathcal{B}^H_q} \delta\Phi\bar{q}_{\mathrm{i}}\, \mathrm{dA},
\end{aligned} \tag{4.3}$$

For this equation set, the Neumann boundary condition is described with the term $\bar{q}_{\mathrm{i}} = \bar{\boldsymbol{D}}_{\mathrm{i}} \cdot (\nabla\Phi + \nabla\Phi_{\mathrm{e}}) \cdot \boldsymbol{n}_{\boldsymbol{H}}$ on $\partial\mathcal{B}^H_q$. Similar separation procedure is applied

to the second Galerkin functional of the heart domain leading to the equations,

$$\begin{aligned} \mathrm{G}_{\mathrm{int}}^{\Phi_\mathrm{e}}(\delta\Phi_\mathrm{e}, \Phi, \Phi_\mathrm{e}) &= \int\limits_{\mathcal{B}^H} \nabla(\delta\Phi_\mathrm{e}) \cdot (\bar{\boldsymbol{D}} \cdot \nabla\Phi_\mathrm{e} + \bar{\boldsymbol{D}}_\mathrm{i} \cdot \nabla\Phi)\, \mathrm{dV}\,, \\ \mathrm{G}_{\mathrm{ext}}^{\Phi_\mathrm{e}}(\delta\Phi_\mathrm{e}) &= \int\limits_{\partial\mathcal{B}_q^H} \delta\Phi_\mathrm{e}\bar{q}_\mathrm{t}\, \mathrm{dA}, \end{aligned} \tag{4.4}$$

for the extracellular potential. The term $\bar{q}_\mathrm{t} = (\bar{\boldsymbol{D}}_\mathrm{e} \cdot \nabla\Phi_\mathrm{e} + \bar{\boldsymbol{D}}_\mathrm{i} \cdot \nabla\Phi_\mathrm{i}) \cdot \boldsymbol{n_H}$ is the total current flux applied on the boundary $\partial\mathcal{B}_q^H$. The specific forms of the Galerkin functionals for the torso domain are given as

$$\begin{aligned} \mathrm{G}_{\mathrm{int}}^{\Phi_\mathrm{e}}(\delta\Phi_\mathrm{e}, \Phi_\mathrm{e}) &= \int\limits_{\mathcal{B}^T} \nabla(\delta\Phi_\mathrm{e}) \cdot (\boldsymbol{D}_\mathrm{T} \cdot \nabla\Phi_\mathrm{e})\, \mathrm{dV}\,, \\ \mathrm{G}_{\mathrm{ext}}^{\Phi_\mathrm{e}}(\delta\Phi_\mathrm{e}) &= \int\limits_{\partial\mathcal{B}_q^T} \delta\Phi_\mathrm{e} i_{app}\, \mathrm{dA} + \int\limits_{\Gamma} \delta\Phi_\mathrm{e}\bar{q}_\mathrm{T}\, \mathrm{dA} \end{aligned} \tag{4.5}$$

for the extracellular potential. The external flux applied to the torso surface $\partial\mathcal{B}_q^T$ is denoted by i_{app}. Furthermore, for temporal discretization, the time increment t is defined as $\Delta t = t\text{-}t_\mathrm{n}{>}0$. Here, t denotes the current time and t_n denotes the previous time. The time field is discretized into $\mathrm{n_{stp}}$ subintervals. For each of these subintervals, the classical implicit Euler time integration scheme is applied. The evolution term of the transmembrane potential can be approximated using the following finite difference scheme:

$$\dot{\Phi} \approx \frac{\Phi - \Phi_\mathrm{n}}{\Delta\mathrm{t}} \qquad \text{where} \qquad \Phi_\mathrm{n} := \Phi(\boldsymbol{X}, \mathrm{t_n}). \tag{4.6}$$

The physical domain of the heart $\mathcal{B}^H$ is discretized into $\mathrm{nel_H}$ elements, $\mathcal{B}_\mathrm{el}^H$. These finite elements satisfy the condition $\mathcal{B}^H \approx \bigcup_{\mathrm{el}=1}^{\mathrm{nel_H}} \mathcal{B}_\mathrm{el}^H$. Furthermore, the torso domain is discretized into $\mathrm{nel_T}$ elements that satisfy the condition $\mathcal{B}^T \approx \bigcup_{\mathrm{el}=1}^{\mathrm{nel_T}} \mathcal{B}_\mathrm{el}^T$. Referring to the isoparametric approach, the test functions and the shape functions are the same interpolation functions on the element level.

Eventually, the field variables within an element domain are approximated by

$$\begin{aligned} \delta\Phi &= \sum_{a=1}^{n_{en}} N^a \delta\Phi^h_a; \qquad \delta\Phi_e = \sum_{a=1}^{n_{en}} N^a \delta\Phi^h_{e_a}, \\ \Phi &= \sum_{a=1}^{n_{en}} N^a \Phi^h_a; \qquad \Phi_e = \sum_{a=1}^{n_{en}} N^a \Phi^h_{e_a}, \end{aligned} \tag{4.7}$$

where n_{en} and $N^a(\boldsymbol{X})$ refer to the number of nodes of each element and shape functions, respectively. Further, Φ^h_a and $\Phi^h_{e_a}$ denote the nodal values of the variables. Moreover, the spatial potential gradients are derived to be

$$\begin{aligned} \nabla(\delta\Phi) &= \sum_{a=1}^{n_{en}} \delta\Phi^h_a \otimes \nabla N^a, \\ \nabla(\delta\Phi_e) &= \sum_{a=1}^{n_{en}} \delta\Phi^h_{e_a} \otimes \nabla N^a. \end{aligned} \tag{4.8}$$

Global nodes of the bimaterial problem are separated into three groups for a better representation of the discrete residuals. The heart domain contains n_H nodes and the torso domain contains n_T nodes excluding the interface. Furthermore, there are n_Γ nodes on the interface between the two domains. The discrete form of the residuals of the heart nodes are obtained using (4.3), (4.7), and (4.8).

$$\begin{aligned} R^{\Phi}_{I_H} &= \mathop{\mathsf{A}}_{el=1}^{nel_H} \Big\{ \int_{\mathcal{B}^H_{el}} \left[N^a \tfrac{\Phi-\Phi^n}{\Delta t} + \nabla N^a (\bar{\boldsymbol{D}}_i \cdot \nabla\Phi + \bar{\boldsymbol{D}}_i \cdot \nabla\Phi_e) \right] dV \\ &\qquad - \int_{\mathcal{B}^H_{el}} N^a f^\Phi \, dV - \int_{\partial\mathcal{B}^H_{el}} N^a \bar{q}_i \, dA \Big\}, \\ R^{\Phi_e}_{I_H} &= \mathop{\mathsf{A}}_{el=1}^{nel_H} \Big\{ \int_{\mathcal{B}^H_{el}} [\nabla N^a (\bar{\boldsymbol{D}} \cdot \nabla\Phi_e + \bar{\boldsymbol{D}}_i \cdot \nabla\Phi)] \, dV - \int_{\partial\mathcal{B}^H_{el}} N^a \bar{q}_t \, dA \Big\}. \end{aligned} \tag{4.9}$$

Here, I_H are the global numbers of the H=1,..,n_H heart nodes, nel_H is the number of the heart elements and a=1,..,n_{en} are the local element nodes. In this representation, the residual contribution of each heart element to the corresponding global nodes is provided. The discrete form of the residuals of the torso nodes

are provided using the equations (4.5), (4.7) and (4.8).

$$\mathrm{R}^{\Phi_\mathrm{e}}_{\mathrm{I_T}} = \mathop{\mathsf{A}}_{\mathrm{el}=1}^{\mathrm{nel_T}} \Big\{ \int\limits_{\mathcal{B}^{\mathrm{T}}_{\mathrm{el}}} \nabla \mathrm{N}^{\mathrm{a}} (\boldsymbol{D}_{\mathrm{T}} \cdot \nabla \Phi_{\mathrm{e}}) \, \mathrm{dV} - \int\limits_{\partial \mathcal{B}^{\mathrm{T}}_{\mathrm{el}}} \mathrm{N}^{\mathrm{a}} \bar{q}_{\mathrm{T}} \, \mathrm{dA} \Big\}. \tag{4.10}$$

Here, $\mathrm{I_T}$ are the global numbers of the $\mathrm{T}=1,..,\mathrm{n_T}$ torso nodes and $\mathrm{nel_T}$ is the number of the torso elements. The residual contribution of each torso element to the corresponding global nodes is provided. Furthermore, the transmembrane potential residuals of the interface nodes are given in the following form:

$$\begin{aligned} \mathrm{R}^{\Phi}_{\mathrm{I}_\Gamma} = \mathop{\mathsf{A}}_{\mathrm{el}=1}^{\mathrm{nel_H}} \Big\{ & \int\limits_{\mathcal{B}^{\mathrm{H}}_{\mathrm{el}}} \left[\mathrm{N}^{\mathrm{a}} \tfrac{\Phi - \Phi^{\mathrm{n}}}{\Delta \mathrm{t}} + \nabla \mathrm{N}^{\mathrm{a}} (\bar{\boldsymbol{D}}_{\mathrm{i}} \cdot \nabla \Phi + \bar{\boldsymbol{D}}_{\mathrm{i}} \cdot \nabla \Phi_{\mathrm{e}}) \right] \mathrm{dV} \\ & - \int\limits_{\mathcal{B}^{\mathrm{H}}_{\mathrm{el}}} \mathrm{N}^{\mathrm{a}} f^{\Phi} \, \mathrm{dV} - \int\limits_{\partial \mathcal{B}^{\mathrm{H}}{}_{\mathrm{el}}} \mathrm{N}^{\mathrm{a}} \bar{q}_{\mathrm{i}} \, \mathrm{dA} \Big\}, \end{aligned} \tag{4.11}$$

In this representation, I_Γ are the global numbers of the $\Gamma=1,..,\mathrm{n}_\Gamma$ interface nodes. The residual contributions of each heart element to the corresponding global nodes are provided. It is important to state that there is no contribution from the torso elements to the transmembrane potential residual on the interface Γ, since there is no transmembrane potential developing in the torso. The extracellular potential residual of the interface nodes gets contribution from both the heart elements and the torso elements. Therefore, the residual term involves two parts. These two parts are obtained to be

$$\begin{aligned} \mathrm{R}^{\Phi_\mathrm{e}}_{\mathrm{I}_\Gamma} = & \mathop{\mathsf{A}}_{\mathrm{el}=1}^{\mathrm{nel_T}} \Big\{ \int\limits_{\mathcal{B}^{\mathrm{T}}_{\mathrm{el}}} \nabla \mathrm{N}^{\mathrm{a}} (\boldsymbol{D}_{\mathrm{T}} \cdot \nabla \Phi_{\mathrm{e}}) \, \mathrm{dV} - \int\limits_{\partial \mathcal{B}^{\mathrm{T}}_{\mathrm{el}}} \mathrm{N}^{\mathrm{a}} \bar{q}_{\mathrm{T}} \, \mathrm{dA} \Big\} \\ & + \mathop{\mathsf{A}}_{\mathrm{el}=1}^{\mathrm{nel_H}} \Big\{ \int\limits_{\mathcal{B}^{\mathrm{H}}_{\mathrm{el}}} [\nabla \mathrm{N}^{\mathrm{a}} (\bar{\boldsymbol{D}} \cdot \nabla \Phi_{\mathrm{e}} + \bar{\boldsymbol{D}}_{\mathrm{i}} \cdot \nabla \Phi)] \, \mathrm{dV} - \int\limits_{\partial \mathcal{B}^{\mathrm{H}}_{\mathrm{el}}} \mathrm{N}^{\mathrm{a}} \bar{q}_{\mathrm{t}} \, \mathrm{dA} \Big\}. \end{aligned} \tag{4.12}$$

In order to apply the incrementally iterative Newton Raphson method, the consistent linearization of the residuals is required. The residual vectors and incre-

ments are given as

$$\hat{\boldsymbol{R}} = \begin{Bmatrix} \boldsymbol{R}_{\mathrm{H}}^{\Phi} \\ \boldsymbol{R}_{\mathrm{H}}^{\Phi_{\mathrm{e}}} \\ \boldsymbol{R}_{\Gamma}^{\Phi} \\ \boldsymbol{R}_{\Gamma}^{\Phi_{\mathrm{e}}} \\ \boldsymbol{R}_{\mathrm{T}}^{\Phi_{\mathrm{e}}} \end{Bmatrix}; \quad \Delta\hat{\boldsymbol{\Phi}} = \begin{Bmatrix} \Delta\boldsymbol{\Phi}^{\mathrm{H}} \\ \Delta\boldsymbol{\Phi}_{\mathrm{e}}^{\mathrm{H}} \\ \Delta\boldsymbol{\Phi}^{\Gamma} \\ \Delta\boldsymbol{\Phi}_{\mathrm{e}}^{\Gamma} \\ \Delta\boldsymbol{\Phi}_{\mathrm{e}}^{\mathrm{T}} \end{Bmatrix}. \tag{4.13}$$

$$\mathrm{Lin}\hat{\boldsymbol{R}} = \hat{\boldsymbol{R}} + \frac{\partial\hat{\boldsymbol{R}}}{\partial\hat{\boldsymbol{\Phi}}}\Delta\hat{\boldsymbol{\Phi}} \tag{4.14}$$

$$\hat{\boldsymbol{K}} = \frac{\partial\hat{\boldsymbol{R}}}{\partial\hat{\boldsymbol{\Phi}}} = \mathop{\mathsf{A}}_{\mathrm{el}=1}^{\mathrm{nel_T}+\mathrm{nel_H}} \boldsymbol{K}^{\mathrm{el}} \tag{4.15}$$

Then, the linearized terms are obtained to be

$$\begin{aligned}
\mathrm{K}_{HH}^{\Phi\Phi} = \mathrm{K}_{H\Gamma}^{\Phi\Phi} = \mathrm{K}_{\Gamma H}^{\Phi\Phi} = \mathrm{K}_{\Gamma\Gamma}^{\Phi\Phi} &= \mathsf{A}\int_{\mathcal{B}_{\mathrm{el}}^{\mathrm{H}}} \nabla\mathrm{N}^{\mathrm{a}}\bar{\boldsymbol{D}}_{\mathrm{i}}\nabla\mathrm{N}^{\mathrm{b}}\mathrm{dV} + \mathsf{A}\int_{\mathcal{B}_{\mathrm{el}}^{\mathrm{H}}} \mathrm{N}^{\mathrm{a}}\left(\tfrac{1}{\Delta t} - \mathrm{d}_{\Phi}f^{\Phi}\right)\mathrm{N}^{\mathrm{b}}\mathrm{dV}, \\
\mathrm{K}_{HH}^{\Phi\Phi_e} = \mathrm{K}_{\Gamma H}^{\Phi\Phi_e} = \mathrm{K}_{H\Gamma}^{\Phi_e\Phi} = \mathrm{K}_{\Gamma\Gamma}^{\Phi\Phi_e} &= \mathsf{A}\int_{\mathcal{B}_{\mathrm{el}}^{\mathrm{H}}} \nabla\mathrm{N}^{\mathrm{a}}\bar{\boldsymbol{D}}_{\mathrm{i}}\nabla\mathrm{N}^{\mathrm{b}}\mathrm{dV}, \\
\mathrm{K}_{HH}^{\Phi_e\Phi} = \mathrm{K}_{\Gamma H}^{\Phi_e\Phi} = \mathrm{K}_{H\Gamma}^{\Phi\Phi_e} = \mathrm{K}_{\Gamma\Gamma}^{\Phi\Phi_e} &= \mathsf{A}\int_{\mathcal{B}^{\mathrm{H}}} \nabla\mathrm{N}^{\mathrm{a}}\bar{\boldsymbol{D}}_{\mathrm{i}}\nabla\mathrm{N}^{\mathrm{b}}\mathrm{dV}, \\
\mathrm{K}_{HH}^{\Phi_e\Phi_e} = \mathrm{K}_{\Gamma H}^{\Phi_e\Phi_e} = \mathrm{K}_{H\Gamma}^{\Phi_e\Phi_e} &= \mathsf{A}\int_{\mathcal{B}_{\mathrm{el}}^{\mathrm{H}}} \nabla\mathrm{N}^{\mathrm{a}}\bar{\boldsymbol{D}}\nabla\mathrm{N}^{\mathrm{b}}\mathrm{dV}, \\
\mathrm{K}_{T\Gamma}^{\Phi_e\Phi_e} = \mathrm{K}_{T\Gamma}^{\Phi_e\Phi_e} = \mathrm{K}_{\Gamma T}^{\Phi_e\Phi_e} &= \mathsf{A}\int_{\mathcal{B}_{\mathrm{el}}^{\mathrm{T}}} \nabla\mathrm{N}^{\mathrm{a}}\bar{\boldsymbol{D}}_{\mathrm{T}}\nabla\mathrm{N}^{\mathrm{b}}\mathrm{dV}, \\
\mathrm{K}_{\Gamma\Gamma}^{\Phi_e\Phi_e} &= \mathsf{A}\int_{\mathcal{B}_{\mathrm{el}}^{\mathrm{T}}} \nabla\mathrm{N}^{\mathrm{a}}\boldsymbol{D}_{\mathrm{T}}\nabla\mathrm{N}^{\mathrm{b}}\mathrm{dV} + \mathsf{A}\int_{\mathcal{B}_{\mathrm{el}}^{\mathrm{H}}} \nabla\mathrm{N}^{\mathrm{a}}\bar{\boldsymbol{D}}\nabla\mathrm{N}^{\mathrm{b}}\mathrm{dV}.
\end{aligned} \tag{4.16}$$

Then, the elemental stiffness terms are assembled into the following compact

form of the global solution matrix:

$$
-\begin{bmatrix}
\boldsymbol{K}_{\mathrm{HH}}^{\Phi\Phi} & \boldsymbol{K}_{\mathrm{HH}}^{\Phi\Phi_{\mathrm{e}}} & \boldsymbol{K}_{\mathrm{H\Gamma}}^{\Phi\Phi} & \boldsymbol{K}_{\mathrm{H\Gamma}}^{\Phi\Phi_{\mathrm{e}}} & 0 \\
\boldsymbol{K}_{\mathrm{HH}}^{\Phi_{\mathrm{e}}\Phi} & \boldsymbol{K}_{\mathrm{HH}}^{\Phi_{\mathrm{e}}\Phi_{\mathrm{e}}} & \boldsymbol{K}_{\mathrm{H\Gamma}}^{\Phi_{\mathrm{e}}\Phi} & \boldsymbol{K}_{\mathrm{H\Gamma}}^{\Phi_{\mathrm{e}}\Phi_{\mathrm{e}}} & 0 \\
\boldsymbol{K}_{\Gamma\mathrm{H}}^{\Phi\Phi} & \boldsymbol{K}_{\Gamma\mathrm{H}}^{\Phi\Phi_{\mathrm{e}}} & \boldsymbol{K}_{\Gamma\Gamma}^{\Phi\Phi} & \boldsymbol{K}_{\Gamma\Gamma}^{\Phi\Phi_{\mathrm{e}}} & 0 \\
\boldsymbol{K}_{\Gamma\mathrm{H}}^{\Phi_{\mathrm{e}}\Phi} & \boldsymbol{K}_{\Gamma\mathrm{H}}^{\Phi_{\mathrm{e}}\Phi_{\mathrm{e}}} & \boldsymbol{K}_{\Gamma\Gamma}^{\Phi_{\mathrm{e}}\Phi} & \boldsymbol{K}_{\Gamma\Gamma}^{\Phi_{\mathrm{e}}\Phi_{\mathrm{e}}} & \boldsymbol{K}_{\Gamma\mathrm{T}}^{\Phi_{\mathrm{e}}\Phi_{\mathrm{e}}} \\
0 & 0 & 0 & \boldsymbol{K}_{\mathrm{T}\Gamma}^{\Phi_{\mathrm{e}}\Phi_{\mathrm{e}}} & \boldsymbol{K}_{\mathrm{TT}}^{\Phi_{\mathrm{e}}\Phi_{\mathrm{e}}}
\end{bmatrix}
\begin{bmatrix}
\Delta\boldsymbol{\Phi}^{\mathrm{H}} \\
\Delta\boldsymbol{\Phi}_{\mathrm{e}}^{\mathrm{H}} \\
\Delta\boldsymbol{\Phi}^{\Gamma} \\
\Delta\boldsymbol{\Phi}_{\mathrm{e}}^{\Gamma} \\
\Delta\boldsymbol{\Phi}_{\mathrm{e}}^{\mathrm{T}}
\end{bmatrix}
=
\begin{bmatrix}
\boldsymbol{R}_{\mathrm{H}}^{\Phi} \\
\boldsymbol{R}_{\mathrm{H}}^{\Phi_{\mathrm{e}}} \\
\boldsymbol{R}_{\Gamma}^{\Phi} \\
\boldsymbol{R}_{\Gamma}^{\Phi_{\mathrm{e}}} \\
\boldsymbol{R}_{\mathrm{T}}^{\Phi_{\mathrm{e}}}
\end{bmatrix}
\tag{4.17}
$$

It is worth noting that the electrical source term f^{Φ} and its consistent linearization $d_{\Phi} f^{\Phi}$ are treated locally. The solution and update procedure of the local problem are already explained in Chapter 3.

The iterative update of the global unknown vector is conducted through the following equations:

$$
\begin{aligned}
\hat{\boldsymbol{\Phi}} &\leftarrow \bar{\boldsymbol{\Phi}} + \Delta\boldsymbol{\Phi}, \\
\Delta\boldsymbol{\Phi} &= -\bar{\boldsymbol{K}}^{-1} \cdot \bar{\boldsymbol{R}}
\end{aligned}
\tag{4.18}
$$

which is applied until the solution converges for a specified residual norm and the tolerance. For a better representation of the solution of the cardiac electrophysiology problem, the algorithmic box is provided in Figure 4.1.

4.2 Condensation of the Solution Matrix

Owing to the linear and time-independent nature of the torso, the corresponding stiffness terms computed with the finite element method are constant. Therefore, the total nodal degrees of freedom of the model can be reduced by manipulating the system of linear equations. The fourth and fifth set of equations of the solution system in (4.17) can be written as

$$
\begin{aligned}
\boldsymbol{R}_{\Gamma}^{\Phi_{\mathrm{e}}} = \;& \boldsymbol{K}_{\Gamma\mathrm{H}}^{\Phi_{\mathrm{e}}\Phi}\Delta\boldsymbol{\Phi}^{\mathrm{H}} + \boldsymbol{K}_{\Gamma\mathrm{H}}^{\Phi_{\mathrm{e}}\Phi_{\mathrm{e}}}\Delta\boldsymbol{\Phi}_{\mathrm{e}}^{\mathrm{H}} + \boldsymbol{K}_{\Gamma\Gamma}^{\Phi_{\mathrm{e}}\Phi}\Delta\boldsymbol{\Phi}^{\Gamma} + \boldsymbol{K}_{\Gamma\Gamma}^{\Phi_{\mathrm{e}}\Phi_{\mathrm{e}}}\Delta\boldsymbol{\Phi}_{\mathrm{e}}^{\Gamma} + \\
& \boldsymbol{K}_{\Gamma\mathrm{T}}^{\Phi_{\mathrm{e}}\Phi_{\mathrm{e}}}\Delta\boldsymbol{\Phi}_{\mathrm{e}}^{\mathrm{T}}, \\
\boldsymbol{R}_{\mathrm{T}}^{\Phi_{\mathrm{e}}} = \;& \boldsymbol{K}_{\mathrm{T}\Gamma}^{\Phi_{\mathrm{e}}\Phi_{\mathrm{e}}}\Delta\boldsymbol{\Phi}_{\mathrm{e}}^{\Gamma} + \boldsymbol{K}_{\mathrm{TT}}^{\Phi_{\mathrm{e}}\Phi_{\mathrm{e}}}\Delta\boldsymbol{\Phi}_{\mathrm{e}}^{\mathrm{T}}.
\end{aligned}
\tag{4.19}
$$

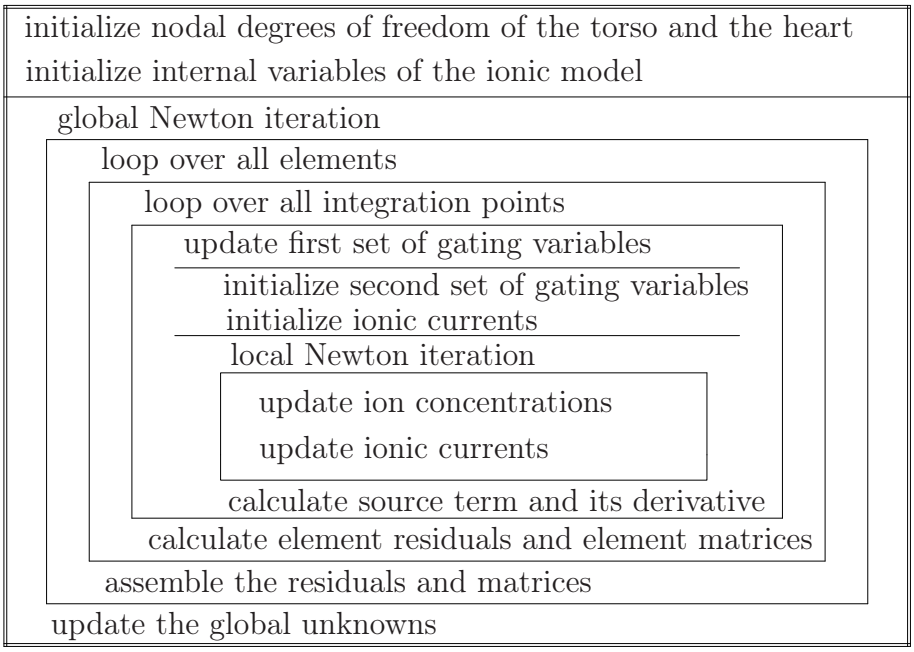

Figure 4.1: Algorithmic box of the FEM solution.

Using $(4.19)_2$, the incremental unknowns of the torso nodes can be carried out as follows:

$$\Delta\boldsymbol{\Phi}_{\mathrm{e}}^{\mathrm{T}} = \boldsymbol{K}_{\mathrm{TT}}^{\Phi_{\mathrm{e}}\Phi_{\mathrm{e}}{}^{-1}}\big[\boldsymbol{R}_{\mathrm{T}}^{\Phi_{\mathrm{e}}} - \boldsymbol{K}_{\mathrm{T\Gamma}}^{\Phi_{\mathrm{e}}\Phi_{\mathrm{e}}}\Delta\boldsymbol{\Phi}_{\mathrm{e}}^{\Gamma}\big]. \tag{4.20}$$

Then, inserting (4.20) into $(4.19)_1$,

$$\begin{aligned}\boldsymbol{R}_{\Gamma}^{\Phi_{\mathrm{e}}} = \;& \boldsymbol{K}_{\Gamma\mathrm{H}}^{\Phi_{\mathrm{e}}\Phi}\Delta\boldsymbol{\Phi}^{\mathrm{H}} + \boldsymbol{K}_{\Gamma\mathrm{H}}^{\Phi_{\mathrm{e}}\Phi_{\mathrm{e}}}\Delta\boldsymbol{\Phi}_{\mathrm{e}}^{\mathrm{H}} + \boldsymbol{K}_{\Gamma\Gamma}^{\Phi_{\mathrm{e}}\Phi}\Delta\boldsymbol{\Phi}^{\Gamma} + \boldsymbol{K}_{\Gamma\Gamma}^{\Phi_{\mathrm{e}}\Phi_{\mathrm{e}}}\Delta\boldsymbol{\Phi}_{\mathrm{e}}^{\Gamma} + \\ & \boldsymbol{K}_{\Gamma\mathrm{T}}^{\Phi_{\mathrm{e}}\Phi_{\mathrm{e}}}\boldsymbol{K}_{\mathrm{TT}}^{\Phi_{\mathrm{e}}\Phi_{\mathrm{e}}{}^{-1}}\big[\boldsymbol{R}_{\mathrm{T}}^{\Phi_{\mathrm{e}}} - \boldsymbol{K}_{\mathrm{T\Gamma}}^{\Phi_{\mathrm{e}}\Phi_{\mathrm{e}}}\Delta\boldsymbol{\Phi}_{\mathrm{e}}^{\Gamma}\big],\end{aligned} \tag{4.21}$$

and decoupling the residual and the unknowns as

$$\begin{aligned}\boldsymbol{R}_{\Gamma}^{\Phi_{\mathrm{e}}} - \boldsymbol{K}_{\Gamma\mathrm{T}}^{\Phi_{\mathrm{e}}\Phi_{\mathrm{e}}}\boldsymbol{K}_{\mathrm{TT}}^{\Phi_{\mathrm{e}}\Phi_{\mathrm{e}}{}^{-1}}\boldsymbol{R}_{\mathrm{T}}^{\Phi_{\mathrm{e}}} \;=\; & \boldsymbol{K}_{\Gamma\mathrm{H}}^{\Phi_{\mathrm{e}}\Phi}\Delta\boldsymbol{\Phi}^{\mathrm{H}} + \boldsymbol{K}_{\Gamma\mathrm{H}}^{\Phi_{\mathrm{e}}\Phi_{\mathrm{e}}}\Delta\boldsymbol{\Phi}_{\mathrm{e}}^{\mathrm{H}} + \boldsymbol{K}_{\Gamma\Gamma}^{\Phi_{\mathrm{e}}\Phi}\Delta\boldsymbol{\Phi}^{\Gamma} + \\ & \big[\;\boldsymbol{K}_{\Gamma\Gamma}^{\Phi_{\mathrm{e}}\Phi_{\mathrm{e}}} - \boldsymbol{K}_{\Gamma\mathrm{T}}^{\Phi_{\mathrm{e}}\Phi_{\mathrm{e}}}\boldsymbol{K}_{\mathrm{TT}}^{\Phi_{\mathrm{e}}\Phi_{\mathrm{e}}{}^{-1}}\boldsymbol{K}_{\mathrm{T\Gamma}}^{\Phi_{\mathrm{e}}\Phi_{\mathrm{e}}}\big]\Delta\boldsymbol{\Phi}_{\mathrm{e}}^{\Gamma},\end{aligned} \tag{4.22}$$

and if we define a new matrix and an array as

$$\begin{aligned} \bar{\boldsymbol{K}}_{\Gamma\Gamma}^{\Phi_e\Phi_e} &= \boldsymbol{K}_{\Gamma\Gamma}^{\Phi_e\Phi_e} - \boldsymbol{K}_{\Gamma T}^{\Phi_e\Phi_e} \boldsymbol{K}_{TT}^{\Phi_e\Phi_e{}^{-1}} \boldsymbol{K}_{T\Gamma}^{\Phi_e\Phi_e}, \\ \bar{\boldsymbol{R}}_{\Gamma}^{\Phi_e} &= \boldsymbol{R}_{\Gamma}^{\Phi_e} - \boldsymbol{K}_{\Gamma T}^{\Phi_e\Phi_e} \boldsymbol{K}_{TT}^{\Phi_e\Phi_e{}^{-1}} \boldsymbol{R}_{T}^{\Phi_e}, \end{aligned} \tag{4.23}$$

we end up with the following condensed solution matrix of the problem.

$$\begin{bmatrix} \boldsymbol{K}_{HH}^{\Phi\Phi} & \boldsymbol{K}_{HH}^{\Phi\Phi_e} & \boldsymbol{K}_{H\Gamma}^{\Phi\Phi} & \boldsymbol{K}_{H\Gamma}^{\Phi\Phi_e} \\ \boldsymbol{K}_{HH}^{\Phi_e\Phi} & \boldsymbol{K}_{HH}^{\Phi_e\Phi_e} & \boldsymbol{K}_{H\Gamma}^{\Phi_e\Phi} & \boldsymbol{K}_{H\Gamma}^{\Phi_e\Phi_e} \\ \boldsymbol{K}_{\Gamma H}^{\Phi\Phi} & \boldsymbol{K}_{\Gamma H}^{\Phi\Phi_e} & \boldsymbol{K}_{\Gamma\Gamma}^{\Phi\Phi} & \boldsymbol{K}_{\Gamma\Gamma}^{\Phi\Phi_e} \\ \boldsymbol{K}_{\Gamma H}^{\Phi_e\Phi} & \boldsymbol{K}_{\Gamma H}^{\Phi_e\Phi_e} & \boldsymbol{K}_{\Gamma\Gamma}^{\Phi_e\Phi} & \bar{\boldsymbol{K}}_{\Gamma\Gamma}^{\Phi_e\Phi_e} \end{bmatrix} \begin{bmatrix} \Delta\boldsymbol{\Phi}^{H} \\ \Delta\boldsymbol{\Phi}_e^{H} \\ \Delta\boldsymbol{\Phi}^{\Gamma} \\ \Delta\boldsymbol{\Phi}_e^{\Gamma} \end{bmatrix} = \begin{bmatrix} \boldsymbol{R}_{H}^{\Phi} \\ \boldsymbol{R}_{H}^{\Phi_e} \\ \boldsymbol{R}_{\Gamma}^{\Phi} \\ \bar{\boldsymbol{R}}_{\Gamma}^{\Phi_e} \end{bmatrix} \tag{4.24}$$

After the unknowns of the heart computed using the condensed matrix, the unknowns of the torso can be recovered by

$$\Delta\boldsymbol{\Phi}_e^{T} = \boldsymbol{K}_{TT}^{\Phi_e\Phi_e{}^{-1}} \left[\boldsymbol{R}_{T}^{\Phi_e} - \boldsymbol{K}_{T\Gamma}^{\Phi_e\Phi_e} \Delta\boldsymbol{\Phi}_e^{\Gamma} \right] \tag{4.25}$$

This reduced form is iteratively updated as in the regular FEM, using (4.18). Because of the fact that the size of the heart is very small compared to the size of the human body, the bimaterial problem at hand includes relatively many torso unknowns. Hence, rearranging the global solution matrix and storing the inverse of the linear and time-independent part of it, which is denoted as $\boldsymbol{K}_{TT}^{\Phi_e\Phi_e{}^{-1}}$, the size of the global solution matrix reduced, drastically. Owing to the condensation, the solution matrix can be much more easily inverted due to the highly reduced form. Once the solution is obtained through the modified solution matrix and vector, the computed values of the heart and interface unknowns are used to recover the unknowns of the torso nodes by using (4.25) at each iteration.

4.3 The Boundary Element Method and the FEM-BEM Coupling

The boundary element method is based on the idea of approximating the solution of a partial differential equation on the boundary, and then, using the solution obtained on the boundary to solve the inner domain. The advantage

of this approach is that in order to solve a linear problem numerically, only the boundaries are discretized. It is an efficient method, especially if the FEM approximation requires too many elements and nodes for an accurate solution. The disadvantages of the method is that it may be difficult to implement the solution procedure for a nonlinear or inhomogeneous problem. Further, the method requires a fundamental solution, which can be unavailable in some cases.

The torso is a linear and isotropic conductor of electricity. The solution of the Laplace equation using the boundary element method is straightforward. Therefore, the differential equation defining the torso can be solved using the boundary element method. First, the fundamental solution of the governing differential equation should be determined. In the torso model, the only field variable is the extracellular potential Φ_e. Therefore, the Laplace equation is

$$-\operatorname{div}(\boldsymbol{D}_T \cdot \nabla \Phi_e) = 0. \tag{4.26}$$

The analytical solution of a PDE in an infinite domain with a point source is the fundamental solution of the corresponding PDE. In the two dimensional setting, the fundamental solution of the Laplace equation is given as

$$\mathrm{w} = \frac{-1}{2\pi} \ln r \tag{4.27}$$

where r is the distance between two points. For the derivation of the fundamental solution of the Laplace equation and for further information about the BEM, the reader is referred to [69].

In order to solve a PDE with the BEM, a weight function should be selected. The weight function of the BEM, apart from FEM, is the fundamental solution of the differential equation. Multiplying the Laplace equation with the weight function and employing the integration by parts twice and then employing Gauss's

theorem, the boundary integral equation is found to be

$$\mathrm{c(p)}\Phi_{\mathrm{e}}(\mathrm{p}) + \int\limits_{\partial\mathcal{B}^{\mathrm{e}}} \Phi_{\mathrm{e}} \frac{\partial \mathrm{w}}{\partial \mathrm{n}}\, \mathrm{d}s = \int\limits_{\partial\mathcal{B}^{\mathrm{e}}} \mathrm{w} \frac{\partial \Phi_{\mathrm{e}}}{\partial \mathrm{n}}\, \mathrm{d}s. \tag{4.28}$$

In (4.28), s refers to the overall surface of the domain $\mathcal{B}$, p refers to any point in the space and c(p) refers to a constant depending on the spatial position of the point p. If p is a point inside the domain, c(p) is 1 and if it is on a continuous surface of the domain, c(p) is 0.5. If the point is out of the domain, c(p) is 0.

$$\mathrm{c(p)} = \begin{cases} 1 & \text{if } \mathrm{p} \in \mathcal{B}, \\ 0.5 & \text{if } \mathrm{p} \in \partial\mathcal{B}, \quad \mathcal{B} \text{ smooth}, \\ 0 & \text{if } \mathrm{p} \notin \partial\mathcal{B}\ . \end{cases} \tag{4.29}$$

In order to apply the BEM to the problem at hand, the surface domain is discretized into $\mathrm{n_{line}}$ elements. The domains and boundaries of the problem are given in Figure 4.2. The equations are solved at the midpoint of each line element. Therefore, the constant c(p) is selected to be 0.5, due to the continuity of the point. Furthermore, the variables and their gradients are assumed to be constant on each element, whereas they are not continuous at the nodes. Owing to these assumptions, (4.28) is recast into the following discrete form:

$$\frac{1}{2}\Phi_{\mathrm{e}}^{\mathrm{i}} + \sum_{\mathrm{j}=1}^{\mathrm{n_{line}}} \Big[\int\limits_{\partial s} \Phi_{\mathrm{e}} \tilde{\mathrm{q}} \mathrm{d}s \Big] = \sum_{\mathrm{j}=1}^{\mathrm{n_{line}}} \Big[\int\limits_{\partial s} \mathrm{w}\mathrm{q}\mathrm{d}s \Big], \tag{4.30}$$

where $\tilde{\mathrm{q}} = \nabla \mathrm{w} \cdot n$. Because of the fact that the global variable Φ_{e} and its gradient q are constant on each element, (4.30) can be written as follows:

$$\frac{1}{2}\Phi_{\mathrm{e}}^{\mathrm{i}} + \sum_{\mathrm{j}=1}^{\mathrm{n_{line}}} \Phi_{\mathrm{e}}^{\mathrm{j}} \Big[\int\limits_{\partial s_{\mathrm{j}}} \tilde{\mathrm{q}} \mathrm{d}s \Big] = \sum_{\mathrm{j}=1}^{\mathrm{n_{line}}} \mathrm{q}^{\mathrm{j}} \Big[\int\limits_{\partial s_{\mathrm{j}}} \mathrm{w}\mathrm{d}s \Big] \tag{4.31}$$

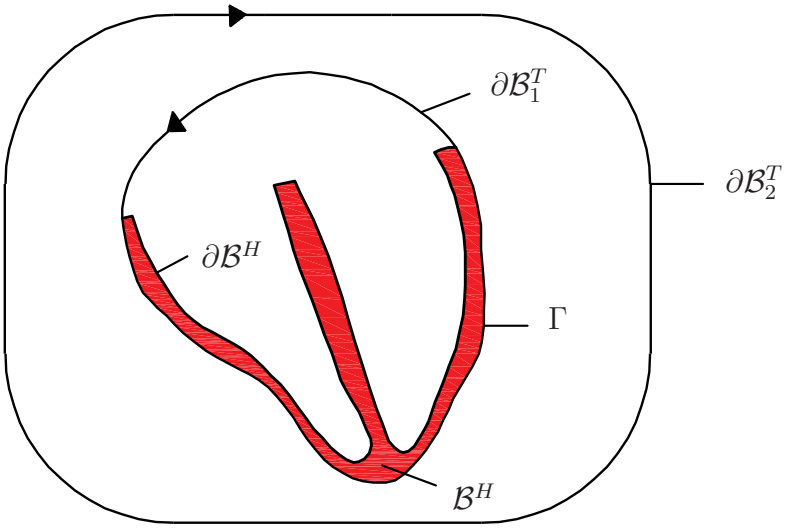

Figure 4.2: Boundaries of the FEM-BEM coupling.

In (4.31), the two integral terms can be rewritten in the form,

$$\hat{\mathrm{H}}^{\mathrm{ij}} = \int_{\partial s_{\mathrm{j}}} \tilde{\mathrm{q}} \mathrm{d}s \ ; \quad \mathrm{G}^{\mathrm{ij}} = \int_{\partial s_{\mathrm{j}}} \mathrm{w} \mathrm{d}s. \tag{4.32}$$

In the calculation of the matrix $\tilde{\mathrm{H}}$, if linear elements are used and i=j, the point i is singular. The reason for that is if i=j, then the distance is zero. In order to solve this problem, analytic solution can be employed [69] or Gaussian quadrature with several points can be applied. In addition to these solutions, at every node i, the following correction should be implemented:

$$\mathrm{H}^{\mathrm{ij}} = \begin{cases} \hat{\mathrm{H}}^{\mathrm{ij}} & \text{if} \quad \mathrm{i} \neq \mathrm{j}, \\ \hat{\mathrm{H}}^{\mathrm{ij}} + 0.5 & \text{if} \quad \mathrm{i} = \mathrm{j}. \end{cases} \tag{4.33}$$

Then, the overall equation system can be written in the following form:

$$\sum_{j=1}^{n_{line}} \Phi_e^j H^{ij} = \sum_{j=1}^{n_{line}} q^j G^{ij} \tag{4.34}$$

This equation is a matrix equation $\boldsymbol{H\Phi_e}$=$\boldsymbol{Gq}$ where $\boldsymbol{H}$ and $\boldsymbol{G}$ are the $n_{line} \times n_{line}$ BEM matrices, $\boldsymbol{\Phi_e}$ and $\boldsymbol{q}$ are the vectors of length n_{line} representing the extracellular potentials and normal flux terms of the boundary elements. For the solution of this system, the knowns and the unknowns are separated according to boundary conditions. For a Neumann boundary condition, the potentials are unknowns, whereas for a Dirichlet boundary condition, surface fluxes are the unknowns. It is worth noting that for the bimaterial problem at hand, the purpose is to discretize the surface of the torso only, and neglect the interior part of the torso domain. Therefore, there are two surfaces for this case. The first surface is the outer torso surface and the second surface is the heart surface. The nonlinear equations of the heart model are solved with the FEM and the results obtained this solution is the boundary condition for the BEM, for that specific time step. Therefore, on the surface of the heart, the BEM and FEM equations are coupled. The coupling equations are derived through the following matrix representation of the BEM:

$$\begin{bmatrix} \boldsymbol{H}_{\Gamma\Gamma} & \boldsymbol{H}_{\Gamma T} \\ \boldsymbol{H}_{T\Gamma} & \boldsymbol{H}_{TT} \end{bmatrix} \begin{bmatrix} \boldsymbol{\Phi}_e^{\Gamma} \\ \boldsymbol{\Phi}_e^{T} \end{bmatrix} = \begin{bmatrix} \boldsymbol{G}_{\Gamma\Gamma} & \boldsymbol{G}_{\Gamma T} \\ \boldsymbol{G}_{T\Gamma} & \boldsymbol{G}_{TT} \end{bmatrix} \begin{bmatrix} \boldsymbol{q}_{\boldsymbol{\Gamma}} \\ 0 \end{bmatrix} \tag{4.35}$$

It is important to note that the BEM solution will be for the extracellular potential of the torso domain. The matrices are partitioned according to the knowns and unknowns of the solution procedure. In this equation system, $\boldsymbol{\Phi_e^T}$ refers to the unknown potentials of the BEM, which are the outer surface potentials of the torso. The potentials of the heart surface, on the other hand, is denoted by $\boldsymbol{\Phi_e^{\Gamma}}$, and these potentials are computed with the FEM. Consequently, $\boldsymbol{q_T}$ is the known flux values, which are 0 on the torso surface, due to the homogeneous Neumann boundary conditions and $\boldsymbol{q}_{\Gamma}$ are the unknown surface fluxes of the

heart surface. The two equation systems can be written in the following form:

$$\begin{aligned} \boldsymbol{H}_{\Gamma\Gamma}\boldsymbol{\Phi}_e^{\boldsymbol{\Gamma}} + \boldsymbol{H}_{\Gamma\mathrm{T}}\boldsymbol{\Phi}_e^{\boldsymbol{T}} &= \boldsymbol{G}_{\Gamma\Gamma}\boldsymbol{q}_\Gamma + \boldsymbol{G}_{\Gamma\mathrm{T}} \cdot 0, \\ \boldsymbol{H}_{\mathrm{T}\Gamma}\boldsymbol{\Phi}_e^{\boldsymbol{\Gamma}} + \boldsymbol{H}_{\mathrm{TT}}\boldsymbol{\Phi}_e^{\boldsymbol{T}} &= \boldsymbol{G}_{\mathrm{T}\Gamma}\boldsymbol{q}_\Gamma + \boldsymbol{G}_{\mathrm{TT}} \cdot 0. \end{aligned} \tag{4.36}$$

As mentioned earlier, the flux values on the outer torso surface, $\boldsymbol{q}_T$, are zero. Using $(4.36)_2$, the extracellular potential can be rewritten in terms of fluxes and potentials on the surface of the heart.

$$\boldsymbol{\Phi}_{\mathrm{e}}^{\mathrm{T}} = \boldsymbol{H}_{\mathrm{TT}}^{-1}[\boldsymbol{G}_{\mathrm{T}\Gamma}\boldsymbol{q}_\Gamma - \boldsymbol{H}_{\mathrm{T}\Gamma}\boldsymbol{\Phi}_{\mathrm{e}}^{\Gamma}] \tag{4.37}$$

Implementing (4.37) into $(4.36)_1$, the equation takes the form

$$\boldsymbol{H}_{\Gamma\Gamma}\boldsymbol{\Phi}_e^{\boldsymbol{\Gamma}} + \boldsymbol{H}_{\Gamma\mathrm{T}}\boldsymbol{H}_{\mathrm{TT}}^{-1}[\boldsymbol{G}_{\mathrm{T}\Gamma}\boldsymbol{q}_\Gamma - \boldsymbol{H}_{\mathrm{T}\Gamma}\boldsymbol{\Phi}_e^{\boldsymbol{\Gamma}}] = \boldsymbol{G}_{\Gamma\Gamma}\boldsymbol{q}_\Gamma. \tag{4.38}$$

And, by decoupling the variables we obtain

$$[\boldsymbol{H}_{\Gamma\Gamma} - \boldsymbol{H}_{\Gamma\mathrm{T}}\boldsymbol{H}_{\mathrm{TT}}^{-1}\boldsymbol{H}_{\mathrm{T}\Gamma}]\boldsymbol{\Phi}_{\mathrm{e}}^{\Gamma} = [\boldsymbol{G}_{\Gamma\Gamma} - \boldsymbol{H}_{\Gamma\mathrm{T}}\boldsymbol{H}_{\mathrm{TT}}^{-1}\boldsymbol{G}_{\mathrm{T}\Gamma}]\boldsymbol{q}_\Gamma. \tag{4.39}$$

Introducing new matrices $\tilde{\boldsymbol{H}}$ and $\tilde{\boldsymbol{G}}$, and defining them as

$$\tilde{\boldsymbol{H}} = [\boldsymbol{H}_{\Gamma\Gamma} - \boldsymbol{H}_{\Gamma\mathrm{T}}\boldsymbol{H}_{\mathrm{TT}}^{-1}\boldsymbol{H}_{\mathrm{T}\Gamma}] \ ; \quad \tilde{\boldsymbol{G}} = [\boldsymbol{G}_{\Gamma\Gamma} - \boldsymbol{H}_{\Gamma\mathrm{T}}\boldsymbol{H}_{\mathrm{TT}}^{-1}\boldsymbol{G}_{\mathrm{T}\Gamma}], \tag{4.40}$$

the flux terms of the heart surface can be expresses in terms of the potentials of the heart surface explicitly,

$$\boldsymbol{q}_{\boldsymbol{\Gamma}} = \tilde{\boldsymbol{G}}^{-1}\tilde{\boldsymbol{H}}\boldsymbol{\Phi}_{\mathrm{e}}^{\Gamma}. \tag{4.41}$$

It is important to note that the BEM matrices $\tilde{\boldsymbol{H}}$ and $\tilde{\boldsymbol{G}}$ are time-indepenedent. Therefore, they are computed and stored once and for all at the beginning of the analysis.

These computed fluxes are treated as external fluxes on the heart surface, and implemented to the residual contribution of the surface nodes, then, the BEM and FEM are coupled on the heart surface, leading to a much shorter solution time. The residual contribution of these external fluxes is provided with,

$$\mathrm{R}_{\mathrm{I}_\Gamma}^{\Phi_\mathrm{e}} = \mathrm{R}_{\mathrm{I}_\Gamma}^{\Phi_\mathrm{e}} + \mathop{\mathsf{A}}_{\mathrm{j}=1}^{\mathrm{n_{line}}} \Big\{ \int_{\Gamma} \mathrm{N}^{\mathrm{a}} q_{\Gamma_j} \, \mathrm{dA} \Big\}. \tag{4.42}$$

where, I_Γ denotes the interface nodes between the torso and the heart, N^{a} is the shape function for the surface elements, with $\mathrm{a}=1,..\mathrm{n}_{\mathrm{en}}$.

The finite element discretization, condensation of the stiffness matrix and the boundary element finite element coupling are introduced in Chapter 4. In Chapter 5, the results of the representative numeric examples are provided. The performance of the three methods are compared in terms of computational speed. Furthermore, the simulation results of selected two disease cases that are modeled using a realistic heart and torso geometry are illustrated.

CHAPTER 5

NUMERICAL EXAMPLES

This chapter is devoted to the numerical examples representing the integrated cardiac electrophysiology problem. The efficiency of the proposed C-FEM and FEM-BEM approaches are demonstrated through the ECG simulations. In order to simulate an ECG, first the mesh size of the finite element solution is determined. The mesh sizes of the torso and the heart are settled upon after a series of analyses. After these convergence analyses, the calibration of the time step is provided. Then, using the calibrated time step and mesh size, the ECG simulations are conducted. The solution times of the methods are provided with the CPU time comparison of the ECG simulations. The validity of the simulated ECG in terms of practical medicine is discussed. Moreover, the performance of our model is illustrated with a disease scenario. The ECG results of the inferior infarction simulation are demonstrated with the illustrative figures.

5.1 Determination of the Mesh Size

In order to obtain accurate results with the FEM and C-FEM, the mesh size of the heart and the torso are determined with sensitivity analyses. If the mesh is coarse, the solution of the highly stiff ionic model may lead to significant errors and fluctuations.

The nonlinear problem of the heart domain is solved together with the linear problem of the torso. The parameter set of the governing differential equations are provided in Table 5.1.

These parameters are selected because of the fact that the ECG leads obtained

Table 5.1: Parameters of the integrated electrophysiology equations

Parameter	Unit	Description	Values
$\bar{d}^i_{\parallel} := d^i_{\parallel}/\mathcal{X}\mathcal{C}_m$	[mm^2/s]	Normalized intracellular conductance of the heart in the longitudinal direction	10.0
$\bar{d}^i_{\perp} := d^i_{\perp}/\mathcal{X}\mathcal{C}_m$	[mm^2/s]	Normalized intracellular conductance of the heart in the orthogonal direction	1.0
$\bar{d}^e_{\parallel} := d^e_{\parallel}/\mathcal{X}\mathcal{C}_m$	[mm^2/s]	Normalized extracellular conduction of the heart in the longitudinal direction	10.0
$\bar{d}^e_{\perp} := d^e_{\perp}/\mathcal{X}\mathcal{C}_m$	[mm^2/s]	Normalized extracellular conductance of the heart in the orthogonal direction	3.0
d^T_{iso}	[mm^2/s]	Isotropic conductance of the torso	1.0
θ	[Rad]	Fiber orientation angle of the heart tissue	0.0

with these parameters are accurate [42, 70]. The conductivity constants of the heart tissue and the torso are not exact. Therefore, there are several approaches for the determination of the cardiac conductivity. In the recent years, one of the most effective approaches is to construct a proportionality relation between the orthogonal and longitudinal conductivites. Roth proposed a mathematical model and related the auxillary parameters to bidomain conductivities [70]. Therefore, if the conductivity of the intracellular domain is determined accurately, other three conductivity parameters can be computed easily.

The heart domain is at the resting state initially. Therefore, the initial value of the heart domain is -86.2 mV, and the initial value of the torso domain is 0 mV, since there is no electrical activity in the torso. Then, the midpoint of the plate is stimulated with a potential of +20 mV, and the action potential starts to propagate. The boundary condition of the outer torso surface is homogeneous Neumann boundary condition, while on the interface there is an equilibrium between the extracellular spatial potential fluxes of the torso and the heart. The initial set of gating variables for the resting state of the heart domain are given to be $g_m = 0$, $g_h = 0$, $g_j = 0.75$, $g_d = 0$, $g_f = 1.0$, $g_{fCa} = 1.0$, $g_r = 0$, $g_s = 1$, $g_{xs} = 0$, $g_{xr1} = 0$, $g_{xr2} = 0$, $g_{xK1\infty} = 0.05$, and $g_g = 1$. Other than the gating variables, there are also four ion concentrations of the resting state, c_{Na}=11.6 mM, c_K=138.3 mM, $c_{Ca} = 0.08{\cdot}10^{-6}$ M and $c^{sr}_{Ca} = 0.56$ mM. The time step for

the ECG simulations is calibrated after the mesh size is determined. Therefore, for the mesh size selection an average time step of the ionic model is used. The time step of the ionic model can be increased up to 0.16 ms. Therefore, we used an average time step of 0.08 ms for the mesh size determination. With this setting, the mesh sizes of the heart domain and the body domain are selected after two sets of analyses, one for the determination of the size of the heart mesh, and the other is for the size of the torso mesh. The mathematical model is solved using the FEM software FEAP [71]. Moreover, all the meshes included in this study are generated with ABAQUS [72].

5.1.1 Appropriate Mesh Size for the Heart Domain

The size of the heart elements is specified with the solutions of the finite element analyses. For the finite element problem, a square domain containing both the torso and the heart is meshed with quadrilateral elements. In Figure 5.1, the boundaries and the geometry of the mesh with 64×64 element are illustrated. The interface is highlighted so that the reader can observe the boundary layer.

The heart is embedded inside the torso domain. The edge of the square heart domain is 72 mm and the edge of the square torso domain is 96 mm. The mesh sizes of the overall domain, containing the torso and the heart are altered in order to compare the results of the different mesh settings. This geometry is meshed with four different element sizes. The mesh sizes and the number of elements of the four cases are provided in the Table 5.2, where h^H denotes the mesh size of the heart domain.

Table 5.2: Selected mesh sizes for the sensitivity analysis of the heart domain.

Mesh No.	h^H[mm]	Number of Elements
Mesh 1	6	256
Mesh 2	2	2304
Mesh 3	0.67	20736
Mesh 4	0.5	36864

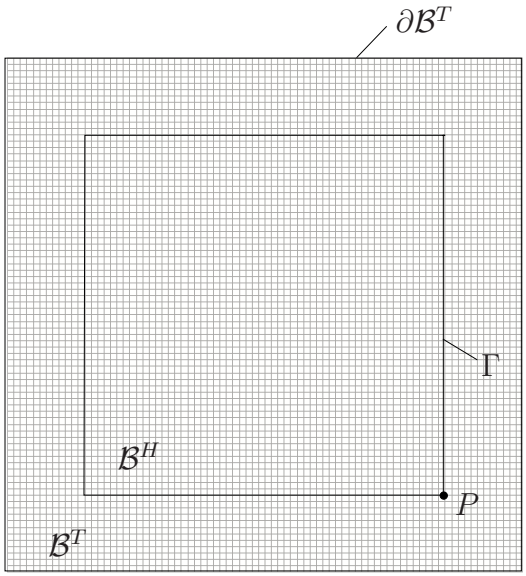

Figure 5.1: The structured 64×64 mesh including the torso and the heart elements.

The extracellular and the transmembrane potentials of the simulations are recorded at the point P shown if Figure 5.1. Point P is on the interface of the torso and the heart domains. Therefore, the effects of the both domain can be included for the sensitivity analysis. In Figure 5.2 (left), the transmembrane potential obtained with the ionic model is illustrated. The action potential waveform converges to a solution as the mesh size decreases (right). The closed box provides means to see the effect of the mesh size on the transmembrane potential. In order to illustrate the convergence rate, the required amount of time for point P to reach a potential of -40 mV is used to compute the conduction velocities of the corresponding meshes. If the distance between the point P and the stimulation point of the mesh is divided with travel times, the corresponding velocities are found. Taking the conduction velocity of the finest mesh with $\mathrm{h}^H = 0.5$ mm as the reference conduction velocity, the relative errors are computed as $\epsilon_{\mathrm{rel}} = (v\text{-}v_{\mathrm{ref}})/v_{\mathrm{ref}}$ where v is the conduction velocity and v_{ref} is the reference conduction velocity. The log-log plot of the results are provided in Figure 5.3. Since the

average slope of the lines in Figure 5.3 is about 2, it can be concluded that the convergence is quadratic.

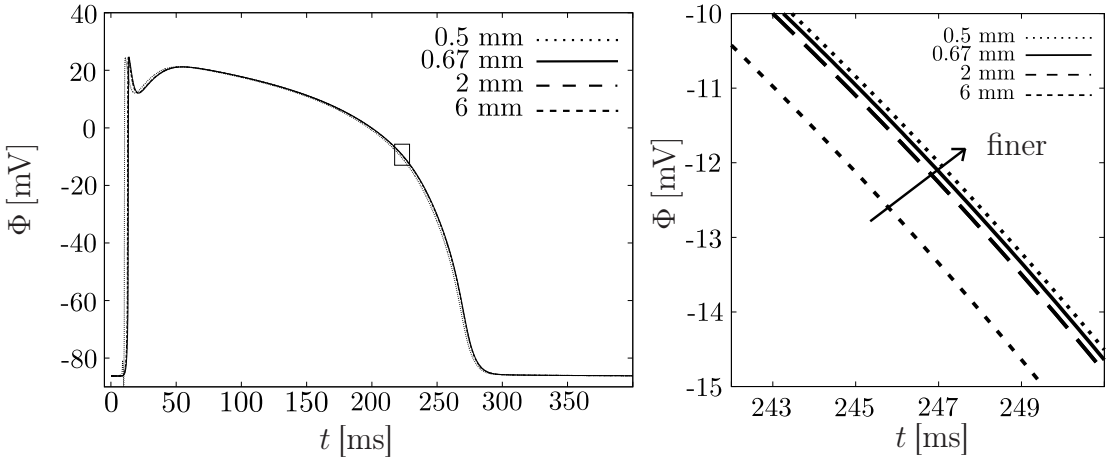

Figure 5.2: Transmembrane potentials at point P for four different mesh sizes (left) and the potentials in the close-up (right).

In Figure 5.4, on the other hand, the extracellular potential of the point P is shown. After the depolarization of the cell, the extracellular potential increases suddenly. The extracellular potential converges to a solution as the mesh size decreases.

Using the results provided in Figures 5.2 and 5.4, the mesh size of the heart domain is chosen to be $\mathrm{h}^H = 0.5$. Then, the mesh size of the torso domain should be determined with the analyses using the unstructured grids where the mesh size of the heart is fixed, but the mesh size of the torso is varied.

5.1.2 Appropriate Mesh Size for the Torso Domain

In order to be able to vary the mesh size of the torso domain, unstructured grids are used. For a better representation of the human body, the dimensions of the torso and the heart are selected to have realistic dimensions. Also, the heart domain is placed at a realistic location, shown in Figure 5.5. The illustrated mesh is composed of 25600 quadrilateral elements representing the heart domain, and

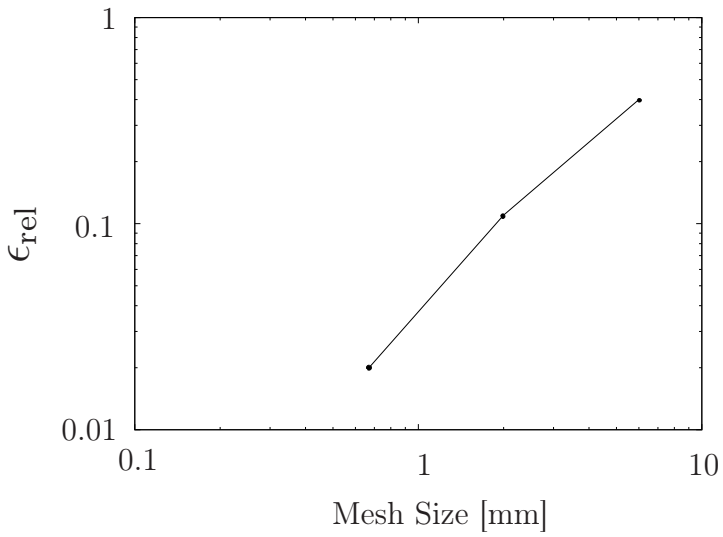

Figure 5.3: Errors in conduction velocity as the normalized difference for mesh sizes h^h= 6 mm, h^h= 2 mm and h^h= 0.67 mm . The result of the finest mesh where h^h= 0.5 mm is taken as to be the reference result.

10437 quadrilaterals representing the torso domain. The edge of the square heart domain is taken to be 72 mm, while the shorter edge and the longer edge of the torso domain are 44 cm and 50 cm, respectively. The number of heart elements in these cases is fixed and it is 25600.

Table 5.3: Selected mesh sizes for the sensitivity analysis of the torso domain.

Mesh No.	h^T_{max}[mm]	Number of Torso Elements
Mesh 1	48	10437
Mesh 2	24	19710
Mesh 3	12	30836
Mesh 4	6	49218

Using the same material parameters, initial conditions and time step, the model is simulated for these unstructured meshes. The extracellular potentials of the two points, $P1$ and $P2$, are plotted in Figure 5.6. The solution of the torso domain depends on the extracellular potential of the heart surface. As can be seen from the two waveforms, the extracellular potentials of the points are not significantly affected from the mesh size. The linear problem of the torso allows us to use coarser meshes. Therefore, the maximum mesh size of the torso domain

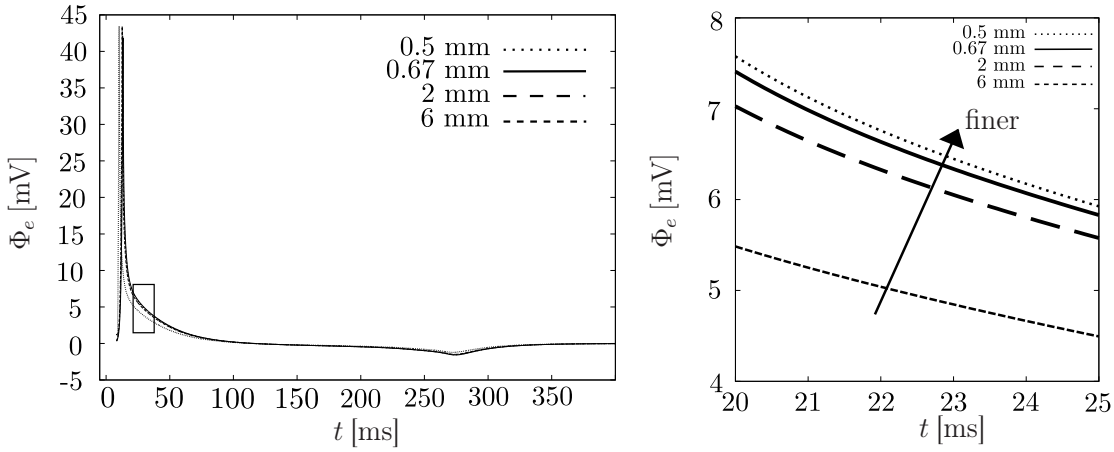

Figure 5.4: The extracellular potential at the point P (left) and the potentials in the close-up (right) for different mesh sizes.

h^T_{max} is selected to be 48 mm. The mesh size of the heart domain and the mesh size of the torso domain are determined according to the results obtained with the FEM. Finally, in order to complete the FEM calibration, the optimal time step of the analyses should be specified for the selected mesh sizes.

5.2 Appropriate Time Step for the Analysis

The optimal mesh sizes of the heart domain and the torso domain are determined so far. The last step is to calibrate the time step using the geometry shown in Figure 5.5 and using the mesh sizes of $h^H = 0.5$ mm for the heart domain and $h^T_{max} = 48$ mm for the torso domain. With this setting, the FEM is used to solve the integrated problem with time steps of $\Delta t = 0.04$, 0.08, 0.12 and 0.16 ms. The results of these analyses are provided in Figures 5.7, 5.8 and 5.9.

In Figure 5.7, the action potential of the corner node of the heart domain corresponding to point P in Figure 5.1 is shown. Similar to the spatial domain, if the time domain is discretized into finer intervals, the results converge to a solution. The convergence of the solution is provided in Figure 5.7.

The results of the extracellular potential at the same point is illustrated in Figure 5.8. It can be observed that even though the point is on the same location of the

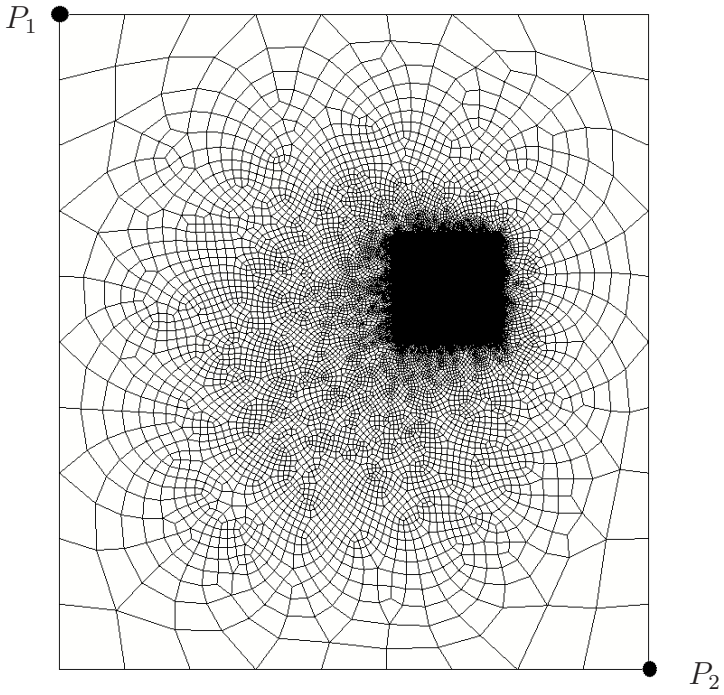

Figure 5.5: A mesh geometry for the integrated electrophysiology problem. The mesh is composed of 36037 quadrilateral elements.

heart domain, the extracellular potentials observed in Figures 5.4 and 5.8 are different. The reason for that is the effect of the torso domain. In the first case, very few torso elements are modeled, whereas in the second geometry, a very large torso domain covers the heart surface. Therefore, it can be stated that the torso influence on the extracellular potential of the interface is significant. Moreover, in Figure 5.9, the extracellular potential of the point $P1$ shown in Figure 5.5 is illustrated.

By investigating the effects of the time steps on the problem, and considering the computational efficiency, the time step is taken to be $\Delta t = 0.08$ ms for the ECG simulations.

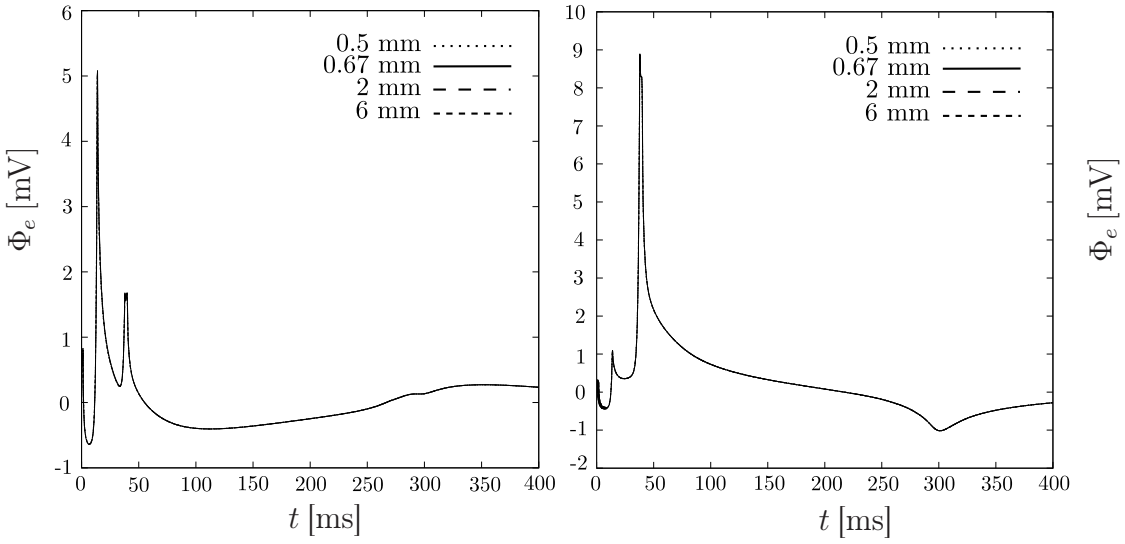

Figure 5.6: The extracellular potentials at the point P1 (left) and at point P2 (right) for different mesh sizes of the torso.

5.3 ECG Simulations

The integrated cardiac electrophysiology simulations allow us to compute the potentials out of the heart. The interaction between the heart and the torso ends up with the realistic potentials on the torso surface. By using these potentials of the torso, we can compute the discrete potential differences at each time step. These discrete potential differences eventualy provide a way to draw the standard 6-lead ECG. The leads of this diagram are computed using the following equations:

$$\begin{aligned} \mathrm{I}_\Phi &= \mathrm{LA}_\Phi - \mathrm{RA}_\Phi \\ \mathrm{II}_\Phi &= \mathrm{LF}_\Phi - \mathrm{RA}_\Phi \\ \mathrm{III}_\Phi &= \mathrm{LF}_\Phi - \mathrm{LA}_\Phi \\ \mathrm{AVF}_\Phi &= \mathrm{LF}_\Phi - \bar{\Phi} \\ \mathrm{AVL}_\Phi &= \mathrm{LA}_\Phi - \bar{\Phi} \\ \mathrm{AVR}_\Phi &= \mathrm{RA}_\Phi - \bar{\Phi} \end{aligned} \tag{5.1}$$

where LF, LA and RA stand for the left foot, left arm and right arm, respectively.

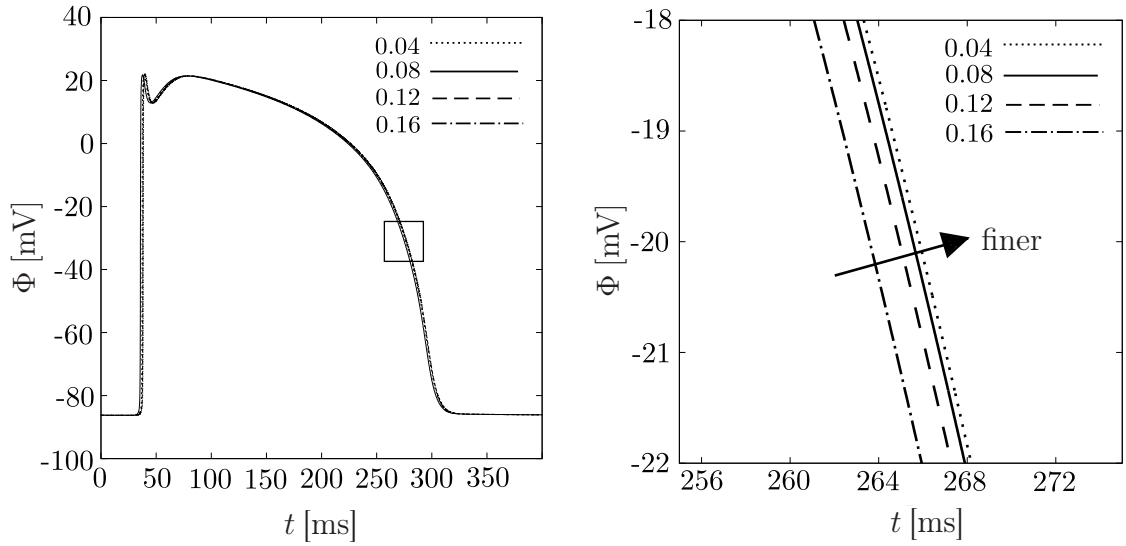

Figure 5.7: The action potential at point P (left) and the potentials in the close-up (right) for different time steps.

Moreover, $\bar{\Phi}$ is the average of the LF, LA, and RA potentials. In order to obtain a realistic ECG, the position and the geometry of the heart should be selected wisely. Moreover, the Purkinje line elements and regional characteristics of the action potential should be taken into account. The details of the mesh is provided in Figure 5.10.

The height and the width of the body section and the heart section are taken to be average. The height of the body without the foot and the head is 150 cm and the width is 45 cm. The heart, on the other hand, is assumed to be 7.5 cm in height without the atria. The cross section of the heart is obtained from the Ashley heart [73]. Furthermore, for the ECG simulation, the three points representing LA, RA, and LF points are labeled as points $P1$, $P2$, and $P3$. The mesh involves 7716 quad elements in the heart domain, 21403 quad elements in the torso domain with overall 30247 nodes. For the FEM-BEM approach, the torso domain is eliminated and outer surface elements are generated. There are 723 surface line elements on the outer surface and 1108 surface line elements on the interface.

In order to obtain an ECG accurately, the Purkinje line elements are employed.

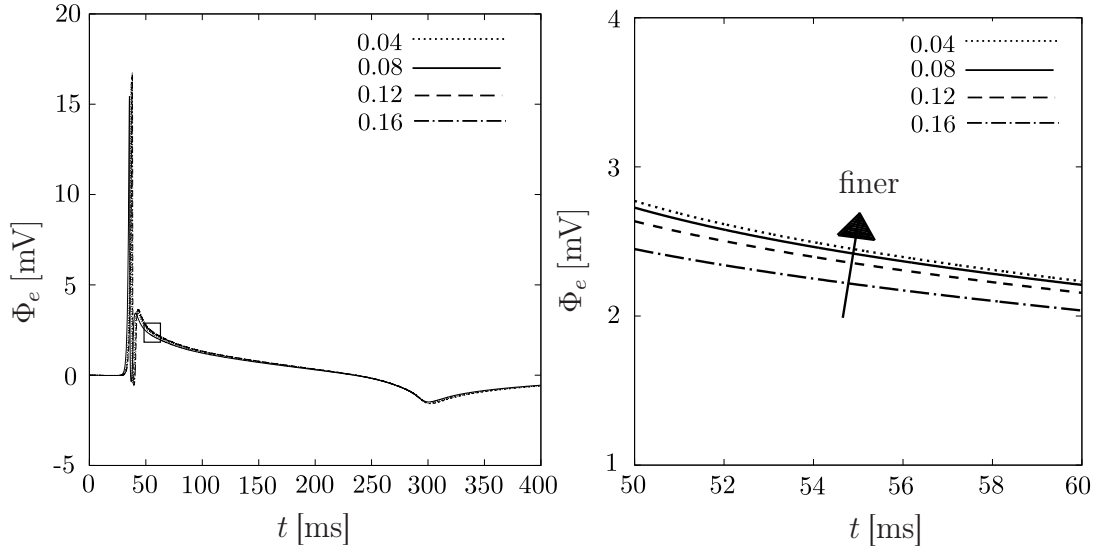

Figure 5.8: The extracellular potential changes at Point P (left) and the extracellular potentials in the close-up (right) for different time steps.

These line elements elongate through the two sides of the septum, the bundle branches and the diverge into the endocardial zones of the heart section. The Purkinje fibers are very effective electrical conductors and their material models are the same model with the cardiac domain, see Figure 5.11. Therefore, these elements are modeled with the ionic ten Tusscher model. The parameter set for the conductivities of the Purkinje fibers is listed in the Table 5.4. The Purkinje fibers have approximately twenty times higher conductance velocity than that of the regular heart tissue [42]. The conductivities in the orthogonal direction are taken to be proportional to the myocardium conductivities. The extracellular conductivity constants are the same with the myocardium.

Lastly, in order to obtain appropriate T waves with the simulation, separating the heart into zones for different action potential evolution characteristics are of great importance. Therefore, the heart domain of the mesh is divided into nine parts that have different initial ionic settings. The partition is visualized in Figure 5.12. The action potential differences are taken into account by horizontal and vertical segments. The critical point is that despite the fact that the depolarization wave reaches to the apex of the heart lastly, it repolarizes first. The reason for this is that the action potential duration is shorter at the apex of

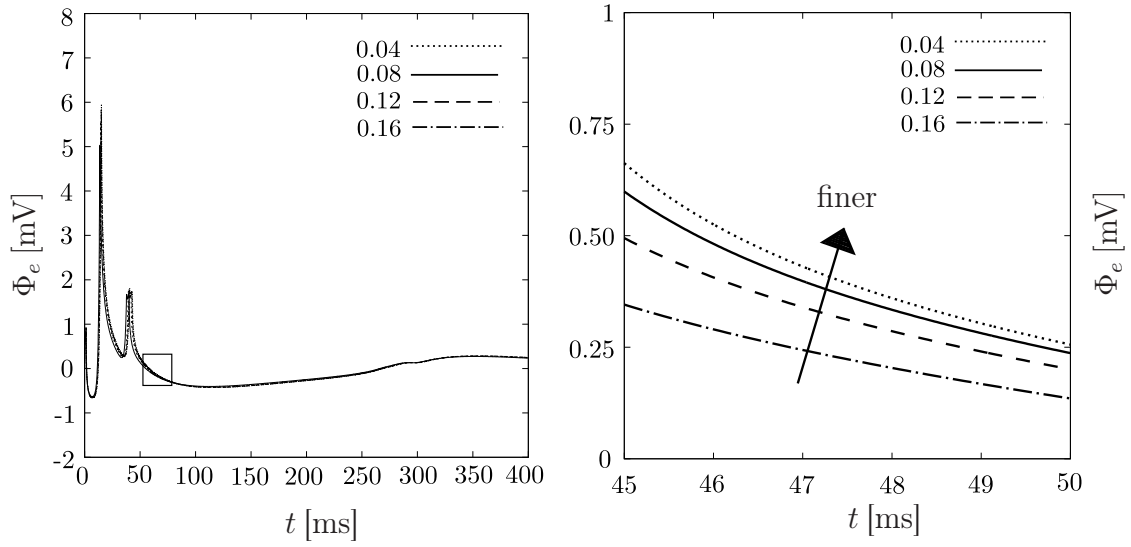

Figure 5.9: The extracellular potential at the point $P1$ (left) and close-up for different time steps.

Table 5.4: Parameters for the Purkinje elements

Parameter	Unit	Description	Values
$\bar{d}^i_{\parallel} := d^i_{\parallel}/\mathcal{X}\mathcal{C}_m$	[mm^2/s]	Normalized intracellular conductance of the heart in the longitudinal direction	200.0
$\bar{d}^i_{\perp} := d^i_{\perp}/\mathcal{X}\mathcal{C}_m$	[mm^2/s]	Normalized intracellular conductance of the heart in the orthogonal direction	30.0
$\bar{d}^e_{\parallel} := d^e_{\parallel}/\mathcal{X}\mathcal{C}_m$	[mm^2/s]	Normalized extracellular conduction of the heart in the longitudinal direction	10.0
$\bar{d}^e_{\perp} := d^e_{\perp}/\mathcal{X}\mathcal{C}_m$	[mm^2/s]	Normalized extracellular conductance of the heart in the orthogonal direction	1.0

the heart. Furthermore, the septum repolarizes a little earlier than the left side and right side of the heart. As a result, the action potential of the right and left parts are arranged to be longer. So as to change the action potential duration of the ionic model, the constants of the ionic model are changed. The major ion concentration that is responsible for the duration of the action potential wave duration is the potassium. Therefore, potassium related constants $C^{max}_{Ks,endo}$ and $C^{max}_{t0,endo}$ are decreased for a longer action potential duration. These parameters are provided in Table 3.1. These constants are 2.5% smaller than the constants

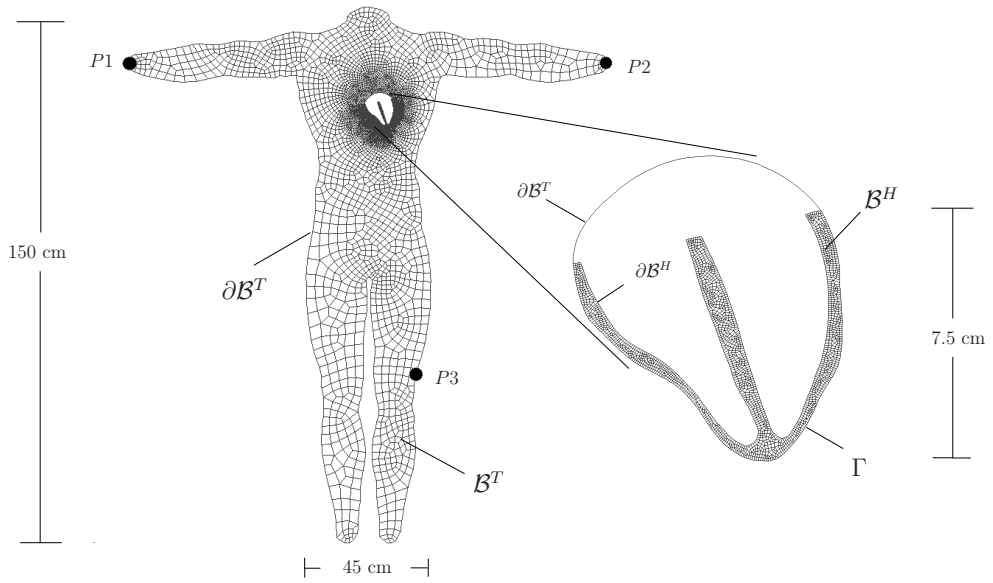

Figure 5.10: Geometric settings of the mesh.

of the lateral myocardium. Likewise, from the apex to the base, the constants are decreased by 5%. The resulting action potential durations of the nine zones are provided in Figure 5.12.

Then, using these geometrical properties, implementing Purkinje fibers and arranging the action potential durations of the myocardium, the ECG simulations are conducted. The results of the healthy and infarcted cases obtained with the FEM, C-FEM and FEM-BEM are provided in the next section.

5.3.1 Healthy ECG

The constructed model is tested for an ECG simulation of the healthy heart. The computed and normalized ECG is plotted in Figure 5.13. In Figure 5.14, the Lead-I, is plotted with a close-up. Furthermore, there are letters starting from (a) and ends up with (f) in Figure 5.14. These are the critical points of the ECG waveform. The obtained numerical results will be demonstrated at those specific instants.

The ECG in Figure 5.13 is solved by using the three approaches namely, the

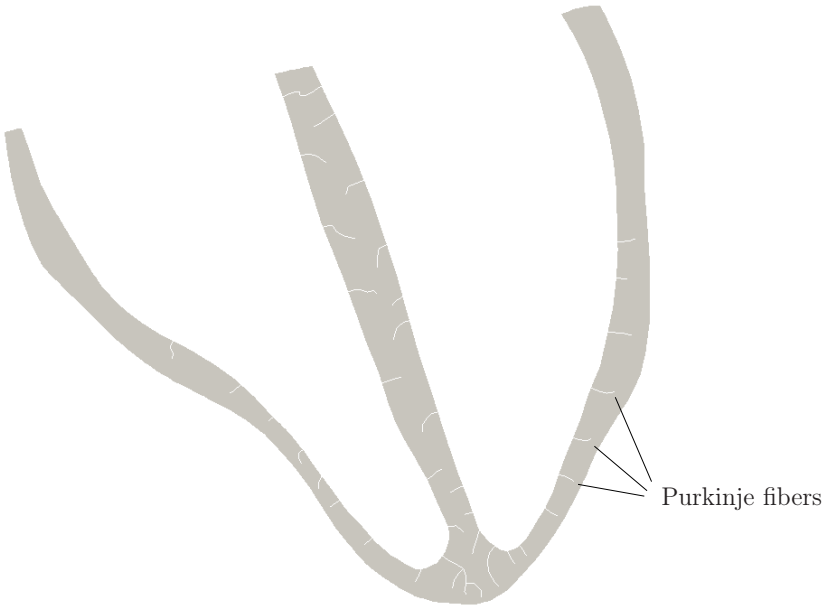

Figure 5.11: The Purkinje fibers placed on the mesh.

FEM, C-FEM and FEM-BEM on the heart surface. The CPU times of these methods are provided with Table 5.5. The solution time of the BEM is very low. The C-FEM, on the other hand, is not very effective in terms of computational speed.

The close-up in Figure 5.14 shows the solution difference between the three methods. It can be observed that the boundary element method gives very accurate results. C-FEM solution, on the other hand, gives exactly the same results with the FEM approach as expected. However, the speed of the C-FEM does not seem to be very efficient. The nonlinear domain contributes to the interface. Therefore, the residual of the linear domain should be computed at each iteration just like the FEM.

The standard 6-lead ECG structure is well characterized with the QRS complex and the T wave. The clinical results of a healthy heart shows that the model predicts the directions of the leads at the depolarization and repolarization phases, qualitatively. The timings of the QRS is acceptable, however, the ST interval

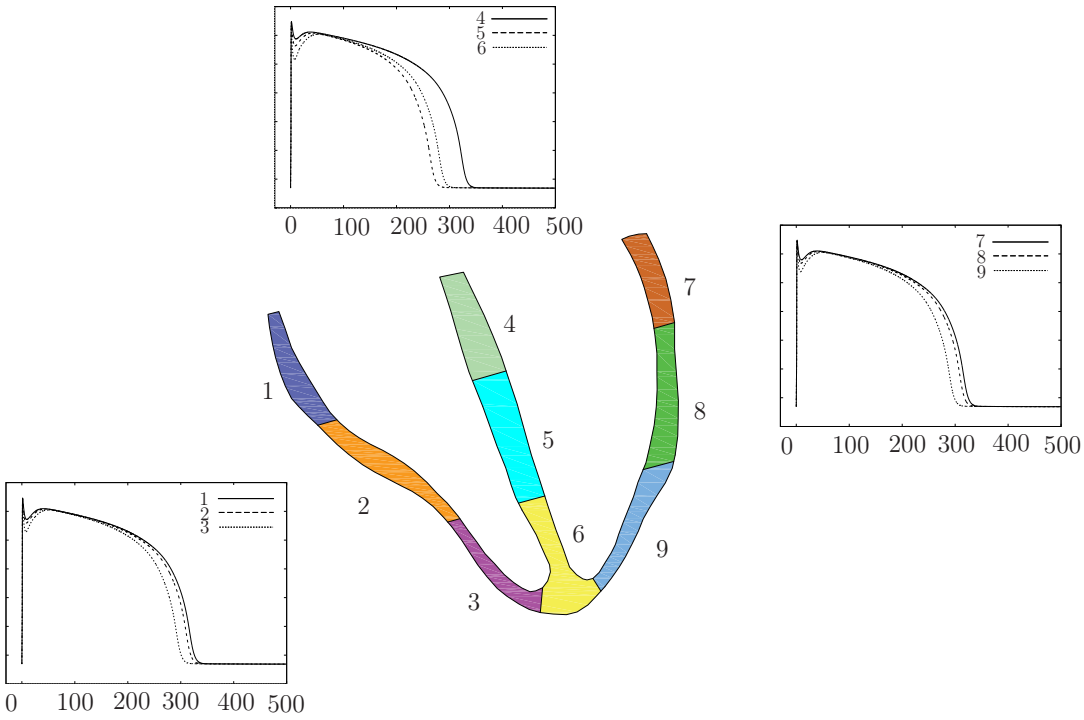

Figure 5.12: Zones of the human heart and the corresponding action potential waveforms.

is too long. The start of the T wave should be at around 300 ms. The reason for this difference is caused by the 2-D model, since the overall behavior of the ECG depends on the 3-D space. One critical issue about the modeling the ECG is the direction of the aVR lead. This lead has negative peak value and negative T wave. The ECG leads of a healthy heart are given in Figure 1.13.

In order to initiate the action potential, the top portion of the septum is stimulated by applying external flux terms on the selected nodes. The action potential propogation is provided in Figure 5.15. The action potential firstly propagates through the septum. Then, it reaches to apex and is separated into two parts, leading to left and right ventricles respectively. After a long phase named plateau, the heart starts to depolarize from the apex.

In addition to these results, the element number of the outer surface is varied for FEM-BEM approach. In Figure 5.17, the ECG simulation results are provided for 568, 723 and 948 outer line elements. It can be deduced from the figure that

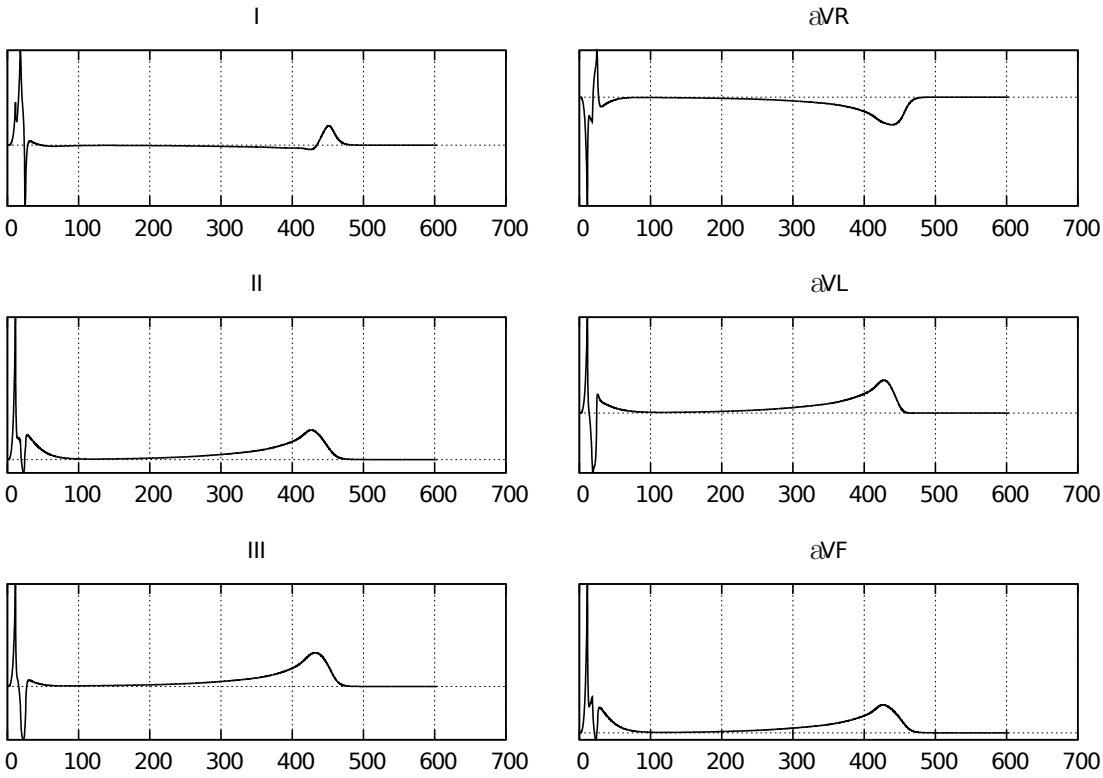

Figure 5.13: The normalized ECG of a healthy heart computed with FEM, C-FEM and FEM-BEM. Units are mV in y direction and ms in x direction.

Table 5.5: Solution times of FEM, C-FEM and FEM-BEM methods.

Method	-	CPU Time
FEM	-	107.5 min
C-FEM	-	98.2 min
FEM-BEM	-	48.8 min

as the number of BEM elements decreases, the accuracy of the solution reduces as well. The CPU Time results are also provided in Table 5.6. With the BEM, the solution time is reduced drastically, since the torso is eliminated. However, reducing the number of outer line elements does not provide further efficiency to the model.

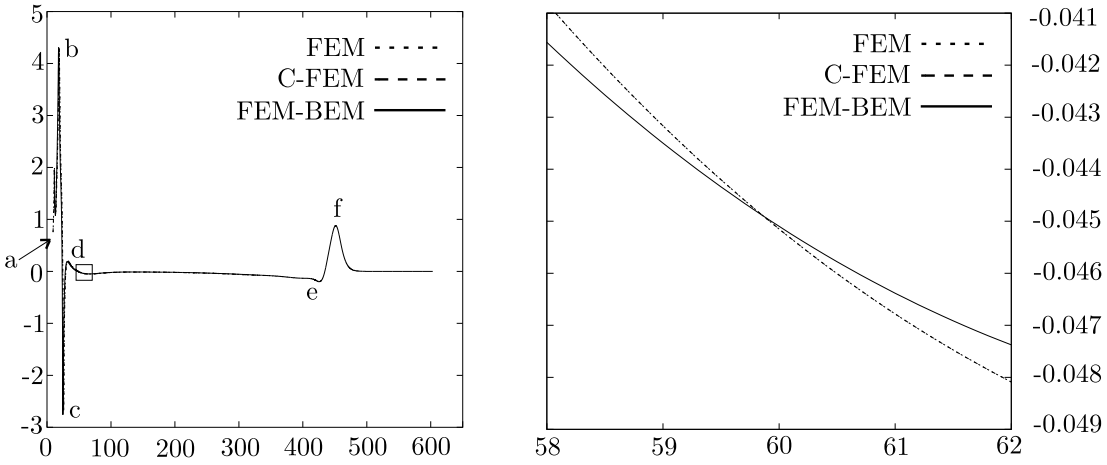

Figure 5.14: LEAD-I ECG (left) and close-up. Units are in mV in y direction and ms in x direction.

Table 5.6: FEM-BEM solution times with different numbers of outer line elements.

# of outer line el.	-	CPU Time
568	-	43.6 min
723	-	48.8 min
948	-	50.9 min

5.3.2 Modeling the Inferial Infarction

In order to test the performance of the model besides the heathy heart case, an infarction case is modeled. The model is solved with the FEM-BEM coupling, and the torso mesh is not generated. First, infarction zone is created by selecting the elements at the right hand side of the apex. These elements are shown in Figure 5.18. The infarcted region should be inexcitable for the model to properly simulate the disease. The activation phase of the cardiac cell, the depolarization, strongly depends on the sodium channels. Therefore, the sodium constant C_{Na0} is taken to be 30.0 mM and I_{NaCa}^{max} is taken to be 500.0 pA/pF. By this way, these elements become inexcitable, while the convergence of the model is maintained. All other model parameters are the same for the simulation. The results of the model is provided in Figures 5.19-5.21.

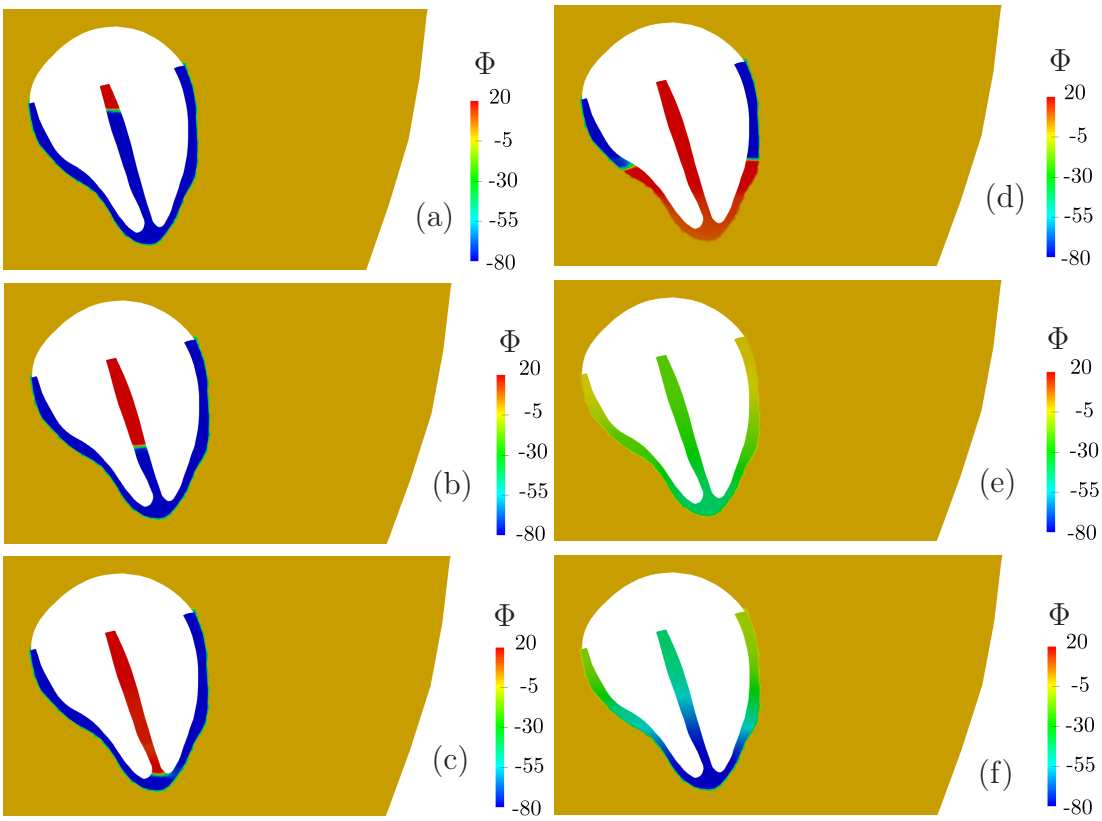

Figure 5.15: The transmembrane potential propagation through the healthy heart.

In Figure 5.19, the propogation of the transmembrane potential through the heart section can be observed. In the sequence, the action potential moves through the septum. When it reaches to the septum, the infarcted zone is not excited. The transmembrane potential continues to advance through the ventricles, but the infarcted zone remains inexcitable. Therefore, the corrupted transmembrane potential and intracellular potential changes behavior of the extracellular potential in that specific area.

In Figure 5.20, the propagation of the extracellular potential through the septum is provided. Please note that in order to represent the effects of the infarcted zone efficiently, the scale bar is not fixed, but it changes with respect to each step. As a reaction to the transmembrane potential, the extracellular potential starts to advance through the septum, and when it reaches to the apex, the infarcted zone does not react to extracellular stimulation as well. Therefore,

the boundary conditions of the coupled FEM-BEM problem changes. The scar tissue prevents the potential to reach to the left foot. Therefore, second, third leads and the aVF lead of the ECG should have different peaks.

The ECGs obtained through the solutions of the healthy heart and the infarcted heart are provided in Figure 5.21. The effect of the infarcted zone can be seen in leads II, III and aVF easily. The S wave of the lead-II can not go below zero, resulting in elevated T wave. It is the common indicator of diseases related to the septum. Lead-III, on the other hand, cannot even increase in the depolarization phase, simply because the infarcted zone blocks the potential in the downward direction. Another critical point verifying the validity of the obtained ECG is that the lead-I and aVR does not change significantly due to the infarction. This is acceptable because of the infarcted zone is at the bottom of the heart. The effects of the potential of the lower part has less effects on the upper leads.

In this section, the applications of the integrated cardiac electrophysiology problem is shown. The efficiency of the proposed algorithms are tested in ECG simulations in terms of solution time. Moreover, the accuracy of the coupled FEM-BEM approach is tested with the healthy and infarcted case scenarios.

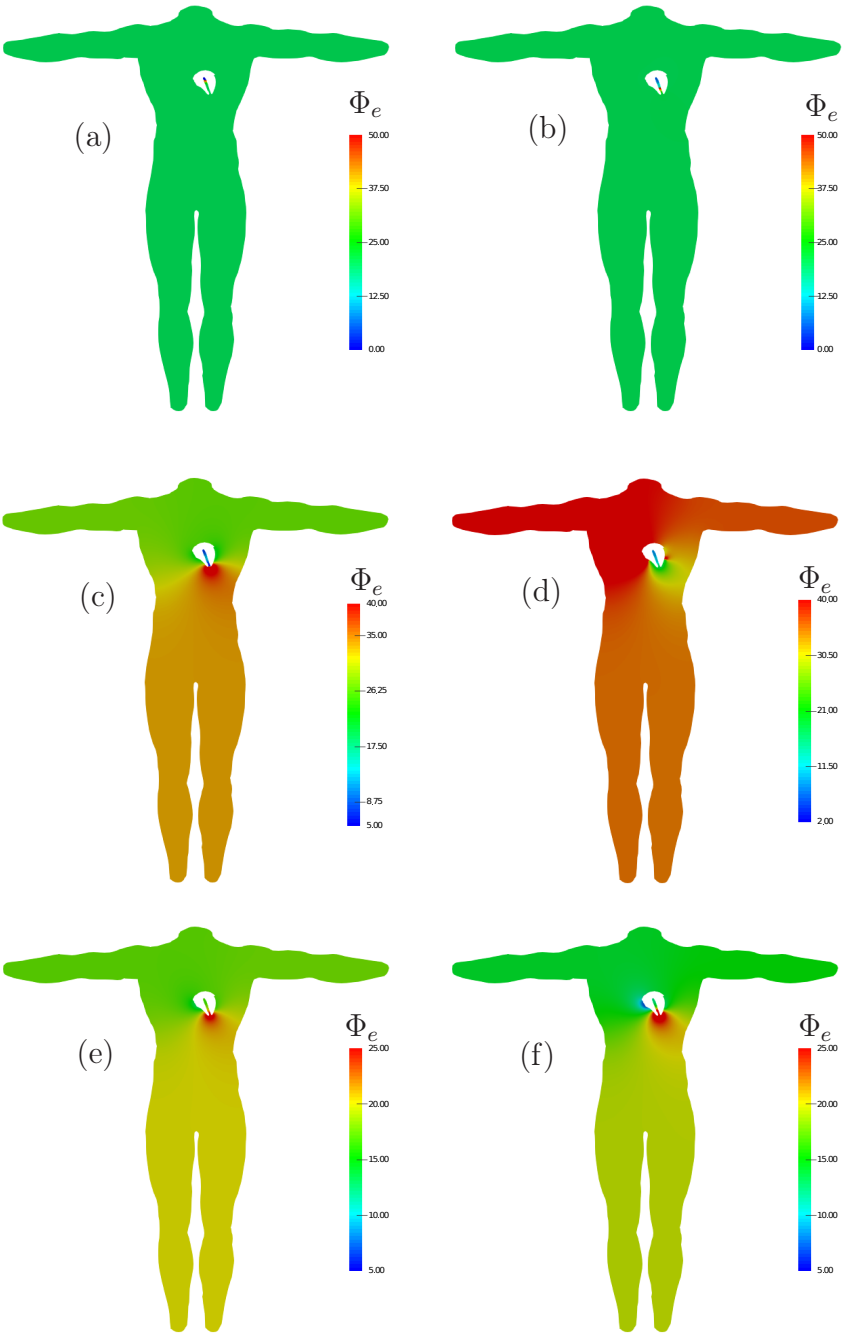

Figure 5.16: The extracellular potential contours on the body for the healthy case.

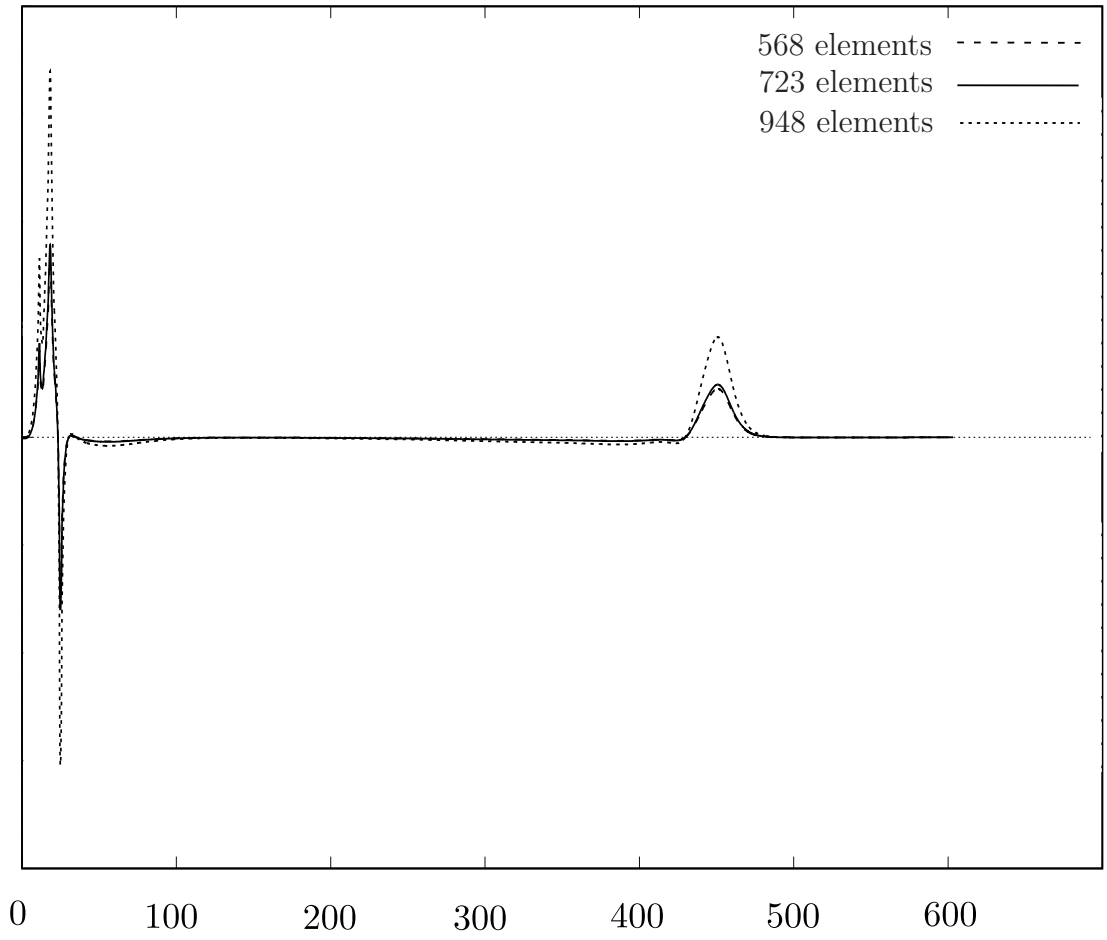

Figure 5.17: Normalized LEAD-I ECG obtained using FEM-BEM coupling with different numbers of outer line elements. Units are mV in y direction and ms in x direction.

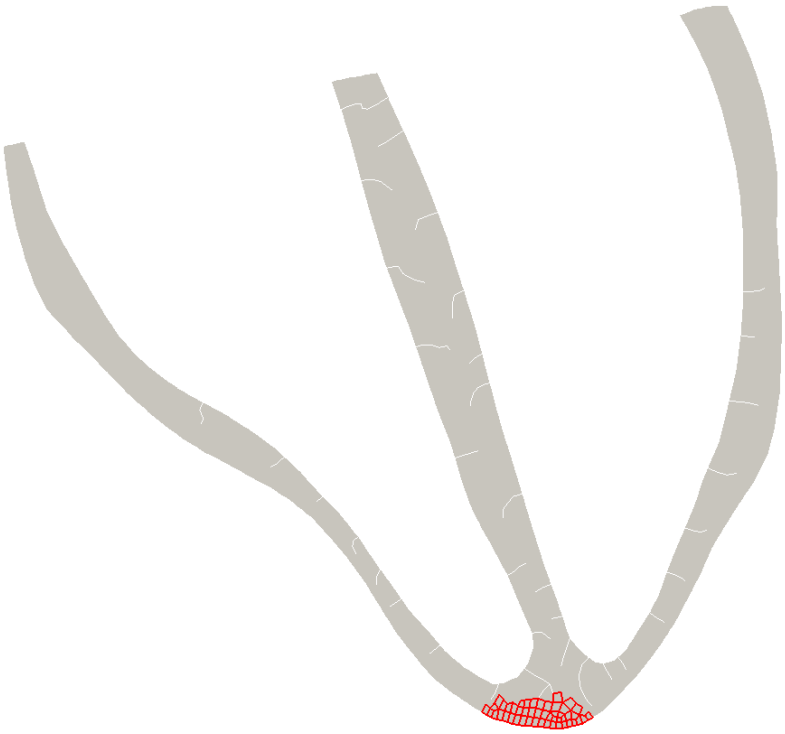

Figure 5.18: The heart section with inferial infarction.

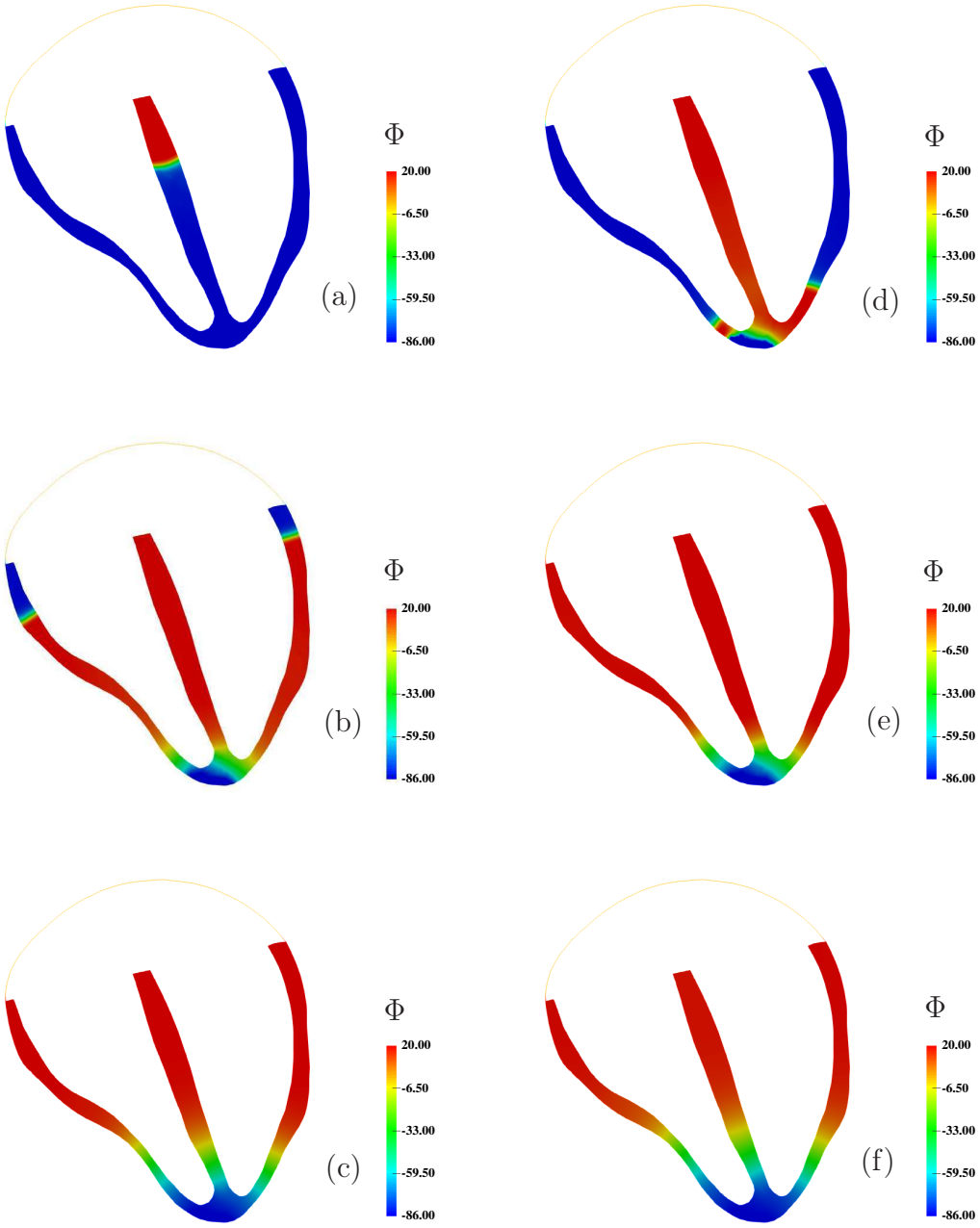

Figure 5.19: The propagation of the transmembrane potential through the infarcted heart.

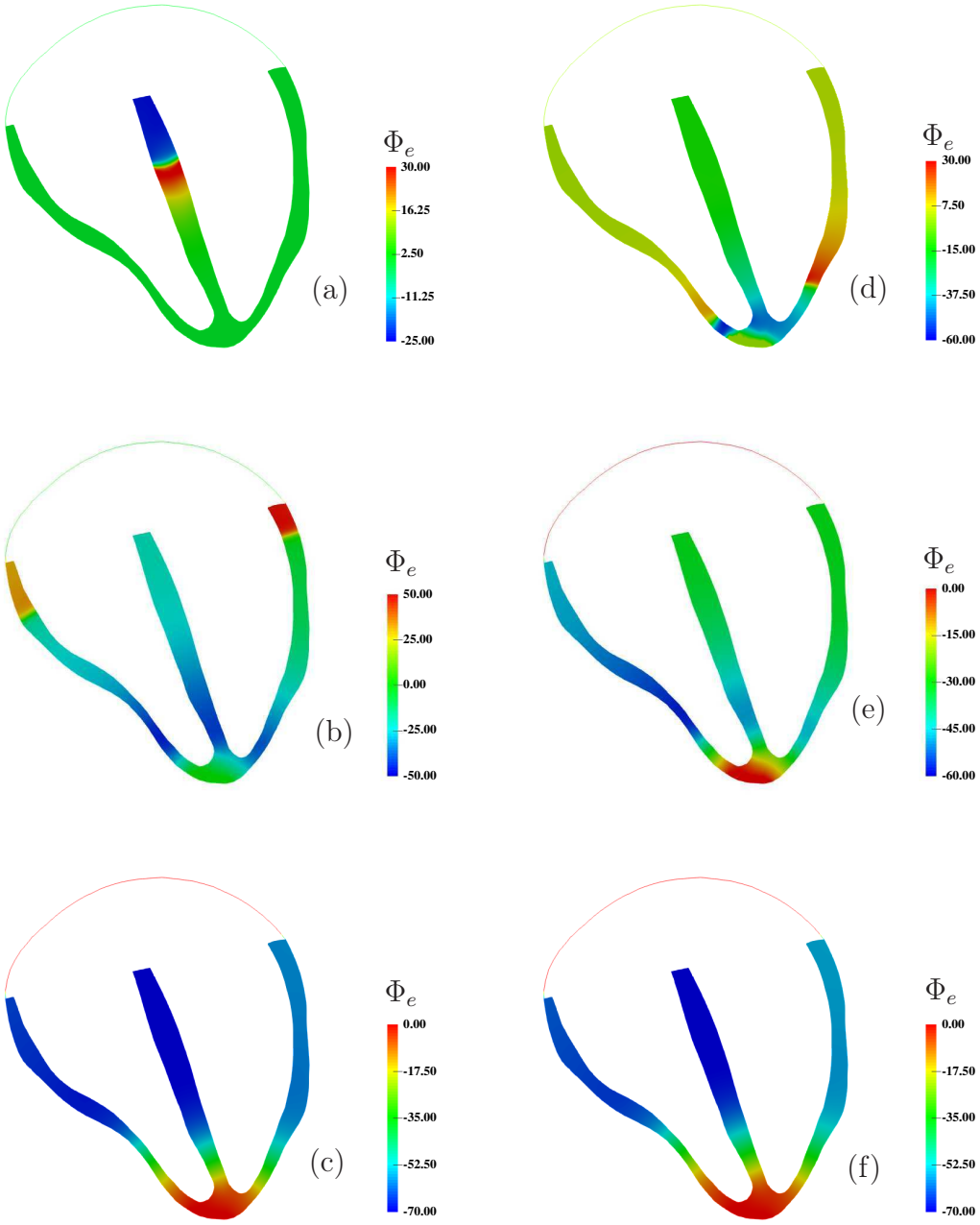

Figure 5.20: The propagation of the extracellular potential through the infarcted heart.

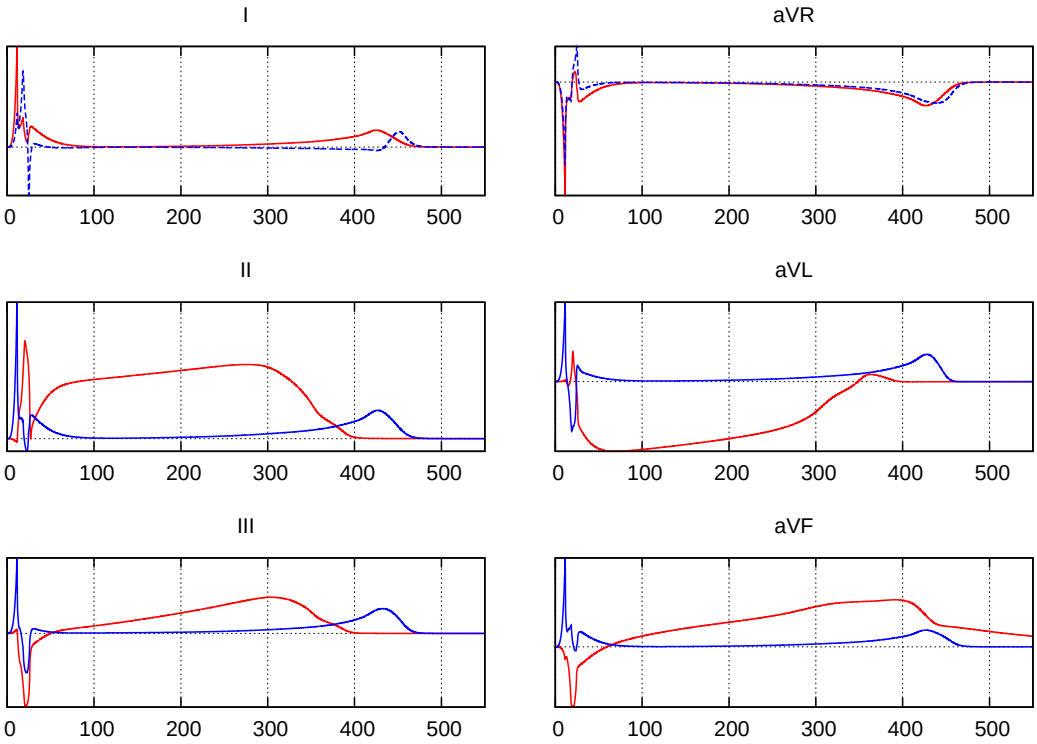

Figure 5.21: The normalized ECG of the healthy heart (blue) and the ECG of the infarcted heart (red). Units are mV in y direction and ms in x direction.

CHAPTER 6

CONCLUSION

In this thesis, we have developed numerical approaches to solve the integrated cardiac electrophysiology problem in the bidomain setting. The material model used for the electrical source term is the ionic model of electrophysiology of ten Tusscher [4]. Three numerical approaches have been proposed in this thesis, and the efficiency of the models are tested for the two dimensional ECG simulations.

In cardiac modeling, the mechanical and the electrical problems cause high computational costs. Therefore, it is important to propose new models that may accelerate the solutions. The first numeric approach we tested is the condensation of the solution matrix to eliminate the large portion of the unknowns and recover them once the reduced heart domain is solved. The second approach is solving the torso domain on the surface only. By this way, we may decrease the number of unknowns of the problem drastically.

In the first approach, the condensation of the solution matrix, has lead us to a smaller matrix to be inverted during the analysis. However, the problem involves coupling of the torso domain and the heart domain at the interface. Therefore, during the assembly of the solution matrix, the interface nodes get contribution from the torso nodes. Therefore, in order to get the exact same solution with the FEM approach, the residuals of the torso domain should be taken into account at each step. As a result, in addition to the massive storage of the stiffness terms of the torso, the computation of the residuals is required. Eventually, the solution time of the method was a little shorter than the standard finite element method. To improve the computational efficiency of this approach, one can employ the staggered solution scheme for the solution of the domains

separately. In this approach, the effect of the torso on the heart surface will be underestimated, yet, the solution time would reduce drastically because, there is no tangent contribution from the torso. Therefore, there is no need to store the shape functions or the calculated degrees of freedom. Also, using computers with a high RAM capacity will decrease the solution time of the problem, because, the storage problem will be eliminated.

The second approach, the FEM-BEM coupling, is proven to be effective. The reason is that the FEM-BEM solution matrix is assembled once and for all at the beginnig of the analysis. After that the inversion of the large torso problem is avoided. The method is very effective for the linear problems but its extention to anisotropic cases or the monolithic solution scheme are two challenging problems. The monolithic solution may let us use higher time steps and eventually reduce the solution time further.

With all three approaches, the ECG leads are captured qualitatively. The dynamic coupling of the BEM and FEM on the heart surface is shown to work effectively in terms of capturing the ECG results qualitatively and decreasing the computational cost.

In terms of cardiac modeling, this thesis does not provide any suggestions about the models defining the heart domain. However, it is clear that extension of the FEM-BEM approach to the electrophysiology and electromechanic problems would lead to new approaches. Furthermore, the ionic model and the bidomain model are flexible models and their efficiency can be exploited to develop robust and novel approaches. Futhermore, the model can be extended to three-dimensional setting. This leads to construct more realistic simulations and understand the function of the heart deeply.

REFERENCES

[1] "Longitudinal Cross Section of the Heart." https://patient.info/in/diagram/heart-cross-section-diagram. Last visited on August 2017.

[2] "The AFIB Center." http://www.theafcenter.com/p/normal-heart-rhyth.html. Last visited on August 2017.

[3] J. Malmivuo and R. Plonsey, *Bioelectromagnetism: Principles and Applications of Bioelectric and Biomagnetic Fields*. Oxford University Press, USA, 1995.

[4] K. Ten Tusscher, D. Noble, P. Noble, and A. V. Panfilov, "A Model for Human Ventricular Tissue," *American Journal of Physiology-Heart and Circulatory Physiology*, vol. 286, no. 4, pp. H1573–H1589, 2004.

[5] "The McGill Physiology Virtual Lab." http://www.medicine.mcgill.ca/physio/vlab/cardio/introECG.htm. Last visited on August 2017.

[6] "Normal ECG." https://meds.queensu.ca/central/assets/modules/ECG/normal_ecg.html. Last visited on August 2017.

[7] "European Cardiovascular Disease Statistics 2017." http://www.ehnheart.org/cvd-statistics.html. Last visited on August 2017.

[8] "Heart Disease: Scope and Impact." https://www.theheartfoundation.org/heart-disease-facts/heart-disease-statistics/. Last visited on August 2017.

[9] "Heart Disease Facts." https://www.cdc.gov/heartdisease/facts.htm. Last visited on August 2017.

[10] "Cardiovascular Risk Factors." https://www.world-heart-federation.org/resources/risk-factors/. Last visited on August 2017.

[11] "Treatment of a Heart Attack." http://www.heart.org/HEARTORG/Conditions/Conditions_UCM_001087_SubHomePage.jsp. Last visited on August 2017.

[12] "Global Action Plan for the Prevention and Control of NCDs 2013-2020." http://www.who.int/nmh/publications/ncd-action-plan/en/. Last visited on August 2017.

[13] C. Taylor and C. Figueroa, "Patient-Specific Modeling of Cardiovascular Mechanics," *Annual Review of Biomedical Engineering*, vol. 11, no. 1, pp. 109–134, 2009.

[14] J. Sainte-Marie, D. Chapelle, R. Cimrman, and M. Sorine, "Modeling and Estimation of the Cardiac Electromechanical Activity," *Computers & Structures*, vol. 84, no. 28, pp. 1743–1759, 2006.

[15] P. A. Iaizzo, *Handbook of Cardiac Anatomy, Physiology, and Devices*. Springer Science & Business Media, 2009.

[16] L. H. Opie, *Heart Physiology: From Cell to Circulation*. Lippincott Williams & Wilkins, 2004.

[17] F. H. Netter, S. Colacino, *et al.*, *Atlas of Human Anatomy*. Ciba-Geigy Corporation, 1989.

[18] S. Göktepe, A. Menzel, and E. Kuhl, "The Generalized Hill Model: A Kinematic Approach Towards Active Muscle Contraction," *Journal of the Mechanics and Physics of Solids*, vol. 72, pp. 20–39, 2014.

[19] R. FITZHUGH, "Thresholds and Plateaus in the Hodgkin-Huxley Nerve Equations," *The Journal of General Physiology*, vol. 43, pp. 867–896, May 1960. PMID: 13823315.

[20] K. H. W. J. T. Tusscher and A. V. Panfilov, "Modelling of the Ventricular Conduction System," *Progress in Biophysics and Molecular Biology*, vol. 96, pp. 152–170, Jan. 2008.

[21] J. Nagumo, S. Arimoto, and S. Yoshizawa, "An Active Pulse Transmission Line Simulating Nerve Axon," *Proceedings of the IRE*, vol. 50, no. 10, pp. 2061–2070, 1962.

[22] P. W. Macfarlane and T. D. V. Lawrie, *Comprehensive Electrocardiology: Theory and Practice in Health and Disease*, vol. 2. Pergamon, 1989.

[23] D. Durrer, R. T. Van Dam, G. Freud, M. Janse, F. Meijler, and R. Arzbaecher, "Total Excitation of the Isolated Human Heart," *Circulation*, vol. 41, no. 6, pp. 899–912, 1970.

[24] R. Klabunde, *Cardiovascular Physiology Concepts*. Lippincott Williams & Wilkins, 2011.

[25] A. L. Hodgkin and A. F. Huxley, "A Quantitative Description of Membrane Current and Its Application to Conduction and Excitation in Nerve," *The Journal of Physiology*, vol. 117, pp. 500–544, Aug. 1952. PMID: 12991237 PMCID: PMC1392413.

[26] R. Fitzhugh, *Mathematical Models of Excitation and Propagation in Nerve.* Publisher Unknown, 1966.

[27] K. Yanagihara, A. Noma, and H. Irisawa, "Reconstruction of Sino-Atrial Node Pacemaker Potential Based on the Voltage Clamp Experiments," *The Japanese Journal of Physiology*, vol. 30, no. 6, pp. 841–857, 1980. PMID: 7265560.

[28] Y. Rudy and J. R. Silva, "Computational Biology in the Study of Cardiac Ion Channels and Cell Electrophysiology," *Quarterly Reviews of Biophysics*, vol. 39, no. 01, pp. 57–116, 2006.

[29] C. H. Luo and Y. Rudy, "A Model of the Ventricular Cardiac Action Potential. Depolarization, Repolarization, and Their Interaction," *Circulation Research*, vol. 68, pp. 1501–1526, June 1991. PMID: 1709839.

[30] R. E. McAllister, D. Noble, and R. W. Tsien, "Reconstruction of the Electrical Activity of Cardiac Purkinje Fibres.," *The Journal of Physiology*, vol. 251, pp. 1–59, Sept. 1975. PMID: 1185607.

[31] R. R. Aliev and A. V. Panfilov, "A Simple Two-Variable Model of Cardiac Excitation," *Chaos, Solitons & Fractals*, vol. 7, pp. 293–301, Mar. 1996.

[32] K. H. Ten Tusscher, O. Bernus, A. V. Panfilov, *et al.*, "Comparison of Electrophysiological Models for Human Ventricular Cells and Tissues," *Progress in Biophysics and Molecular Biology*, vol. 90, no. 1, pp. 326–345, 2006.

[33] K. Ten Tusscher and A. Panfilov, "Cell Model for Efficient Simulation of Wave Propagation in Human Ventricular Tissue Under Normal and Pathological Conditions," *Physics in Medicine and Biology*, vol. 51, no. 23, p. 6141, 2006.

[34] J. Wong, S. Göktepe, and E. Kuhl, "Computational Modeling of Electrochemical Coupling: A Novel Finite Element Approach Towards Ionic Models for Cardiac Electrophysiology," *Computer Methods in Applied Mechanics and Engineering*, vol. 200, no. 45, pp. 3139–3158, 2011.

[35] R. Plonsey and R. C. Barr, *Bioelectricity: A Quantitative Approach.* Springer Science & Business Media, 2007.

[36] L. Tung, *A Bi-domain Model for Describing Ischemic Myocardial DC Potentials.* PhD thesis, Massachusetts Institute of Technology, 1978.

[37] B. J. Roth and J. P. Wikswo, "A Bidomain Model for the Extracellular Potential and Magnetic Field of Cardiac Tissue," *IEEE Transactions on Biomedical Engineering*, no. 4, pp. 467–469, 1986.

[38] J. P. Keener and J. Sneyd, *Mathematical Physiology.* New York: Springer, 1998.

[39] D. B. Geselowitz and W. Miller, "A Bidomain Model for Anisotropic Cardiac Muscle," *Annals of Biomedical Engineering*, vol. 11, no. 3-4, pp. 191–206, 1983.

[40] F. N. Wilson, F. D. Johnston, F. F. Rosenbaum, and P. S. Barker, "On Einthoven's Triangle, the Theory of Unipolar Electrocardiographic Leads, and the Interpretation of the Precordial Electrocardiogram," *American Heart Journal*, vol. 32, no. 3, pp. 277–310, 1946.

[41] R. Klabunde, *Cardiovascular Physiology Concepts*. Lippincott Williams & Wilkins, Nov. 2011.

[42] M. Kotikanyadanam, S. Göktepe, and E. Kuhl, "Computational Modeling of Electrocardiograms: A Finite Element Approach Toward Cardiac Excitation," *International Journal for Numerical Methods in Biomedical Engineering*, vol. 26, no. 5, pp. 524–533, 2010.

[43] R. M. Gulrajani, "The Forward and Inverse Problems of Electrocardiography," *IEEE Engineering in Medicine and Biology Magazine*, vol. 17, no. 5, pp. 84–101, 1998.

[44] T. B. Garcia, *12-Lead ECG: The Art of Interpretation*. Jones & Bartlett Publishers, 2013.

[45] G. R. Fleisher and S. Ludwig, *Textbook of Pediatric Emergency Medicine*. Lippincott Williams & Wilkins, 2010.

[46] M. J. Bishop and G. Plank, "Bidomain ECG Simulations Using an Augmented Monodomain Model for the Cardiac Source," *IEEE Transactions on Biomedical Engineering*, vol. 58, no. 8, pp. 2297–2307, 2011.

[47] M. Jolley, J. Stinstra, J. Tate, S. Pieper, R. MacLeod, L. Chu, P. Wang, and J. K. Triedman, "Finite Element Modeling of Subcutaneous Implantable Defibrillator Electrodes in an Adult Torso," *Heart Rhythm*, vol. 7, no. 5, pp. 692–698, 2010.

[48] P. K. Banerjee and R. Butterfield, *Boundary Element Methods in Engineering Science*, vol. 17. McGraw-Hill London, 1981.

[49] M. Potse, B. Dubé, and A. Vinet, "Cardiac Anisotropy in Boundary-Element Models for the Electrocardiogram," *Medical & Biological Engineering & Computing*, vol. 47, no. 7, pp. 719–729, 2009.

[50] G. Huiskamp, "Simulation of Depolarization in a Membrane-Equations-Based Model of the Anisotropic Ventricle," *IEEE Transactions on Biomedical Engineering*, vol. 45, no. 7, pp. 847–855, 1998.

[51] M.-C. Trudel, B. Dubé, M. Potse, R. M. Gulrajani, and L. J. Leon, "Simulation of QRST Integral Maps with a Membrane-Based Computer Heart Model Employing Parallel Processing," *IEEE Transactions on Biomedical Engineering*, vol. 51, no. 8, pp. 1319–1329, 2004.

[52] F. S. Costabal, D. E. Hurtado, and E. Kuhl, "Generating Purkinje Networks in the Human Heart," *Journal of Biomechanics*, vol. 49, no. 12, pp. 2455–2465, 2016.

[53] J. V. Tranquillo, J. Hlavacek, and C. S. Henriquez, "An Integrative Model of Mouse Cardiac Electrophysiology from Cell to Torso," *EP Europace*, vol. 7, no. s2, pp. S56–S70, 2005.

[54] S. Sovilj, R. Magjarević, A. A. Abed, N. H. Lovell, and S. Dokos, "Simplified 2D Bidomain Model of Whole Heart Electrical Activity and ECG Generation," *Measurement Science Review*, vol. 14, no. 3, pp. 136–143, 2014.

[55] S. Sovilj, R. Magjarević, N. H. Lovell, and S. Dokos, "A Simplified 3D Model of Whole Heart Electrical Activity and 12-Lead ECG Generation," *Computational and Mathematical Methods in Medicine*, vol. 2013, 2013.

[56] Z. Li, S. Zhu, and B. He, "Solving the ECG Forward Problem by Means of a Meshless Finite Element Method," *Physics in Medicine and Biology*, vol. 52, no. 13, p. N287, 2007.

[57] R. Modre, M. Seger, G. Fischer, C. Hintermuller, D. Hayn, B. Pfeifer, F. Hanser, G. Schreier, and B. Tilg, "Cardiac Anisotropy: Is It Negligible Regarding Noninvasive Activation Time Imaging?," *IEEE Transactions on Biomedical Engineering*, vol. 53, no. 4, pp. 569–580, 2006.

[58] M. Aoki, Y. Okamoto, T. Musha, and K.-I. Harumi, "Three-Dimensional Simulation of the Ventricular Depolarization and Repolarization Processes and Body Surface Potentials: Normal Heart and Bundle Branch Block," *IEEE Transactions on Biomedical Engineering*, no. 6, pp. 454–462, 1987.

[59] R. M. Gulrajani and G. E. Mailloux, "A Simulation Study of the Effects of Torso Inhomogeneities on Electrocardiographic Potentials, Using Realistic Heart and Torso Models.," *Circulation Research*, vol. 52, no. 1, pp. 45–56, 1983.

[60] X. Zhu and D. Wei, "Computer Simulation of Intracardiac Potential with Whole-Heart Model," *International Journal of Bioinformatics Research and Applications*, vol. 3, no. 1, pp. 100–122, 2006.

[61] W. T. Miller and D. B. Geselowitz, "Simulation Studies of the Electrocardiogram. I. The Normal Heart.," *Circulation Research*, vol. 43, no. 2, pp. 301–315, 1978.

[62] A. Van Oosterom and T. Oostendorp, "Ecgsim: An Interactive Tool for Studying the Genesis of QRST Waveforms," *Heart*, vol. 90, no. 2, pp. 165–168, 2004.

[63] M. Seger, G. Fischer, R. Modre, B. Messnarz, F. Hanser, and B. Tilg, "Lead Field Computation for the Electrocardiographic Inverse Problem—Finite Elements versus Boundary Elements," *Computer Methods and Programs in Biomedicine*, vol. 77, no. 3, pp. 241–252, 2005.

[64] G. Fischer, B. Tilg, R. Modre, G. Huiskamp, J. Fetzer, W. Rucker, and P. Wach, "A Bidomain Model Based BEM-FEM Coupling Formulation for Anisotropic Cardiac Tissue," *Annals of Biomedical Engineering*, vol. 28, no. 10, pp. 1229–1243, 2000.

[65] J. Xue, W. Gao, Y. Chen, and X. Han, "Identify Drug-Induced T Wave Morphology Changes by a Cell-to-Electrocardiogram Model and Validation with Clinical Trial Data," *Journal of Electrocardiology*, vol. 42, no. 6, pp. 534–542, 2009.

[66] S. Sugiura, T. Washio, A. Hatano, J. Okada, H. Watanabe, and T. Hisada, "Multi-Scale Simulations of Cardiac Electrophysiology and Mechanics Using the University of Tokyo Heart Simulator," *Progress in Biophysics and Molecular Biology*, vol. 110, no. 2, pp. 380–389, 2012.

[67] P. Colli-Franzone, L. Guerri, C. Viganotti, E. Macchi, S. Baruffi, S. Spaggiari, and B. Taccardi, "Potential Fields Generated by Oblique Dipole Layers Modeling Excitation Wavefronts in the Anisotropic Myocardium. Comparison with Potential Fields Elicited by Paced Dog Hearts in a Volume Conductor.," *Circulation Research*, vol. 51, no. 3, pp. 330–346, 1982.

[68] A. Van Oosterom, "Genesis of the T Wave as Based on an Equivalent Surface Source Model," *Journal of Electrocardiology*, vol. 34, no. 4, pp. 217–227, 2001.

[69] A. A. Becker, *The Boundary Element Method in Engineering: A Complete Course*. McGraw-Hill Companies, 1992.

[70] B. J. Roth, "Electrical Conductivity Values Used with the Bidomain Model of Cardiac Tissue," *IEEE Transactions on Biomedical Engineering*, vol. 44, no. 4, pp. 326–328, 1997.

[71] R. L. Taylor, "FEAP - Finite Element Analysis Program," 2014.

[72] M. Smith, *ABAQUS/Standard User's Manual, Version 6.9*. Simulia, 2009.

[73] J. Wong, S. Göktepe, and E. Kuhl, "Computational Modeling of Chemo-Electro-Mechanical Coupling: A Novel Implicit Monolithic Finite Element

Approach," *International Journal for Numerical Methods in Biomedical Engineering*, vol. 29, no. 10, pp. 1104–1133, 2013.